Resonance production in the π^+ π^- decay channel in proton - proton collisions at 7 TeV

Graham Richard Lee

Thesis submitted for the degree of
Doctor of Philosophy

Nuclear Physics Group,
School of Physics and Astronomy,
University of Birmingham.

June 6, 2016

ACKNOWLEDGEMENTS

I feel honoured to have had the opportunity to work with some amazing people who throughout the last four years have helped me to carry out the work I love.

First and foremost these include my supervisors Prof David Evans and Dr Orlando Villalobos Baillie without whose help, encouragement and support the completion of this thesis would not have been possible. Not only experts in their field but also the best mentors anyone starting out could hope for, they allowed me the space and patience to follow my own path whilst offering their expert knowledge along the way.

I would also like to personally thank everyone else at the UK ALICE group, these being, Dr Lee Barnby, Professor Peter Jones, Dr Roman Lietava, Dr Marian Krivda and Dr Anton Jusko as well as my good friends in the UK ALICE office located at the University of Birmingham, Physics and Astronomy Department, Didier Alexandre, Katie Graham and Nima Zardoshti. It has been an honour and privilege to work with such dedicated colleagues and I am indebted to them all.

I am grateful to have also worked with the members of the ALICE resonance group and would like to thank Dr Francesca Bellini, Dr Anders Knospe, Dr Christina Markert, Dr Viktor Riabov and my friend Inayat Rasool Bhat for all of their invaluable helpful advice and support.

The Department of Physics and Astronomy at the University of Birmingham has always provided me with the support and equipment needed to complete my thesis and I thank them also.

Finally, I would like to offer my special thanks to my parents for always being there and supporting me throughout, as well as providing me with the practical things

such as a roof over my head during the completion of this thesis.

> "Equipped with his five senses, man explores the universe around him and calls the adventure Science."
>
> — Edwin Powell Hubble (May 1929)

ABSTRACT

Short lived resonances can be used as a useful probe into the fundamental interactions that occur within the collisions of particles at high energy, as conducted in high energy experiments, such as the ones performed at the A Large Ion Collider Experiment (ALICE) experiment at the Large Hadron Collider (LHC). The environments studied range from the broad hadronic interactions created within the collisions of protons at unexplored centre-of-mass energies, to an entirely different form of hadronic matter created in the hot and dense region resulting from colliding heavy ions at high energy. However, due to the short lifetimes of resonances, they cannot be measured directly and instead must be studied using the products they decay into.

The analysis conducted focuses on the extraction of a number of resonances seen in the π^+ π^- channel; the invariant mass spectrum created contains many components which need to be accounted for within the extraction process, which also requires numerous corrections applied to it in order to accurately measure the desired peaks. This analysis made use of additional studies within a Monte Carlo (MC) simulation as well as other theoretical models to extract the $\rho(770)$, $f_0(980)$ and $f_2(1270)$ resonances from the constructed spectra and measure their properties. In doing so, this analysis highlights the practicality of using such a method as well as to encouraging further study of these resonances, primarily due to the short lifetime of the $\rho(770)$ it should make a useful probe into the underlying events within the proton - proton collisions, as well as being susceptible to medium effects within heavy ion collisions. Continued study into this analysis may also aid in parametrising the lesser known properties of the $f_0(980)$ and $f_2(1270)$ resonances and further the intrigue into whether they contain components of non-standard meson structures in their make-up.

This analysis was successful in extracting these three resonances from the π^+ π^-

spectrum in the p_t region of 0 - 5 GeV/c. The resulting spectra of these resonances are studied and the results of normalised yield (dN/dy) and mean transverse momentum $\langle p_t \rangle$ are compared to past experiments, including the first look at the $f_2(1270)$ resonance at 7 TeV in proton - proton events plus the measured results from the $\rho(770)$ and $f_0(980)$ which contribute to the parametrisation of these resonances in this unexplored energy region.

Contents

List of Tables

List of Figures

DEFINITIONS OF ACRONYMS

ACORDE A COsmic Ray DEtector

ALFA Absolute Luminosity For ATLAS

ALICE A Large Ion Collider Experiment

AOD Analysis Object Data

ATLAS A Toroidal LHC ApparatuS

BC Bunch-Crossing

BE Bose-Einstein

BSM Beyond the Standard Model

CDF Collider Detector at Fermilab

CERN The European Organization for Nuclear Research

CKM CabibboKobayashiMaskawa

CMS Compact Muon Solenoid

CTP Central Trigger Processor

DAQ Data AcQuisition system

DCA Distance of Closest Approach

DPM Dual-Parton Model

EMCal Electromagnetic Calorimeter

ESD Event Symmetry Data

EWT Electroweak Theory

GDC Global Data Collectors

HEP High Energy Physics

HLT High Level Trigger

HMPID High Momentum Particle IDentification

ISR Intersecting Storage Rings

ITS Inner Tracking System

LDC Local Data Concentrators

LEIR Low Energy Ion Ring

LEP Large Electron - Positron Collider

LHC Large Hadron Collider

LHCb Large Hadron Collider beauty

LHCf A Large Hadron Collider forward

LINAC2 Linear accelerator 2

LINAC3 Linear accelerator 3

LTU Local Trigger Unit

MC Monte Carlo

MIT Massachusetts Institute of Technology

MRPC MultiGap Resistive Chamber

MWPC MultiWire Proportional Chamber

NDF N Degrees of Freedom

PDG Particle-Data-Group

PHENIX Pioneering High Energy Nuclear Interaction eXperiment

PHOS PHOton Spectrometer

PID Particle IDentification

PMD Photon Multiplicity Detector

PS Proton Synchrotron

PSB Proton Synchrotron Booster

QCD Quantum Chromodynamics

QED Quantum Electrodynamics

QFD Quantum Flavordynamics

QGP Quark-Gluon Plasma

QGSM Quark-Gluon String Model

RF Radio Frequency System

RICH Ring Imaging CHerenkov

RHIC Relativistic Heavy Ion Collider

SDD Silicon Drift Detectors

SPD Silicon Pixel Detectors

SPS Super Proton Synchrotron

SSD Silicon Strip Detectors

STAR Solenoidal Tracker At RHIC

TOF Time Of Flight

TOTEM TOTal Elastic and diffractive cross-section Measurement

TPC Time Projection Chamber

TRD Transition Radiation Detector

TTC Trigger, Timing and Command

ZDC Zero Degree Calorimeter

CHAPTER 1

Theory

1.1 The Standard Model

The Standard Model of particle physics is currently the best representation of the physical world at the subatomic level, describing not only the variety of particles that exist (given in table 1.1), but also the interactions they undergo with each other.

The current understanding is that the fundamental particles are point like objects which can be divided into two categories, the fermions, which comprise hadronic

Table 1.1: The generations of matter

Table of the known fundamental particles of matter, including the three generations of quarks and leptons as well as the known gauge bosons [1].

	Quarks			**Bosons**
	u	**c**	**t**	γ
Mass	2.4 MeV	1.27 GeV	173.21 GeV	0
Charge (e)	2/3	2/3	2/3	0
Spin	1/2	1/2	1/2	1
	d	**s**	**b**	**g**
Mass	4.8 MeV	104 MeV	4.2 GeV	0
Charge	-1/3	-1/3	-1/3	0
Spin	1/2	1/2	1/2	1
	Leptons			**Bosons**
	e	μ	τ	Z^0
Mass	0.511 MeV	105.7 MeV	1.77 GeV	91.2 GeV
Charge	-1	-1	-1	0
Spin	1/2	1/2	1/2	1
	ν_e	ν_μ	ν_τ	$W^\pm$
Mass	< 2.2 eV	< 0.17 MeV	< 15.5 MeV	80.385 GeV
Charge	0	0	0	$\pm$ 1
Spin	1/2	1/2	1/2	1
				H
Mass				125.09 $\pm$ 0.21 GeV
Charge				0
Spin				0

matter, and the bosons acting as force carriers described by gauge theories which form the basis of the standard model.

Fermions are defined by their half integer spin values and as such must obey the Pauli exclusion principle [3]. At this fundamental level, these particles are divided into two types, known as leptons and quarks.

Leptons are split into generations, which include three generations of charged leptons (electron (e^-), muon (μ^-) and tau (τ^-)), all with the same properties apart from mass, which increases with generation. In addition, three generations of very light particles called neutrinos (electron neutrino (ν_e), muon neutrino (ν_μ) and tau

neutrino (ν_τ)) make up the rest of the lepton category; all three have zero electrical charge and are speculated to increase in mass value with generation to adhere to a mass hierarchy [4].

Quarks also come in six flavours, divided similarly into three generations. The quarks in higher generations have higher masses than the ones in lower generations. Each of the quarks is electrically charged yet have non-integer values with respect to the charge of an electron (e); positively charged quarks (up (u), charm (c) and top (t)) have a value of $+\frac{2}{3}e$ and the negatively charged quarks (down (d), strange (s) and bottom (b)) have a value of $-\frac{1}{3}e$.

All of the fermion particles have their own anti-particle associated with them; these particles have the opposite electrical charge value as their particle counterparts yet have the same mass value.

1.1.1 Gauge theories

The interactions, which occur between these particles, can be described via gauge theories [5]; in this context a gauge theory describes an interaction between two particles as the exchange of a gauge boson, which mediates a particular fundamental force. Bosons are defined as having integer spin values irrespective of whether they are fundamental or composite particles.

A well-known fundamental force, the electromagnetic force, is mediated via a well known massless and chargeless gauge boson called the photon (γ). Interactions

involving the photon are described via the gauge theory Quantum Electrodynamics (QED), in which only electrically charged particles can participate in either a repulsive or attractive interaction.

The weak force is mediated by three massive gauge bosons, the $W^{\pm}$ and Z^0, and was once best described by the gauge theory Quantum Flavordynamics (QFD) [6], but is now better understood when it is linked with QED in the Electroweak Theory (EWT). The weak interaction allows fermions to change flavour via absorption or emission of one of the gauge bosons [7]. At the fundamental level this manifests itself in allowing unstable higher generation quarks and leptons to decay downward in generation via the weak interaction. The existence of the three massive gauge bosons and one massless gauge boson within EWT is an example of spontaneous symmetry breaking [8]. In this system three of the gauge bosons in EWT acquire their mass via coupling to the Higgs field when transitioning from a high vacuum energy in the early universe to a much lower vacuum energy in the later universe.

This allows one gauge boson to remain massless (the photon) within the theory but also predicts the existence of another boson to mediate the Higgs field. Evidence for a boson within the predicted Higgs boson mass range has been observed at two of the large experiments at the Large Hadron Collider (LHC) [9] [10] and has been widely agreed to be in line with the standard model interpretation of the Higgs Boson as of March 2015 [11].

The strong interaction only has influence over quarks and induces a strong attractive force between them as described by the gauge theory Quantum Chromodynamics

(QCD). This attractive force locks quarks within very tightly bound states known as hadrons.

This force is mediated via massless gauge bosons known as gluons (g). Like EWT, QCD can be viewed as having some similarities to QED, however many key differences prevent QCD from being fully modelled. The differences between the two gauge theories begin with the definition of their assigned charges, for example QED charge is defined as the well known positive and negative electrical charge. QCD involves three charges known as colour charges associated only with quarks and gluons (*red*, *green* and *blue*) and with anti-colour charges associated with anti-quarks and gluons ($anti-red$, $anti-green$ and $anti-blue$).

This charge system is used to describe the bound structures of quarks QCD imposes via the strong attractive force experienced by non-colourless states (singlet states). Inside a quark singlet state (hadron), the quarks within the structure feel little to no attractive force between each other; such a configuration can be made with either a three quark structure (each quark having a different colour charge) known as a baryon or a quark plus anti-quark structure (with a colour and anti-colour charge of the same colour) known as a meson. Under this system anti-baryons have been observed (each anti-quark with a different anti-colour charge) and even a tetra-quark meson (two quarks and two anti-quarks) observed in 2014 [12]. Additionally, in July 2015 exotic structures were found within the $J/\psi\, p$ channel consistent with a penta-quark (four quarks and one anti-quark structure) charmonium interpretation [13].

Unlike QED, the mediator of this interaction itself carries its own colour charge (eight different possible configurations), as such gluons can self interact resulting in processes such as gluon loops becoming more energetically favourable than lower order processes. QCD is so dissimilar to QED, due to this fact, the abundance of higher order processes within a given interaction makes the calculation and modelling of a typical QCD interaction non-perturbative, i.e. calculations using perturbation methods cannot be applied to low energy or long distance interactions as the summation of all the higher order processes diverge in these interactions. Colour-charge is described in QCD by the generators of a SU(n) (Special Unitary) group; since three dimensions are needed to describe the three colour-charges, SU(3) is used with 3^2-1 generators, giving eight different flavours of gluon.

As a consequence, the QCD potential between two quarks at distance r can be roughly described with the Cornell potential [14] given in equation 1.1,

$$V(r) = kr - \frac{\alpha_s}{r}, \tag{1.1}$$

where k is an energy density scaling parameter which parametrises the non-perturbative nature of a QCD interaction and α_s is the running coupling strength of the strong interaction. As r increases in equation 1.1, the first term in the potential becomes dominant and the energy required to separate the two quarks increases linearly with separation until it is energetically more favourable to produce a quark anti-quark pair. For small r the potential is effectively a Coulomb potential as the second term

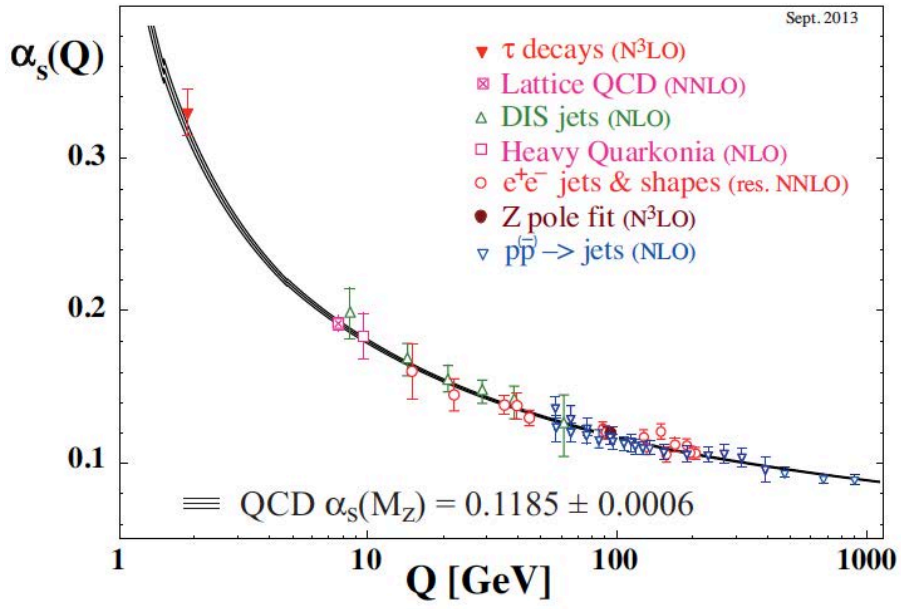

Figure 1.1: Strength of α_s as a function of energy scale. Data from various experiments are presented along with the central average and $\pm 1\sigma$ limits. Taken from [1].

dominates, however α_s is seen to have r dependence as the effective colour charge increases with distance. α_s is plotted in the momentum transfer region $1 < Q^2 < 1000$ GeV^2 in figure 1.1, where Q^2 directly corresponds to the minimum energy required to physically probe a process that occurs at a distance scale r.

The scaling of α_s is described by equation 1.2,

$$\alpha_s(Q^2) = \frac{12\pi}{\beta \ln \frac{Q^2}{\Lambda^2}}, \tag{1.2}$$

where Q^2 is the momentum transfer and β is a constant defined by the number of quark flavours within the theory ($f = 6$) and the number of colour charges ($n = 3$) combined in the following way,

$$\beta = 11n - 2f, \tag{1.3}$$

where Λ is defined as a function of a momentum transfer value for which α_s has a known value and is thus called the QCD scaling constant. Λ is quantified by equation 1.4 and has the value of approximately 200 MeV [15],

$$\ln \Lambda^2 = \ln \mu^2 - \frac{12\pi}{\beta \alpha_s(\mu^2)}, \tag{1.4}$$

where μ^2 is the momentum transfer for which $\alpha_s(\mu^2)$ is known, thus making Λ a purely measured quantity.

For low values of Q, α_s is large and non-perturbative due to the higher order processes, and perturbative for higher values of Q. This crossover happens at a value of $r \approx 1$ fm. In order to make predictions in the non-perturbative region numerical theoretical models are required such as lattice QCD [16] and the Massachusetts Institute of Technology (MIT) bag model [17].

The latter model depicts a bag representing the colourless hadron, in which, valence quarks are bound by a great pressure that exists outside of the bag. The amount of energy required to separate the quarks increases linearly with increasing r as shown in equation 1.1. This can continue until the energetically favourable outcome is to create a new quark and anti quark pair that binds to the original valence quarks, the net result of which is the formation of two colourless bags.

Lattice QCD describes space-time as a lattice structure in order to model QCD interactions. In this way a momentum cut-off value can be introduced, related to the spacing of the lattice components, thus removing the non-perturbative nature imposed by large coupling strengths.

1.2 Resonances

The study of heavy and light hadrons is useful for probing elements that comprise the standard model. Large quantities of particles created within high energy interactions originate at some stage by the production (and decay) of very short lived particles known as resonances. The study of such particles is therefore important as they are believed to be better probes of the primary mechanics influencing these interactions, as they can exist and decay within the small time frame these interactions occur over. This means they are more suited for comparing theoretical models and data studies within high energy experiments.

Resonances were amongst the first particles to be discovered during the early phase of high energy physics studies and are characterised by the method in which they are detected. Resonances refer to a class of particle which have very short lifetimes ($\sim 10^{-25}$ s), therefore, to study these particles, momentum and energy measurements from the decay products of the resonance are used to build an invariant mass distribution using the formula in equation 1.5,

$$M_{1,2}^2 = (E_1 + E_2)^2 - (\boldsymbol{p_1} + \boldsymbol{p_2})^2, \tag{1.5}$$

where $M_{1,2}$ is the invariant mass, $E_{1,2}$ is the energy and $\boldsymbol{p_{1,2}}$ is the momentum vector of the decay products 1 and 2. By this method, resonances can be viewed as a peak within the distribution centred around a central mass value with a width (typically from 10 to 200 MeV) which is related to the exponentially decaying distribution derived from the Fourier transform of the energy distribution described below.

The amplitude of an assumed s-wave resonance is defined using a s-wave potential scattering given in equation 1.6,

$$f = \frac{e^{2i\sigma} - 1}{2ik}, \tag{1.6}$$

where σ is the s-wave phase shift and k is the centre of mass energy. The phase shift is real for elastic scattering yet has a positive imaginary part for inelastic scattering. Equation 1.6 can be rearranged by defining a constant Γ which determines the rate at which the amplitude becomes maximum at some energy E_0, and is expressed by equation 1.7,

$$f = \frac{\Gamma - ik}{2k(E_0 - E)} = \frac{1}{k} \frac{\frac{\Gamma}{2}}{(E_0 - E) - \frac{i\Gamma}{2}}, \tag{1.7}$$

thus the differential cross-section is given by equation 1.8,

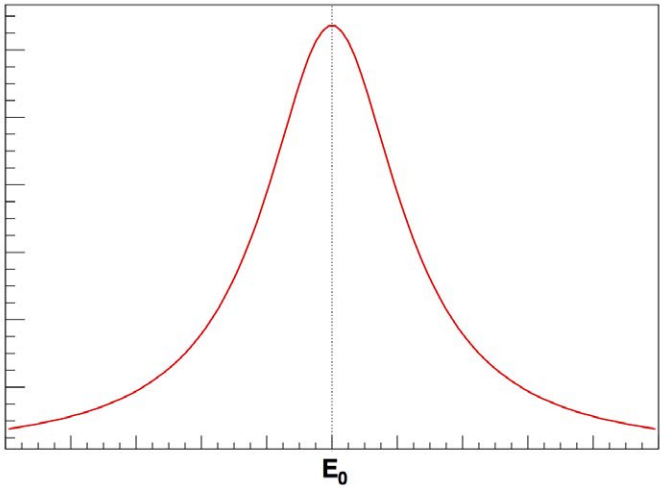

Figure 1.2: Example of Breit-Wigner function, where E_0 has the value of one and Γ has the value 0.5.

$$\frac{d\sigma}{d\Omega} = |f|^2, \tag{1.8}$$

and gives a total cross-section of,

$$\sigma = 4\pi|f|^2 = \frac{4\pi}{k^2}\frac{\frac{\Gamma^2}{4}}{(E-E_0)^2+\frac{\Gamma^2}{4}}. \tag{1.9}$$

This is the origin of the Breit-Wigner function seen in equation 3.2, used in most resonance studies to describe the distribution of the resonance peak. An example of this function is also shown in figure 1.2, in this context Γ is defined as the 'full width at half maximum' (shortened to 'width') of the resonance peak.

1.2.1 Resonance measurements and interpretations

An important resonance, called the $\rho(770)$ meson, was discovered in 1961 using the 14-inch hydrogen bubble chamber of Adair and Leipuner at the Cosmotron at Brookhaven National Laboratory [18]. The particle was of particular interest due to a prediction that it could be represented as π meson with different spin alignments of the valence quarks, existing with a spin value of $J = 1$, making it one of the better known vector mesons. The $\rho(770)$ was also seen to have a large width ($\Gamma \sim 150$ MeV), denoting a small lifetime for this resonance ($\tau \sim 1.5$ fm/c).

Within a similar mass range to the ρ it is believed that all of the lower mass scalar mesons are simply excited quark plus anti-quark configurations, however because these scalar mesons decay via two-body channels with no orbital momentum these scalar mesons may have a quark, quark, anti-quark, and anti-quark ($qq\overline{q}\overline{q}$) configuration as well as the standard quark plus anti-quark [19].

Two highly contested examples of this are the $f_0(980)$ and $a_0(980)$; by assuming a simple excited quark plus anti-quark configuration [[20] [21]] the scalar meson nonet does not follow the same mass ordering as the vector meson nonet; thus studies also sometimes view them as either a closely bound $qq\overline{q}\overline{q}$ structure (as seen in bag model calculations in which the light scalar mesons are good candidates for tightly bound $qq\overline{q}\overline{q}$ systems [[22], [23]]) or a $K\overline{K}$ molecule configuration [24], due to both the $f_0(980)$ meson and $a_0(980)$ meson lying relatively close to the $K\overline{K}$ mass threshold, at 987 MeV/c^2. This can be further supported since in some relativistic quark models a $K\overline{K}$ molecule structure can appear to resemble a weakly bound s-wave state, which

Table 1.2: Main properties of extracted resonances in the $\pi^+\pi^-$ channel

Resonance	Mass (MeV/c)	Full Width (MeV/c)
$\rho(770)$	775.49 $\pm$ 0.34	149.1 $\pm$ 0.8
$f_0(980)$	980 $\pm$ 10	40 to 100
$f_2(1270)$	1275.1 $\pm$ 1.2	$185.1^{+2.9}_{-2.4}$

in turn may be identified as the $a_0(980)$ and $f_0(980)$ particles [[25], [26]]. In more recent studies this question is still an open topic, yet it has been implied that the $a_0(980)$ and $f_0(980)$ cannot both be considered as $K\overline{K}$ molecules despite lying close to the threshold [27].

The properties of the $f_0(980)$ resonance are relatively less well known than the $\rho(770)$, as the mass value (980 MeV) has a $\pm$ 10 MeV uncertainty and the width value is only known to be within the range of 40 to 100 MeV [1]. The resonance is known to have a $J^{PC} = 0^{++}$ making it the lightest scalar meson.

The possibility for pseudo-scalar mesons to interact amongst themselves and meson-baryon interactions has given rise to the idea of interactions occurring between vector mesons [[28] [29]]. It has been postulated that the interactions between two $\rho(770)$ mesons with isospin $I = 0$ and with a spin value of $S = 2$ could lead to the two becoming bound within the resonance $f_2(1270)$ [30] as a possible explanation of the resonance's $J^{PC} = 2^{++}$. However to date the $f_2(1270)$ has been widely regarded to be a standard $q\overline{q}$ configuration.

The main properties of these three resonances are shown in table 1.2 as shown in the PDG [1], as they will be the primary focus of the main analysis.

1.2.1.1 Previous measurements

The $\rho(770)$ has a number of decay channels ranging from it's primary decay channel ($\pi^+ \pi^-$) to leptonic decays ($e^+ e^-$ and $\mu^+ \mu^-$).

The NA60 experiment at the Super Proton Synchrotron (SPS) at The European Organization for Nuclear Research (CERN) measured the ρ in In - In (Indium) collisions at an energy of 158 GeV per nucleon [31]. This study was conducted with $\sim$ 400,000 events and found a centrality dependent broadening effect of the extracted ρ peak, where centrality is defined as the amount of overlap between the two colliding particles. However, it was also seen that even with this effect there was no noticeable mass shifting due to heavy ion environmental effects.

The $\rho(770)$ has also been measured by the Solenoidal Tracker At RHIC (STAR) detector at Relativistic Heavy Ion Collider (RHIC) in both proton - proton and Au - Au (Gold - Gold) ion collisions at a centre-of-mass energy of 200 GeV. In this analysis it was observed that the mass of the $\rho(770)$ resonance was 40 MeV below the generalised Particle-Data-Group (PDG) value of 775.49 ± 0.34 MeV in minimum bias proton - proton collisions at 200 GeV, and 70 MeV below the PDG value in Au - Au (gold) collisions also at 200 GeV [[32] [33]]. These mass shifts appear to reduce in magnitude at larger transverse momentum (p_t) values; this was interpreted to be due to some of the ρ mesons decaying later in the events and as such in a much less interactive environment, thus their decay products have fewer interactions with background particles. This was conducted alongside the measurements of the $f_0(980)$ resonance; no mass or width measurements were taken in this study but the raw

yield was extracted and a normalised spectrum for the $f_0(980)$ and the $\rho(770)$ was constructed.

Another relevant measurement of these resonances was taken in the study of the production cross-sections of both the $\rho(770)$ and the $f_0(980)$ resonances within proton - proton events at 52.5 GeV conducted with the ISR at CERN [34]. This is amongst the standard references for these particles in high energy hadronic collisions as it found the production cross-section of the ρ to be in agreement with other experiments listed in the PDG.

The NA45 experiment at the CERN SPS also measured dielectron production in heavy ion (Pb-Au) collisions and observed an enhancement of the e^+ e^- pairs in the invariant mass region of the $\rho(770)$ [35]. This hinted at the possible modification to the $\rho(770)$ production properties by re-scattering within the heavy ion environment.

1.2.2 Quark-Gluon Plasma (QGP)

Along with resonances being useful to understanding fundamental interactions there is another field of study they can be interesting in, most notably within A Large Ion Collider Experiment (ALICE) [36] at CERN.

The behaviour of α_s as a function of Q^2 implies that at a high enough momentum transfer (low distance between individual quarks) α_s is reduced ($\alpha_s \approx 0.5$) and the quarks will be free from confinement. This predicts some critical energy density in which hadronic matter (quarks and gluons) undergoes a phase transition where

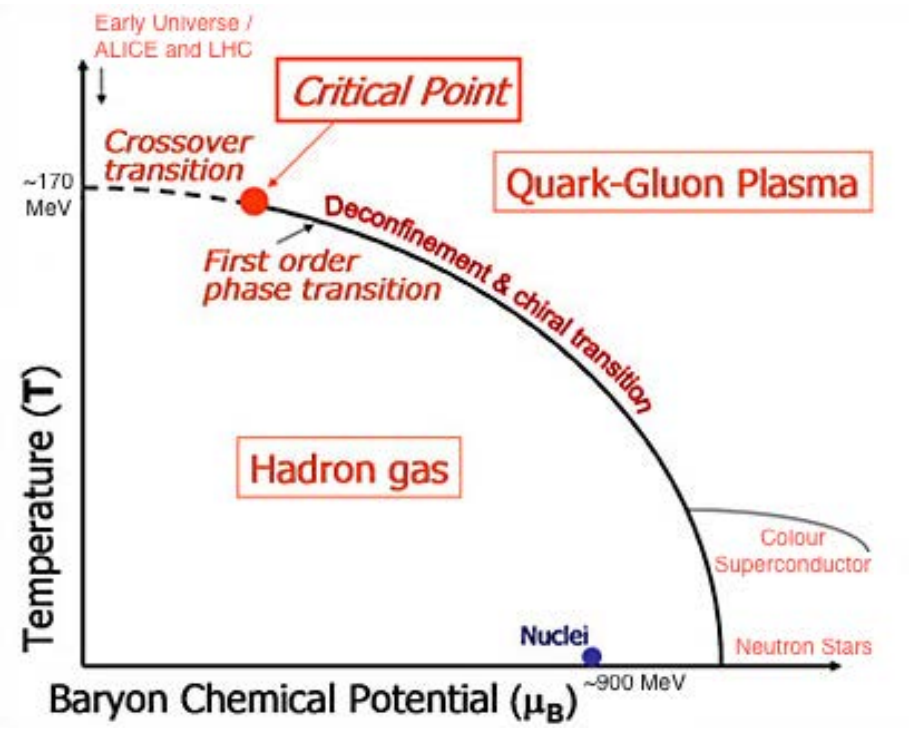

Figure 1.3: Phase diagram of hadronic matter showing phase transitions at the two extremes of both temperature and baryo chemical potential [37].

they become asymptotically free. This state of matter is known as the Quark-Gluon Plasma (QGP), the phase transition for which is depicted in the phase diagram in figure 1.3.

By existing in a high energy density, by either inducing a high temperature (denoted by T) or a high matter density (denoted by the chemical potential for baryon number called baryon chemical potential μ) or a combination of both, hadronic matter undergoes the phase transition into this QGP phase. Calculations from numerical models such as lattice QCD and the MIT bag model [17] estimate the critical temperature of the transition to be $\approx$ 175 MeV and for the critical energy density of $\sim$ 1 GeV/fm^3, assuming zero baryo chemical potential [38]. As shown in figure 1.3, conditions for the transition into the QGP phase require high temperatures or

densities as is believed to be the conditions present in the very early universe (10^{-5} seconds after the Big Bang). Other sources of such conditions may include the core of collapsing neutron stars, where the pressures can be as extreme as five to ten times that for normal quark matter [39].

Within the QGP state, quarks and gluons are described as being de-confined. This is thought to have the added effect of reducing the observed constituent quark mass to a bare mass value. This is highlighted by the observation that a very large portion of a hadron's mass ($\sim 99\%$) does not originate from the mass of the valence quarks but from the binding energy between them [40]. This constituent mass can be thought of as being the result of a spontaneous breaking in symmetry of chiral symmetry, where the chirality of a particle is defined as being equal to the helicity of the particle, in the special case of the particle having zero mass. Helicity is defined in equation 1.10,

$$h = \frac{\bar{\mathbf{s}}.\bar{\mathbf{k}}}{|\bar{\mathbf{k}}|}, \tag{1.10}$$

where $\bar{\mathbf{s}}$ is the spin vector of the particle and $\bar{\mathbf{k}}$ is the momentum vector of the particle. With this property, a particle can be defined as being either left handed or right handed. In the special case in which all particles are massless, the number of left handed and right handed particles is conserved; however due to the fact quarks have finite mass, this value is not conserved within QCD interactions and thus quark masses are observed to be higher than the quark base mass in normal

hadronic matter. Analysis of the $\rho(770)$ and other resonances is conducted to observe not only how the extracted yields and energy measurements compare in different underlying events, but also to observe any possible mass shift due to the resonances existing and then decaying when chiral symmetry is partially restored within the QGP medium. Due to the $\rho(770)$ meson's short lifetime (corresponding to a mean lifetime of $\sim 4.5 \times 10^{-24}$ s and thus a mean travel distance of $\sim 1.35 \times 10^{-15}$ m) this has been postulated to be one of the better probes to observe this effect [41]. This is because resonances like the ρ (that have a lifetime ~ 1 fm/c) are able to interact and decay within the window of time in which the environment created in the heavy ion collisions exists, as discussed in section 1.2.3. This should be compared to the ϕ meson resonance with a mean travel distance of $\sim 4.65 \times 10^{-14}$ m, which therefore decays outside the QGP volume.

1.2.3 Creating a Quark-Gluon Plasma (QGP) in Heavy Ion Collisions

As seen in figure 1.3, the conditions required for hadronic matter to transition into the QGP phase are high temperature or high density. The collisions of heavy ions at high energy give rise to the conditions in which to create QGP matter. In these conditions a region of high density and high temperature is created in between the colliding ions as they pass through each other. The resulting formation of quark and anti-quark pairs within this region at high density and high temperature will be in the QGP phase if it is above the critical energy density.

The RHIC experiments [42], and ALICE at the LHC, are the only experiments special-

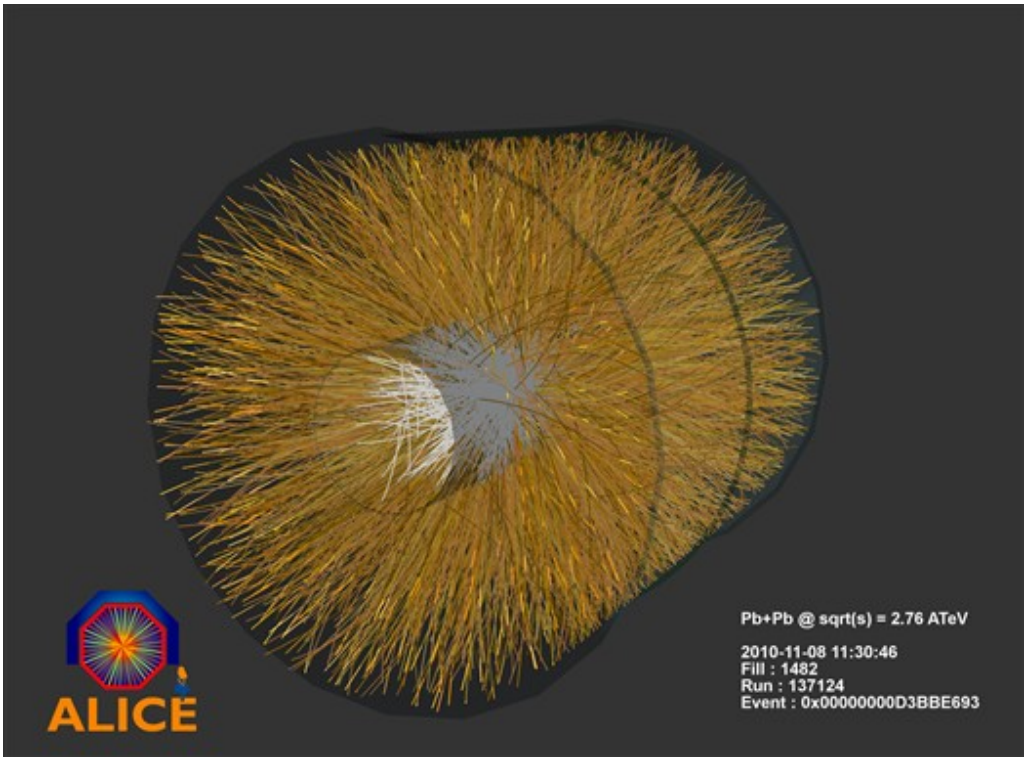

Figure 1.4: Tracking event display of ALICE displaying an example Pb - Pb (lead - lead) event from ALICE repository.

ising in heavy ion collisions operating today, with only two of the RHIC experiments (STAR and PHENIX) still running. At present all of the main experiments at the LHC also study the heavy ion collisions at the LHC, though the others are designed principally of proton proton collisions.

Figure 1.4 shows an example of an event from a lead - lead collision at ALICE, showing the high densities of final tracks detected after the hadronization of the fireball created within the collisions, where the fireball is defined as the region of pre-hadronic strongly interacting matter created in the collision overlap region.

Within ALICE, the fireball created only exists within a small window of time ($\sim$ 10 fm/c $\sim$ 10^{-23} s), after which the system expands and cools until the temperature drops below the critical temperature and the material undergoes hadronization,

shortly afterwards the material undergoes chemical freeze-out, at which point inelastic interactions cease. The material then expands further and undergoes the thermal freeze-out when all elastic interactions also cease.

1.2.4 Kinematics

For convenience, many different variables are used to describe the collisions within high energy physics experiments, some of which will be described in this section, due to them being referenced in later sections. The most commonly used of these is the transverse momentum of a particle (p_t) which is defined in equation 1.11 as the momentum value of a particle in the direction perpendicular to the beam axis, usually taken to be the z-axis. This is favoured above other momentum measurements as it is invariant under Lorentz boosts in the z-direction,

$$p_t = \sqrt{p_x^2 + p_y^2}, \tag{1.11}$$

where p_x and p_y are the momentum values of the particle in the x and y coordinates respectively.

Another commonly used variable is known as rapidity and is defined in equation 1.12,

$$y = \frac{1}{2} \ln \frac{1+\beta}{1-\beta} = \frac{1}{2} \ln \frac{E+p_z}{E-p_z}, \tag{1.12}$$

where β is the particle velocity in natural units, E is the total energy of the particle and p_z is the momentum component of the particle in the longitudinal direction. Rapidity is used to characterise the longitudinal momentum of a particle with respect to the z-axis (beam axis) and, like p_t, it is sometimes quoted as its shape is also invariant under longitudinal Lorentz boosts. Within high energy physics experiments it is very likely that the mass of the particle is much less than the momentum value of the particle and in this case rapidity can be approximated by a simpler variable known as pseudo-rapidity defined in equation 1.13,

$$\eta = -\ln \tan \frac{\theta}{2}, \tag{1.13}$$

where θ is defined as the angle between the total momentum vector direction and the beam axis (z direction), with emphasis placed on the fact that η is dependent only on θ and as such is easier to calculate in practice.

CHAPTER 2

A Large Ion Collider Experiment (ALICE)

2.1 Large Hadron Collider (LHC) at The European Organization for Nuclear Research (CERN)

2.1.1 Introduction

The Large Hadron Collider (LHC) [43] is the most powerful synchrotron particle collider ever built. The 27 km circumference accelerator began construction in 1998 at the The European Organization for Nuclear Research (CERN). The ring itself

is situated in the tunnels previously occupied by the Large Electron - Positron Collider (LEP), ranging from 50 m to 170 m beneath the Franco - Swiss border.

The LHC's primary design is for the production of proton - proton collisions at the high centre of mass energy of 14 TeV. The LHC first conducted its first proton - proton collision runs in 2010 and 2011 at half its design energy (7 TeV), along with a run at 8 TeV with increased luminosity in 2012. In June 2015 the second run of the LHC began, starting with 13 TeV proton - proton collisions.

The LHC is also designed to collide lead (Pb) ions at a maximum design energy of 5.1 TeV per nucleon, with a lower running energy of 2.76 TeV per nucleon, conducted over one month in 2010 and again over one month in 2011. Aside from this the LHC also conducted proton - lead collisions, in 2013, at an energy of 5.02 TeV per nucleon.

2.1.2 Design

Figure 2.1 depicts the basic layout of the LHC design and how it is segmented into eight regions, the focus of each is known as a collision point. The four main large experiments listed below are located at points 1,2,5 and 8.

- A Large Ion Collider Experiment (ALICE) (point 2);
- A Toroidal LHC ApparatuS (ATLAS) experiment (point 1);
- Compact Muon Solenoid (CMS) experiment (point 5);
- Large Hadron Collider beauty (LHCb) experiment (point 8).

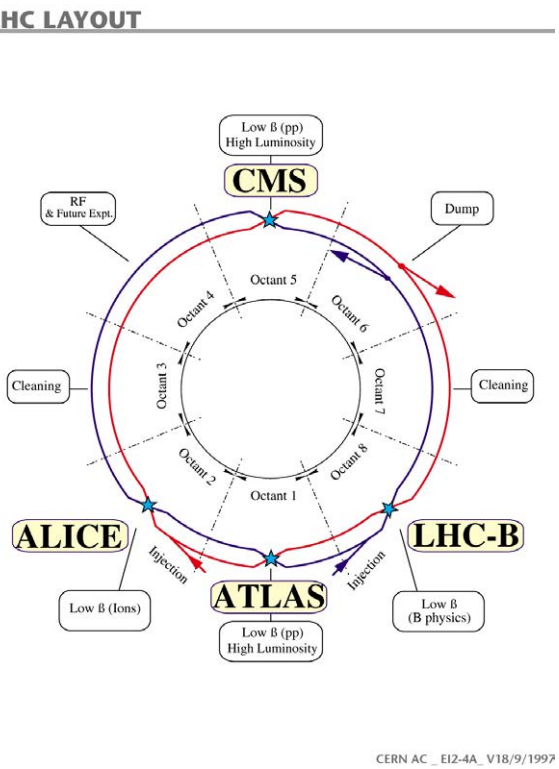

Figure 2.1: Basic layout of the LHC taken from [44].

The injection of the colliding particle beams occurs just before points 2 and 8. The beams are injected into the LHC via the Super Proton Synchrotron (SPS). Beam cleaning occurs at points 3 and 7, with stray particles, not defined within the ordered bunches, being removed. These beams can be ejected via a kicker magnet into the beam dump at point 6 [45].

The acceleration of the bunches themselves is conducted at point 4 with the use of the Radio Frequency System (RF), which consists of eight cavities within four cylindrical refrigerators (cryomodules) per beam. This produces the electromagnetic field of 5.5 MV/m which accelerates protons and lead ions to the designed energy level.

Aside from the four large experimental detectors at the LHC, other smaller experiments include the TOTal Elastic and diffractive cross-section Measurement (TOTEM)

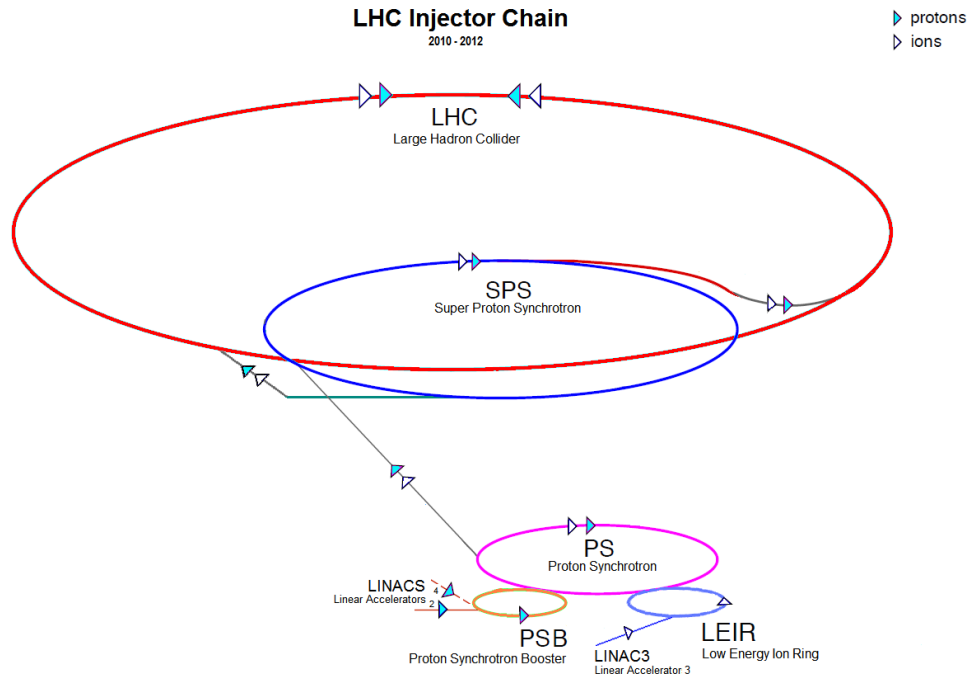

Figure 2.2: Layout of the CERN accelerator complex taken from [49].

[46] experiment which provides the latest measurements of the proton - proton cross section, A Large Hadron Collider forward (LHCf) [47] experiment used to simulate cosmic rays and Absolute Luminosity For ATLAS (ALFA) which accurately measures the luminosity of a given run period [48].

Figure 2.2 displays the LHC alongside its supporting accelerators. These include the Proton Synchrotron (PS) which stores the initial ionized hydrogen injected from the Linear accelerator 2 (LINAC2) at an energy of 120 MeV and the Proton Synchrotron Booster (PSB) at an energy of 1.4 GeV. From there the protons are injected into the Super Proton Synchrotron (SPS) at an energy of 26 GeV where they are accelerated further to an energy of 450 GeV. At this point they are then injected into the LHC itself, which is designed to accelerate them to the final collision energy of 7 TeV via the Radio Frequency System (RF) and controlled via the constant magnetic field of

0.535 T at the start of the acceleration to 8.33 T at a nominal beam energy 7 TeV. Protons are injected into the LHC rings to form bunches (containing approximately 1.15×10^{11} protons each). These bunches are approximately 7.5 cm in length and 7.5 m apart from each other meaning there can be a possible maximum of 3564 bunches stored within the LHC rings at one time, however normally only 2808 of these possible slots are used in a given run period.

For heavy ion runs, lead atoms are ionized and injected from the Linear accelerator 3 (LINAC3) and accelerated with the same method as protons through the PS and Super Proton Synchrotron (SPS) set-up after requiring an additional starting acceleration from the Low Energy Ion Ring (LEIR).

At the interaction points of the main experiments, focusing magnets are used to focus the beams into the smallest possible cross-sectional area ($\sim 16\ \mu$ m $\times\ 16\ \mu$ m) and therefore the largest interaction cross-section for proton - proton events. This cross section (σ_{event}) can be written in terms of the collider luminosity for the given event type and the number of events per second as seen in the formula in equation 2.1,

$$N_{event} = \mathcal{L}\sigma_{event}, \tag{2.1}$$

where N_{event} is the number of achieved collisions per second and $\mathcal{L}$ is the designed LHC luminosity for proton - proton collisions. The luminosity is defined as the factor in equation 2.1 that is solely due to the experimental set-up. A numerical estimation

of the luminosity can be seen in equation 2.2,

$$\mathcal{L} = \frac{fN^2}{4\pi\sigma^2}, \tag{2.2}$$

where the number of protons within a given bunch (N) is scaled by the frequency of crossing bunches (f) and $4\pi\sigma^2$, also known as the effective cross-section, where σ^2 is the cross-sectional area of the beams ($16 \times 10^{-4}\text{cm}^2$). This gives the total design luminosity for the LHC a value of ($10^{34}\text{cm}^{-2}\text{s}^{-1}$). With an inelastic collision cross-section of 60 mbarns at 7 TeV, the LHC is capable of 600 million inelastic events per second.

2.2 A Large Ion Collider Experiment (ALICE)

2.2.1 Introduction

A basic schematic layout of the ALICE detector is shown in figure 2.3.

Typical for a main LHC experiment, ALICE incorporates a cylindrical layered design comprised of many sub-detectors. Each sub-detector has a number of functions, which when used in conjunction with many of the others, allow a reconstruction of the collisions they surround. Such studies include the de-confinement of quarks in the high temperature and density environment created in the heavy ion collisions [51], as described in section 1.2.2 and the possible chiral symmetry restoration as a

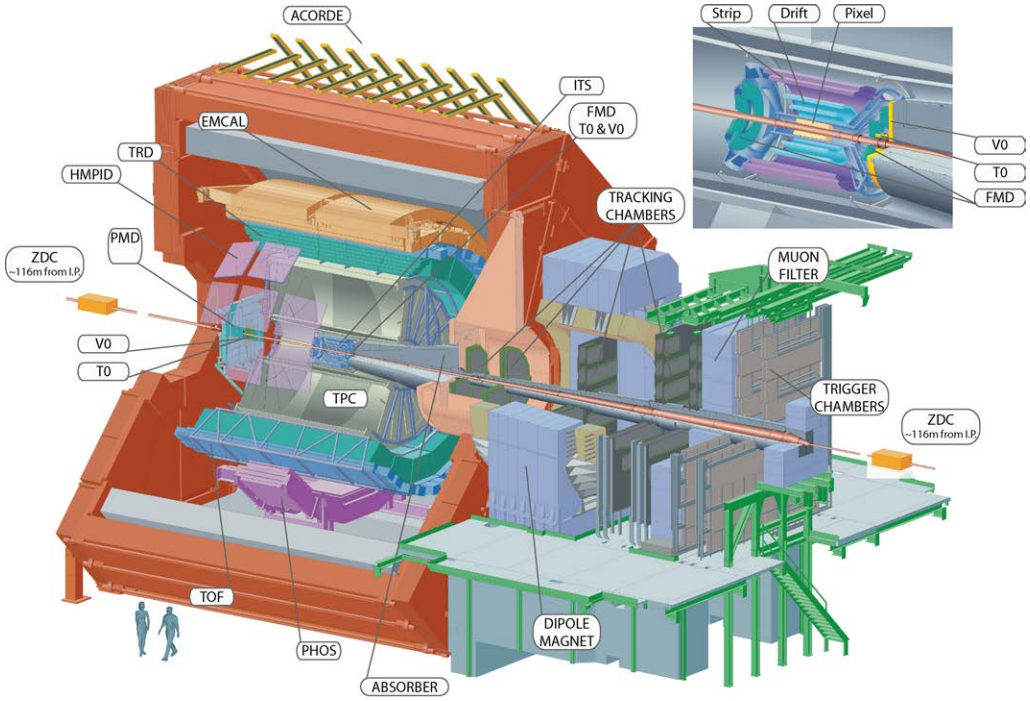

Figure 2.3: ALICE 3D schematic layout with labels to the main detectors and apparatus from [50].

result [52].

The main function of ALICE is to measure the collisions produced from lead ions in the LHC in order to further understand the very hot and very dense material created therein. This design however increases the read-out time for some of the detectors and this restricts the maximum usable luminosity for proton - proton collisions to 10^{30} cm^{-2}s^{-1}. The lead - lead collision luminosity for ALICE however, matches the design luminosity of the LHC itself at 10^{27} cm^{-2}s^{-1}.

Due to this design goal, ALICE is designed to reconstruct accurately very high multiplicity events (2,000 to 8,000 charged particles per unit of rapidity). The 10,000 ton structure itself is 26 m long and 16 m $\times$ 16 m in height and width. The central detectors lie within the 0.5 T solenoidal magnetic field, in this region the sub-detectors

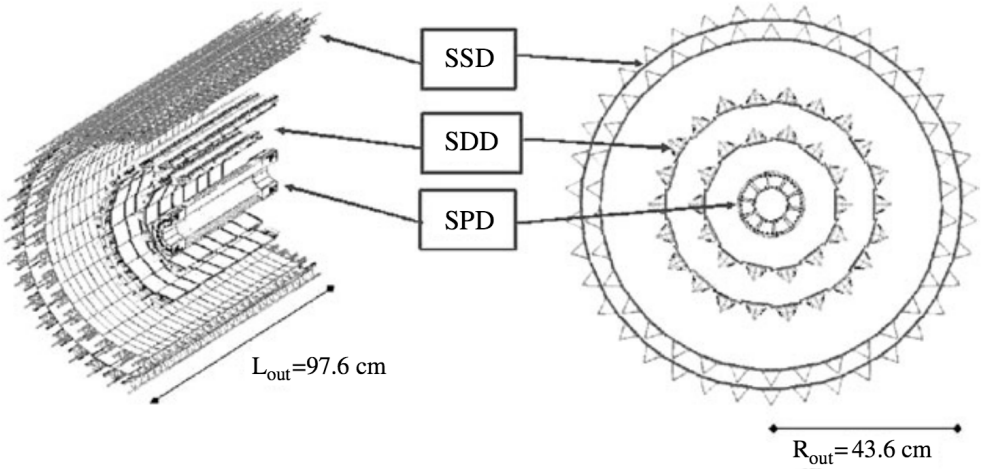

Figure 2.4: ITS schematic layout taken from [54].

have an acceptance over a pseudo-rapidity range of $|\eta| < 0.9$ [53].

2.2.2 Inner Tracking System (ITS)

The Inner Tracking System (ITS) is the closest sub-detector to the interaction point, ranging from a distance of 4 cm to 43.6 cm away. Figure 2.4 shows the schematic layout of the ITS.

It is comprised of six individual layers of silicon detectors which are split into three distinct types. Closest to the interaction point (with the highest particle density) the ITS is comprised of two layers of pixel detectors [53] (4 cm to 7 cm away from the interaction point), followed by two layers of drift detectors [53] (15 cm to 24 cm away from the interaction point), with the last two layers of the ITS (38 cm to 43 cm away from the beam line) comprised of double-sided Silicon Strip Detectors (SSD) [53].

The Silicon Pixel Detectors (SPD) consist of 1,200 pixel chips with 256 × 32 cells, each with dimensions 50 μm × 425 μm. The individual chips are arranged in linear structures called a ladder configuration, where detector sensors are mounted on linear structures to provide overlapping regions of the sensitive areas in both the $r\phi$ and z directions to ensure full angular coverage for vertex reconstruction.

The pixel detectors were chosen for their excellent geometric precision ($\sigma_{r\varphi}$ = 12 μm and σ_z = 100 μm) and two track resolution ($\sigma_{r\varphi}$ = 100 μm and σ_z = 850 μm), due to the high track density close to the interaction point. The first four layers of the ITS have been designed to be two dimensionally segmented, thus allowing an unambiguous two dimensional read-out which leads to an excellent signal to noise ratio for the high velocity particles close to the interaction point.

Tracklets are defined and reconstructed only from tracks that produce hits in both layers of the SPD; this coupled with the binary nature of the read-out gives the best combination of a quick and simple read-out time (one bit per pixel).

The Silicon Drift Detectors (SDD), like many gaseous drift detectors, uses the transport time of electrons from an ionized material, with this detector using the ionization of 300 μm thick Neutron Transmutation Silicon to achieve this. The typical drift time of the SDD is 5.4 μs. Like the SPD, the SDD is arranged into ladders of material, with fourteen ladders each with six detectors in layer 3 of the ITS and twenty two ladders with eight detectors in layer 4 of the ITS.

These drift detectors were chosen to measure multiple tracks with high resolution

in this region of ALICE where the charged track density is approximately 7 tracks cm^{-2}. By working in conjunction with the detectors on layer 5 and 6 of the ITS the SDD is also able to produce the ITS measurement of Particle IDentification (PID) via the energy loss of the track through the medium of the detector.

In the SSD region the particle densities are approximately 0.5 tracks cm^{-2}. Again these detectors are arranged into ladders with 748 modules in layer 5 (22 per ladder) and 950 modules in layer 6 (25 per ladder). Each module has a sensor connected to two hybrids, each with six front end chips. By switching the N and P sides between the two layers the detection of fake tracks can be minimized.

The SSD is required to match the tracks detected within the ITS with the tracks detected within the Time Projection Chamber (TPC) discussed in section 2.2.3. Matching of these tracks is critical to the reconstruction of the whole event with low momentum tracks measured purely in the ITS (200 MeV/$c < p <$ 1 GeV/c) and high momentum tracks ($p >$ 1 GeV/c) requiring information from both detectors to accurately track the particles.

The SSD also provides the last half of the ITS PID capabilities using the energy loss $\mathrm{d}E/\mathrm{d}x$ of the track through the detector (see section 2.2.4 for more information).

2.2.3 Time Projection Chamber (TPC)

The TPC, shown in figure 2.5, is the major tracking detector within ALICE and performs the main measurements for charged PID (with a resolution better than 6.5%

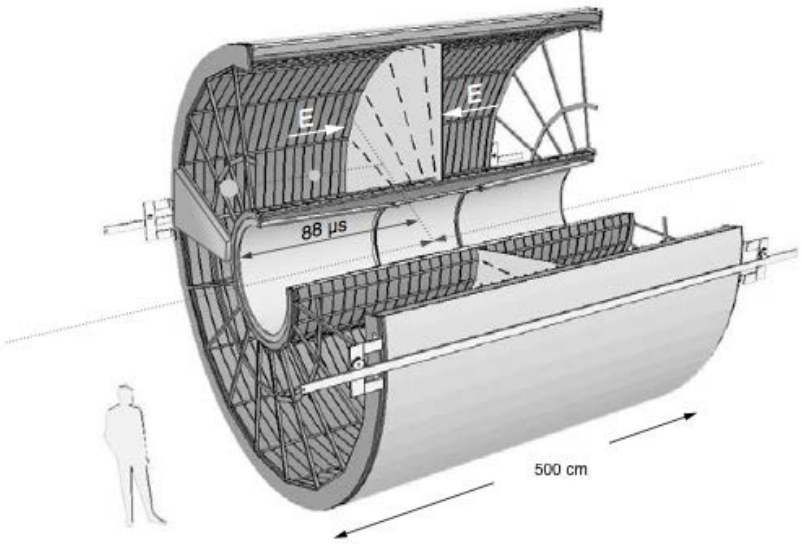

Figure 2.5: TPC 3D schematic layout taken from [53].

on the measured value of $\frac{-\mathrm{d}E}{\mathrm{d}x}$ defined in equation 2.4) and momentum measurement (with a resolution better than 6.5% for 10 GeV/c tracks and better than 1% for 1 GeV/c tracks). The TPC provides good determination of the primary vertex position along with the ITS for all events with a large multiplicity (10^4 tracks) due to its good two-track separation in the region $p_t < 10$ GeV/c and $|\eta| < 0.9$.

The detector itself has inner and outer radii of 85 cm and 250 cm respectively and is 500 cm long in the beam direction; the large volume gives this main tracking detector a good path coverage. The structure is split into two drift regions separated by a high voltage (100 kV) electrode in the centre. Like all drift chamber detectors, tracking and measuring charged particles is accomplished via the ionization of a gas mixture within the chamber. In the ALICE TPC the gas is a mixture of Ne, $C0_2$ and N_2 in the mixing ratio 90 : 10 : 5 within the 95 m^3 volume.

The drift regions are comprised of mylar strips wound around 18 inner and outer

support rods. The end plates are equipped with wire planes in 18 sectors, multi-wire proportional chambers and cathode pads with a active area of 32.5 m^2 and 570,000 electronic channels in three different sizes.

For the electrons to drift, a uniform electric field along the direction of the beam axis, created by an electrode, is required. This allows for the z-coordinate of a track to be calculated with the x-y position being determined by the pad position. The slow drift time (100 μs) over the full 2.5 m length is the main limiting factor for the ALICE proton - proton luminosity, with 40 proton - proton events per drift time, however with the low multiplicity of these events they are distinguishable.

The track momentum measurements are determined by the curvature of the track within the 0.5 T magnetic field as given by equation 2.3,

$$p_t = (0.3)RQB, \tag{2.3}$$

where the transverse momentum (GeV/c) is proportional to the radius of curvature R (m) and the magnetic field strength is given by B (T). The direction of the curving track identifies it as having either a positive or negative charge Q and plays just one part in the PID function of the TPC.

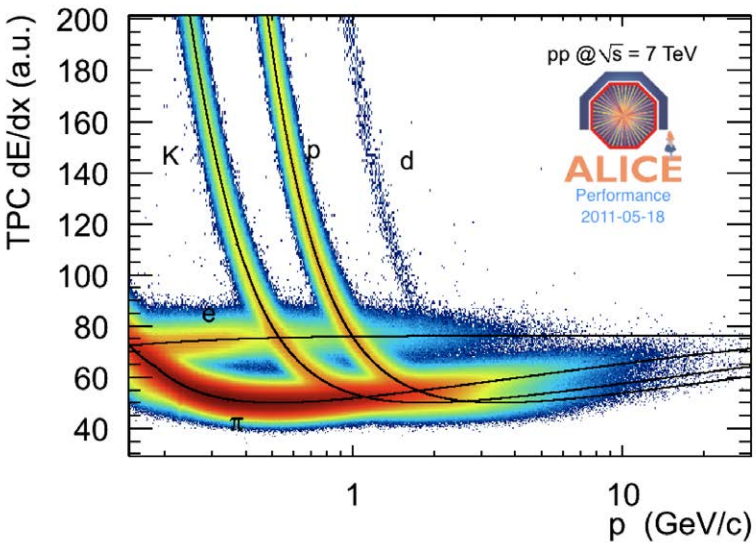

Figure 2.6: TPC energy loss ($\mathrm{d}E/\mathrm{d}x$) measurement vs. measured momentum separation, thus identifying Kaons (K), Protons (p), Deuterons (d), Electrons (e) and Pions (π). Taken from [50]. Solid lines highlight the expected $\mathrm{d}E/\mathrm{d}x$ calculation for the given stable particle.

2.2.4 Particle IDentification (PID) method applied in the TPC

The TPC is also one of the main charged particle PID detectors. Like the ITS it uses the measurement of the energy loss of particles passing through a material. When charged hadrons are traveling at relativistic speeds ionisation becomes the main component of this energy loss through electromagnetic interactions. This energy loss per unit length can be quantified via the Bethe - Bloch formula [55] given in equation 2.4,

$$\frac{-\mathrm{d}E}{\mathrm{d}x} \propto \frac{Z^2}{\beta^2} ln\gamma, \tag{2.4}$$

where z is the atomic number of the medium, β is the relativistic velocity (v/c), and γ is the Lorentz factor defined as $1/\sqrt{1-\beta^2}$. The energy loss as described by

the Bethe - Bloch formula in equation 2.4 decreases as $1/\beta$ for $\beta < 0.95$ but then increases as $\ln\gamma$ for $\beta > 0.95$.

The magnitude of the signal from the read-out pads corresponds to the energy loss of the measured particle within the TPC gas mixture. By plotting both the momentum measurement, determined from equation 2.3, versus this energy loss measurement, charged hadrons of different masses can be separated into clear bands as seen in figure 2.6.

From this, tracks that fall within a standard deviation around these bands can be identified by using the expected σ value calculated using the expected $\mathrm{d}E/\mathrm{d}x$ for the desired particle type and the measured $\mathrm{d}E/\mathrm{d}x$ as seen in equation 2.5,

$$n_\sigma = \frac{\frac{\mathrm{d}E}{\mathrm{d}x}_{Measured} - \frac{\mathrm{d}E}{\mathrm{d}x}_{Expected}}{\sigma_{Expected}}, \tag{2.5}$$

where n_σ is the multiples of σ the measured $\mathrm{d}E/\mathrm{d}x$ value is away from the expected, usually a default value for n_σ will be one to three for resonance analysis.

2.2.5 Time Of Flight (TOF)

The Time Of Flight (TOF) detector is mainly used for the identification of stable hadrons up to an energy of 2.5 GeV, which cannot be separated within the TPC (with its upper limit of 0.5 GeV for K/π separation). The detector itself is made of a number of MultiGap Resistive Chamber (MRPC) and uses the average time taken

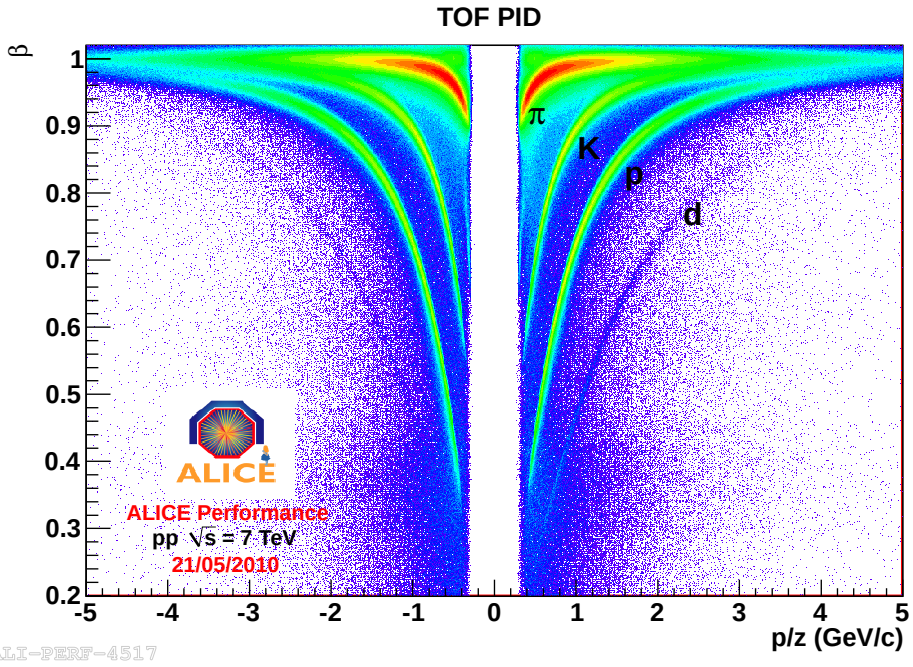

Figure 2.7: TOF β measurement vs. rigidity p/z, where p is the measured momentum and z is the particle charge. Thus identifying Kaons (K), Protons (p), Deuterons (d) and Pions (π). Taken from [50].

for a particle to traverse the detector for its PID.

Figure 2.7 shows the PID method for the TOF. Using the measurement of β (fraction of c), coupled with the momentum measurements from the tracking detectors, the identity of a given particle can be determined.

The detector has an inner radius of 3.7 m and is comprised of 1,638 MultiGap Resistive Chamber (MRPC) modules covering an area of 160 m^2 with 157,248 read-out channels (pads). Each MRPC is made of ten stacks of resistive glass plates (used mainly to prevent the ionization to avalanche into different sections) which are separated with 100 μm Nylon wires, each with a high voltage of 12.5 kV.

The gaps are filled with an ionizing gas (76.9% argon, 20% isobutane, 2.5% ethylene

and 0.6% divinyl) and a high electric field to allow amplification of the signal. The gap size is very small (100 μm) to ensure a near instant read-out time, thus giving an excellent time measurement resolution of 50 ps (where a resolution of only 150 ps was required for an adequate K/π separation).

2.2.6 Other detectors

The Transition Radiation Detector (TRD) [53] is used to identify high momentum electrons for the tracks not within the TPC PID range ($p_t > 1$ GeV/c). It ranges from 2.9 m to 3.7 m from the centre of ALICE and is divided into eighteen regions. There are a total of 540 modules, each with a 4.8 m thick radiator with MultiWire Proportional Chamber (MWPC).

The TRD uses transition radiation, which is emitted as the electrons pass through the boundary of two materials of different refractive indices. This radiation is largely dependent on γ (Lorentz factor). An electron with its low mass has a much larger γ than the other heavier particles in the same momentum range.

This transition radiation causes ionization within the MWPC where, like a typical drift chamber, the drift electrons are ionized from the 85% xenon and 15% CO_2 gas mixture to create the signal. This transition radiation signal is then seen as a large pulse at the end of a train of ionization produced by $\mathrm{d}E/\mathrm{d}x$, similar to that produced by the TPC.

The $V0$ detectors are paired arrays of scintillator counters ($V0A$ and $V0C$) covering

a pseudo-rapidity range of $2.8 < \eta < 5.1$ and $-3.7 < \eta < -1.7$. There are a total of 32 counters divided amongst four rings, which in turn are divided into 8 sectors. Each counter contains scintillation material connected to photomultipliers via optical fibers. Both $V0$ detectors lie close to the beam line (inner radius ~ 4 cm) and are an asymmetric distance away from the interaction point with $V0A$ and $V0C$ lying 340 cm and 90 cm away respectively. The $V0$s are triggering detectors for the minimum bias event trigger and basic centrality trigger for Pb - Pb events using multiplicity measurements. Using the timing information obtained from comparing the detection time to the Bunch-Crossing (BC) clock gas-beam interactions can be identified with the resolution of the timing information less than 1 ns.

The $T0$ detectors are two arrays of Cherenkov counters with twelve counters per array, used for the earliest triggers, precise timing information (better than $V0$ at 50 ps) and vertex measurements used to reject gas-beam interactions. $T0A$ is ~ 375 cm away from the interaction point in the range $4.61 < \eta < 4.92$ and $T0C$ is ~ 72.7 cm away from the interaction point in the range $-3.28 < \eta < -2.97$. The $T0$ is used together with the $V0$ to determine the centrality of a given event.

The Zero Degree Calorimeter (ZDC) is used to measure the number of spectator particles in order to estimate the number of participating nucleons within the Pb - Pb collisions. The energy of the spectator particles measured by these detectors is inversely proportional to the centrality (and number of participating nucleons) of a given collision. This set-up is made of two hadronic calorimeters, ZN (neutron ZDC) and ZP (proton ZDC), both located 116 m from the interaction point. This

set-up also includes an electromagnetic calorimeter which measures the energy of particles at forward rapidity and is located 7 m away from the interaction point.

The PHOton Spectrometer (PHOS) is an array of lead tungstate scintillators used for jet quenching studies by measuring pion and photon jet correlations at high momentum and thermal dynamic phase studies at low momentum.

The High Momentum Particle IDentification (HMPID) uses Ring Imaging CHerenkov (RICH) detectors to create and focus Cherenkov radiation resulting from fast moving particles to be detected by photon counters. This allows identification of high momentum (> 1 GeV/c) hadronic particles outside the TOF range. It has a π/K separation up to 3 GeV/c and a K/p separation of up to 5 GeV/c.

The forward muon spectrometer consists of a number of parts for tracking and triggering on rare muon events above a high momentum value of 4 GeV/c (for example from heavy flavour decays) or from low momentum value of 0.5 GeV/c. A passive absorber is located inside the L3 magnet and absorbs hadrons and photons originating from the interaction point. Muons are tracked using a high - granularity tracking system using 10 detection planes and a large 0.7 T dipole magnet located outside the L3 magnet 7 m from the interaction point. This achieves a spatial resolution of 100 μm in a region where the multiplicity density is 5×10^{-2} cm^{-2}.

The A COsmic Ray DEtector (ACORDE) is an array of plastic scintillators used to trigger on cosmic ray events.

The Electromagnetic Calorimeter (EMCal) is a high acceptance Pb scintillator sam-

pling calorimeter of length 700 cm covering a range of $|\eta| < 0.7$. This detector provides triggering on high energy jets and improves on the jet energy resolution.

The Photon Multiplicity Detector (PMD) is used to measure photon multiplicity and distribution of photons from an event using an array of gas-filled proportional chambers. It has an acceptance range of $2.3 < \eta < 3.7$.

2.2.7 Triggering

The ALICE trigger makes the critical decisions on whether a given event should be read-out by the detectors. The trigger is managed by the Central Trigger Processor (CTP) which receives signals from each triggering detector (for example the $V0$ detectors). After the decision is made, a trigger signal is passed back to the Local Trigger Unit (LTU) of the detectors. The CTP handles three levels of triggering signals, due to different detectors having different latency requirements. If one or more of the triggering detectors observe any measurable event, the first trigger signal is sent. This first trigger is a very quick signal (reaching detectors ~ 1.2 μs after the interaction) and is required by the central detectors in the high multiplicity lead - lead events. If there are no vetoes, such as a BUSY flag, the CTP sends the Level 0 ($L0$) signal to command the detectors to read-out.

The Level 1 ($L1$) reaches detectors 6.5 μs after the interaction and collects and sends all remaining trigger inputs, in this time period the event is processed further if the $L0$ signal was unopposed (compared to being opposed due to detectors sending a

BUSY flag and not ready to read-out new information). The final level, Level 2 ($L2a$ (accepted) or $L2r$ (rejected)) is set to be sent much later (programmable and set to be $\sim$100 μs after the interaction) allowing the CTP to distinguish multiple central collisions within a high multiplicity event and avoid pile - up due to slow detector drift time (such as the TPC). After the final trigger the collected event information is read-out to the Data AcQuisition system (DAQ).

There are a total of 60 trigger inputs (24 inputs in $L0$, 24 inputs in $L1$ and 12 inputs in $L2$) with a wide collection of detectors. Each has different variations on read-out and measurement time.

The CTP can receive BUSY signals from detectors that are unable to take data and thus allow the CTP to stop collection of data until the detectors stop sending the signal. From here minimum bias events can be taken again or allow read-out with a partial cluster of detectors.

The DAQ system controls the flow of data during event taking. It has an active data storage of $\sim$ 5 GBytes/s. After receiving a positive trigger from the CTP the event data is sent from the DAQ system to the Local Data Concentrators (LDC), this event is then archived at CERN where it is ready for reconstruction.

2.2.8 Local Trigger Unit (LTU) technical work

The LTU boards are installed as part of each sub-detector and act as an interface between the CTP and the sub-detector read-out electronics within the ALICE cavern.

The boards offer conversion of signal levels and on-line monitoring capabilities during global running mode. In stand alone mode, the LTU boards are able to simulate signals from the CTP for testing or for times when the CTP is absent.

The LTU is a 6U VME board which is connected directly to the CTP as well as to two other boards (the TTCvi and the TTCex) as part of the Trigger, Timing and Command (TTC) system. The TTCex connects the LTU to a given sub-detector's read-out electronics while the TTCvi is used as an optional debugging and monitoring device. Figure 2.8 shows the layout and components of the TTC system and the connection of inputs between the CTP and the LTU board.

The technical work carried out was of the testing and validation of new boards manufactured at the Rutherford Appleton Laboratory to replace the current boards due to radiation damage during the previous experimental runs.

This included helping to write the testing process code in an efficient way and executing the process systematically on all 52 of the newly manufactured boards so that all functions and outlets of the boards were rigorously tested.

Inputs from the CTP were simulated through the input ports of the LTU boards and the full range of output signals were tested for validation of both the physical port of the board and the test firmware installed on the board.

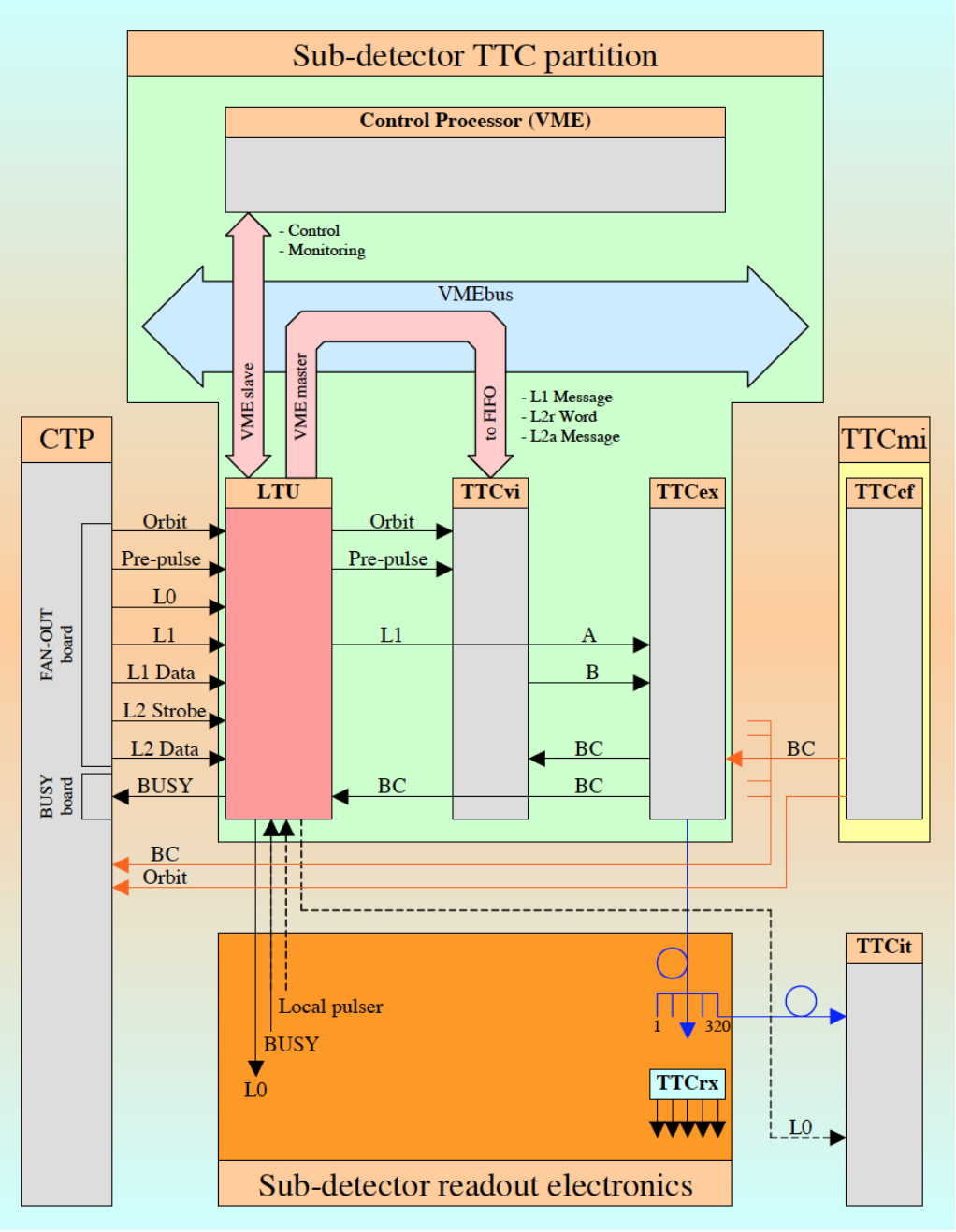

Figure 2.8: Diagram of TTC layout taken from [56], depicting the connections between the LTU and CTP within the TTC system.

CHAPTER 3

Extraction of resonances from the π^+ π^- spectrum in p-p collisions at 7 TeV

3.1 Construction of the π^+ π^- spectrum in proton - proton collsions at 7 TeV

3.1.1 Introduction

The main focus of this analysis was the extraction of the $\rho(770)$, $f_0(980)$ and $f_2(1270)$ resonances using their two - particle decay channel (π^+ π^-). By constructing an

inclusive π^+ π^- invariant mass spectrum these resonances were extracted in the momentum range of $p_t \leq 5$ GeV/c.

The main properties of these resonances are shown in table 1.2 as shown in the PDG [1].

Both the Monte Carlo (MC) study and real data analysis were conducted using the 'Aliroot' [57] package. Aliroot is based on the ROOT analysis package [58], allowing users to create up to 3-dimensional histograms using their own user-constructed code written in the C++ language. Particle tracks detected within one run period are recorded into particle track classes allowing information such as momentum, energy, track position coordinates and PID information to be sorted and accessed within a given analysis custom framework.

3.1.2 Data acquisition and selection

The data used for this study were taken from the proton - proton 2010 run period of collisions from the ALICE collaboration. This data set refers to the information collected in proton - proton runs at an energy of $\sqrt{s} = 7$ TeV. Tracks extracted within a given event for this analysis were required to meet a number of criteria to ensure the purity and condition of the tracks. The most notable of these are listed below.

- The p_t of individual particle tracks detected was required to be greater than 0.15 GeV/c, thus removing low energy particles that decay within the inner

stages of the detector. This means that no tracks were included that had a radius of curvature less then 1 metre.

- The measured $|\eta|$ of the individual particle tracks was required to be less than 0.8 as this was well within the typical ALICE $|\eta|$ acceptance range of 0.9.

- The Distance of Closest Approach (DCA) of the track to the primary vertex in the z direction was required to be less than 0.2 cm, thus allowing the background from tracks, clearly not coming from the primary vertex, to be removed, as well as to reduce influences imposed by re-scattered products originating from other vertices.

- The Distance of Closest Approach (DCA) of the track to the primary vertex in the R direction was cut according to the formula in equation 3.1 [59],

$$DCA_R < \frac{0.0455}{p_t^{1.1}}, \tag{3.1}$$

where the R direction is defined as the transverse direction ($\sqrt{x^2 + y^2}$).

Equation 3.1 is used for this cut since the DCA resolution in the transverse plane is dependent on the p_t of the measured track. This is mainly due to the influences of the magnetic field within the experimental set-up.

The cut applied to the data is comprised of the product of the DCA_R value in equation 3.1 and the track momentum p (GeV/c). This product has units of centimetres.

The formula in equation 3.1 corresponds to a seven σ cut on the DCA_R value,

where σ is the resolution on the DCA_R value. As seen in equation 3.1 the applied cut on the DCA_R value is set to be smaller than the DCA distribution of primary tracks produced in an anchored MC sample.

- The rapidity ($|y|$) of the combined pair of particle tracks for the creation of the invariant mass spectrum was required to be $|y| < 0.5$, thus giving a symmetric central rapidity value for the calculated yields of the extracted resonances.

- The minimum number of track clusters measured with the TPC was required to be 70 so as to remove events with poor TPC reconstruction. The χ^2 / NDF value, where NDF is defined as the number of degrees of freedom, for the track momentum fitting was also required to be no more than 6 for this same reason.

Individual particle tracks were identified as π tracks using their energy loss ($\mathrm{d}E/\mathrm{d}x$) in the Time Projection Chamber (TPC), as described in section 2.2.4. A $n_\sigma = 3$ cut on the expected charged pion $\mathrm{d}E/\mathrm{d}x$ value was used as the default PID cut for this analysis. However, as seen in section 3.4, this was subject to some contamination from non-pion tracks.

3.1.3 Combinatorial background removal

Two methods were used to remove the combinatorial background from the full π^+ π^- invariant mass spectrum (usually referred to as the unlike spectrum in this context). Removal of this background was important in order to eliminate the contribution from non-commutative π tracks, i.e to remove π tracks that are not correlated to

each other within the spectrum.

The first is known as the like-sign method; this method uses both the π^+ π^+ and π^- π^- invariant mass spectra and combines them using the expression $2\sqrt{n_{++}n_{--}}$ where n_{++} and n_{--} are the number of π^+ π^+ and π^- π^- pairs respectively.

An alternative method utilised mixed pairs of charged π tracks originating from different events. In this analysis the operation for the mixing method was to mix tracks from one event with tracks from five other similar events, chosen to have a close primary vertex (less than 5 cm from the mean collision point) and a similar event multiplicity value (a difference of no more than ten between the events). The resulting mixed π^+ π^- spectrum was normalised to have the same total integral as the like-sign spectrum, contrary to the more commonly used method, where the mixed spectrum was normalised to the total integral of the unlike spectrum in the region outside of the resonance peak. This normalising method was chosen in order to extract all three desired peaks together as well as to account for the large number of different components (shown in figure 3.11) that also exist within the spectrum that would also have to be accounted for when normalising this estimation.

The like-sign method was chosen as the default method to describe accurately this background. This was due to the large number of different components, such as other resonances and reflections, some of which have large widths with respect to the studied spectrum segment. The mixing tracks method would not incorporate the fine detail of this large number of components occupying the same mass range.

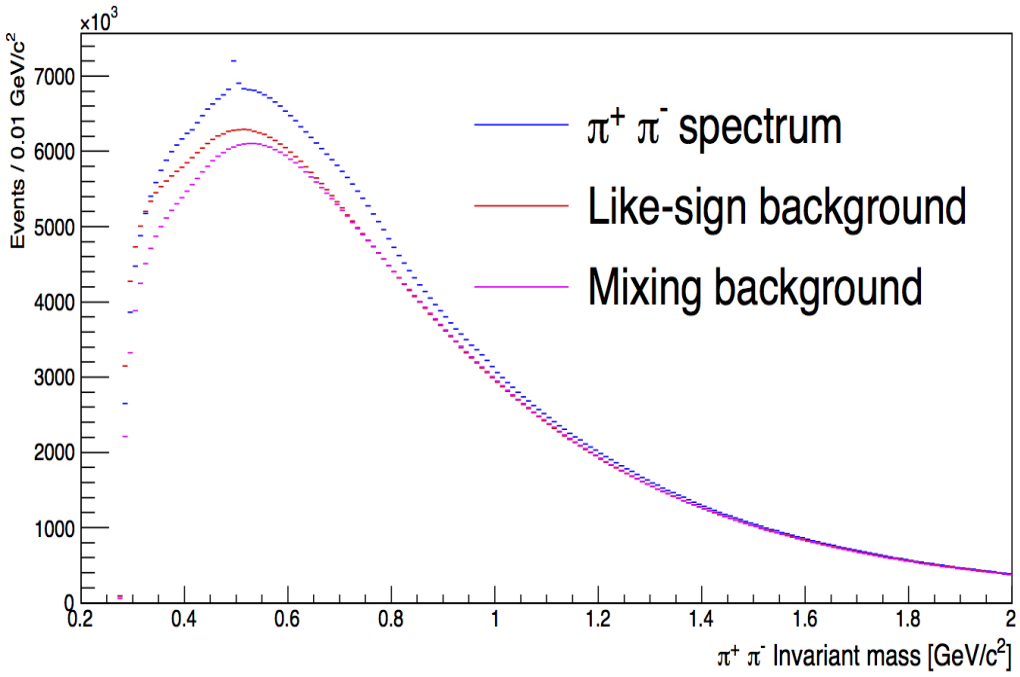

Figure 3.1: Two methods of estimating the combinatorial background (like-sign and mixing) of the π^+ π^- spectrum. The spectrum was constructed from all π tracks that met the data selection before it was split into different p_t regions. The estimated backgrounds are normalised as described in section 3.1.3.

Figure 3.1 shows the estimated combinatorial background as calculated by each of the above methods compared to the total π^+ π^- spectrum. From this it is also shown that the mixing method of estimation of the background results in a lower estimate than the like-sign method, thus resulting in a much lower signal to background ratio.

The like-sign method of estimating the true combinatorial background is the optimum choice in this case. This is due to the infeasibility of normalising the estimation calculated from the mixing method to the spectrum size outside of the ρ peak region. However, as seen in figure 3.1 the magnitude of the like-sign estimated combinatorial background is greater than the original π^+ π^- spectrum in the low mass region (< 0.3 GeV/c^2), resulting in the spectrum being truncated in this region.

3.2 Monte Carlo (MC) simulation study of the π^+ π^- spectrum

3.2.1 Introduction

Simulations of proton - proton collisions are created using Monte Carlo (MC) generators. This analysis was simulated using 40 million events with a Pythia 6.421 (flat ATLAS tune) MC generator, [[60] [61], [62], [63]].

The Pythia generator is one of the standard tools to simulate high energy collisions by using a coherent set of physical models which describe the interactions within the system from hard many-body processes (internal, interfaced or via Les Houches events) to a multi-hadron final state [64]. To do this the Pythia generator can contain within it models for Beyond the Standard Model (BSM), hadronic showers, string fragmentation, remnants within the initial beam, multiple partonic interactions and resonance decays. Pythia uses a perturbative inspired QCD model in which multi-parton interactions are described by perturbative QCD. Another specific generation tune used alongside the flat ATLAS tune in this analysis was the Perugia 0 variant, which is tuned to the results obtained from Collider Detector at Fermilab (CDF) data [65]. This focuses mostly on colour re-connections, which model string formations between final partons during fragmentation [66].

This tool was used firstly to identify the different components of the invariant mass distribution, then to calculate the efficiency of detecting the relevant resonances within the ALICE experimental set-up and lastly to create templates for the components of the spectrum which could not be described with continuous functions.

The transport package used was the GEANT4 toolkit [67] which was set to simulate particles travelling through a medium and the associated energy loss and interactions that can occur along the way. GEANT4 is used to simulate the generated particles and transport them through the ALICE experimental set-up in order to include energy loss effects, decays or detector acceptance effects by simulating interactions with the materials involved when handling real data. From here on in, reconstructed MC will be defined as MC samples that have been measured with a simulation of the ALICE experimental set-up with the same acceptance cuts as the real data sample. This can therefore give an estimation of the efficiency of the ALICE experimental set-up for this analysis.

3.2.2 Efficiency and other corrections

The efficiency for measuring each of the extracted resonances was determined by using the simulated data from 40 million Pythia events, set to have the same properties as the real (acquired run) data in the same period. The same track selections and cuts in section 3.1.2 were applied to these events to produce the reconstructed MC data.

The efficiency for measuring a given resonance within the π^+ π^- spectrum was defined as $\epsilon = \frac{Rec}{Gen}$. In this expression the denominator is the number of particles of the given resonance generated within the simulation and the numerator is the number of particles of the same resonances in the same rapidity ($|y|$) region of $<$ 0.5 in which both π^+ π^- decay products are successfully reconstructed and pass all

of the track cuts in section 3.1.2. The efficiencies for the desired resonances, as a function of p_t, are shown in figure 3.2.

Tests were also conducted to compute the efficiencies using a different MC generator; in the case of the ρ the default Pythia 6.421 efficiencies are compared to the efficiencies computed using Phojet. Phojet differs from Pythia as it focuses on a perturbative QCD model for hard parton interactions and the Dual-Parton Model (DPM) as well as the Quark-Gluon String Model (QGSM) for soft interactions [[68], [69], [70]].

The desired particles are identified within the MC sample by selecting pairs of π tracks that originate from the same mother. Each particle generated by the MC is labelled and contains information relating to the identity and energy of the particle as well as the decay chain of this particle.

This is done by observing the ancestry code within the MC generator, which with the context of a high energy collision set-up, will use the pre-set centre of mass energy of the collision to generate the particle showers resulting from the collision. This has a close analogy to modelling the evolution of unstable nuclei (nuclear decays), in which models must check if a given particle is able to decay and if so, produce the complete decay chain.

Pion tracks can be described as decaying from the same mother if the pion pair share the same mother label. This same process can also be applied to MC samples that include simulations for the f_0 and f_2 particles.

This process can be visualised by the top plot in figure 3.3, which shows the p_t

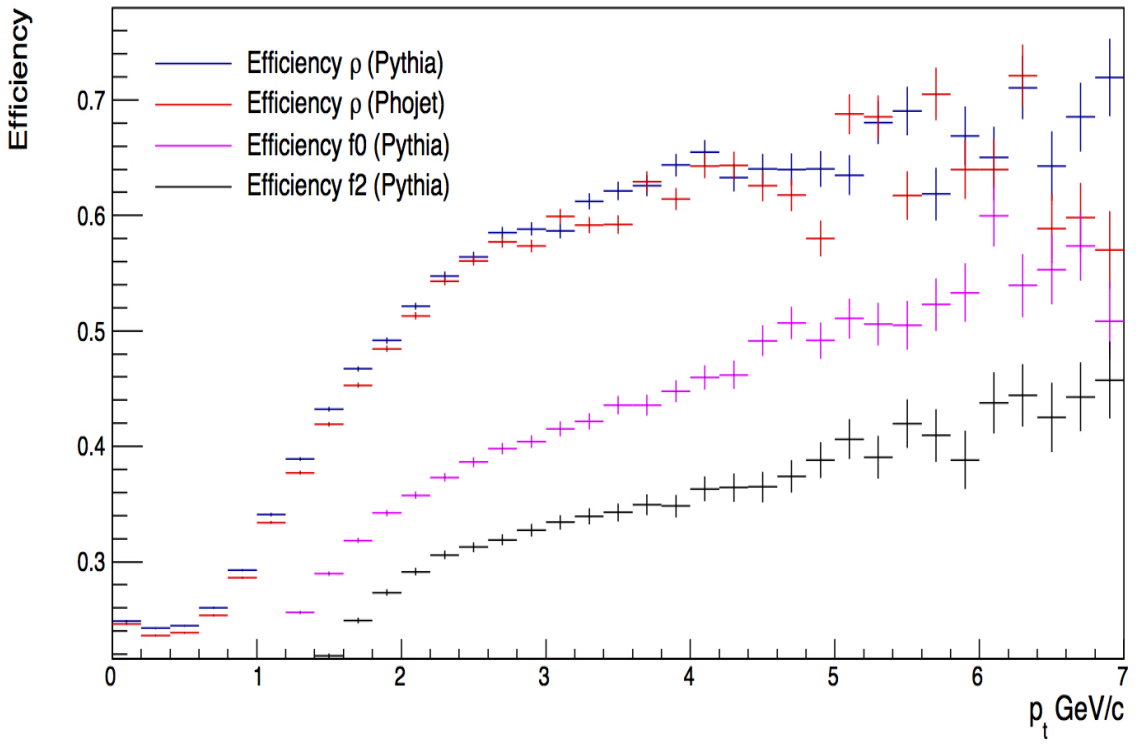

Figure 3.2: Efficiency of the ρ, f_0 and f_2 resonances as a function of p_t. The efficiencies calculated from Pythia and Phojet are compared for the ρ.

integrated generated peak of the ρ as compared to the same peak after being reconstructed. The efficiency is therefore defined as the reconstructed spectrum divided by the generated spectrum as shown in the bottom plot in figure 3.3.

However, this shows that there is a clear invariant mass dependence to the efficiency covering a wide range of detector acceptance. This implies that a distortion in the peak is introduced by the reconstruction of the peak within the π^+ π^- spectrum and, as such, the efficiency corrections for the ρ, f_0 and f_2 should be applied bin by bin to the extracted peak, as opposed to a single efficiency correction factor when extracting the integral of the peaks.

This feature is also seen when computing the efficiency for different p_t regions. As

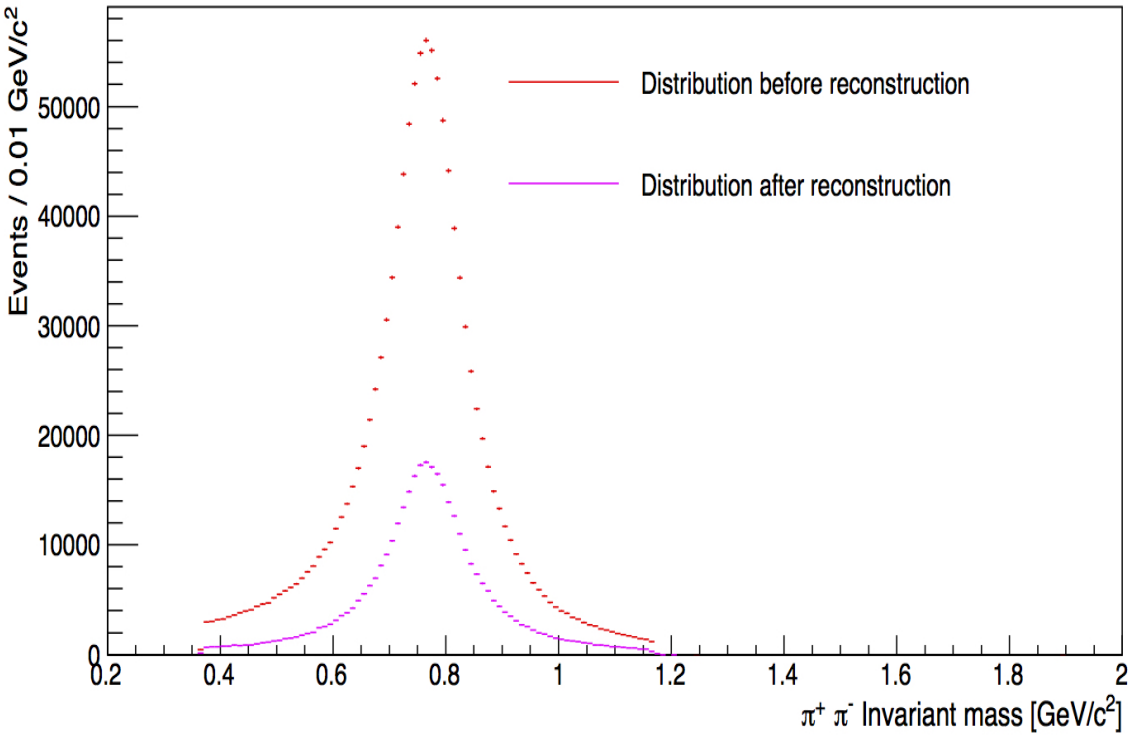

(a)

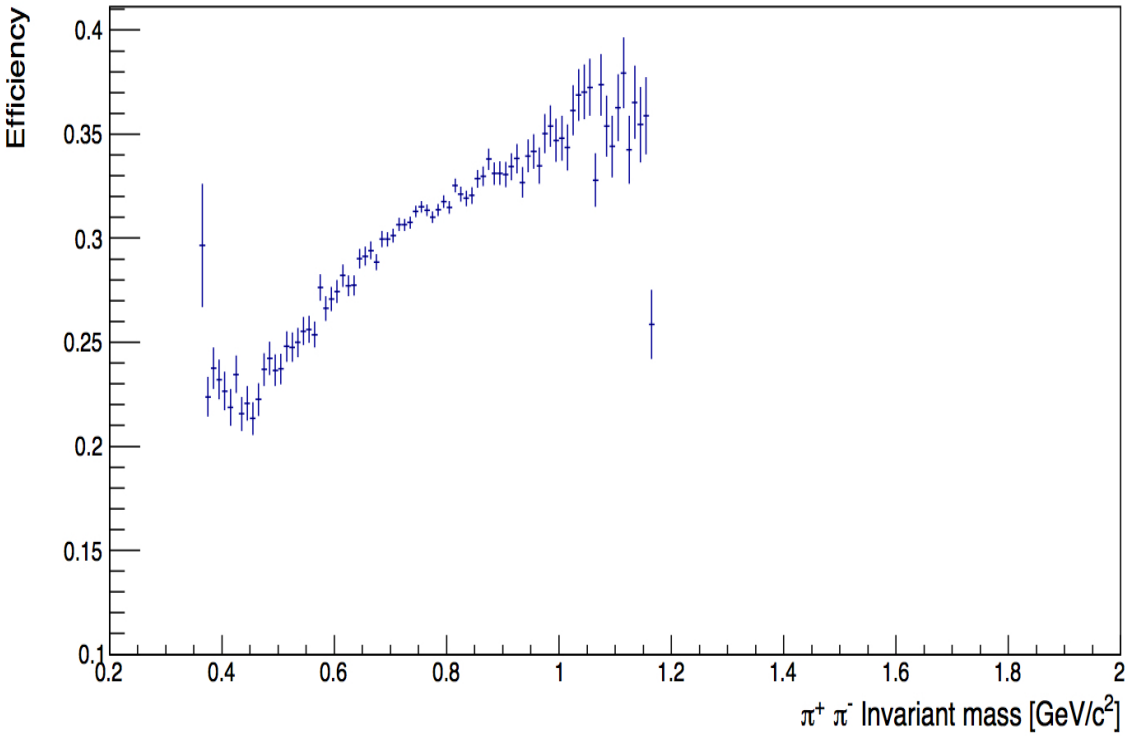

(b)

Figure 3.3: (a) ρ resonance peaks constructed using both generated and reconstructed MC. (b) Efficiency calculated bin by bin using the peaks in (a) via $\epsilon = \frac{Rec}{Gen}$.

figure 3.2 shows, the dependence on invariant mass is most prominent in the low p_t regions.

This also implies that one further correction is required when fitting these desired resonance peaks. Therefore, within the fitting process shown in figure 3.11, the Breit-Wigner shapes used are multiplied by this invariant mass dependent efficiency to account for the distortion away from a pure relativistic Breit-Wigner shape due to the reconstruction of the spectrum. This is in contrast to scaling the magnitude of the peak by a single efficiency factor which is usually satisfactory for studies of narrower peaks.

Since no official MC production exists for this set-up that includes the less known f_0 and f_2 particles, the efficiency of detecting these particles had to be estimated by using the efficiency of π tracks within the same mass range. This should be a fair estimation at least for the f_0, since it, as well as the residual background, has a $J^{PC} = 0^{++}$, and will therefore be subjected to similar acceptance requirements. Using this assumption, the efficiency calculated in plot 3.2 is obtained and is used within this analysis to produce the spectra seen in figures 4.27 and 4.28.

3.2.3 Testing the fitting process

The simulated π^+ π^- invariant mass spectrum, shown in figure 3.4a, exhibits similar features to the spectrum obtained from the real data fitting process, shown in figure 3.11. These features most importantly include the non-resonant background and

Table 3.1: Comparison between extracted MC ρ yield after efficiency corrections and true generated MC ρ peak yield.

	Extracted value	True MC value
Integral of peak	1326000 ± 4000	1332000
Central mean value (GeV/c^2)	7.753 ± 0.003	7.750

these contributions to the spectrum, such as the ω and η reflections, i.e features resulting from the three body decays, as discussed in section 3.4.

The MC study was useful in identifying each of these different components within the spectrum; this was done by singling out the components via their origin, i.e. the mother particle from which the π^+ and π^- decayed. This was necessary to confirm the shapes of these different components within the spectrum as well as to estimate their relative magnitudes compared to the overall spectrum. As such, figure 3.4a displays the shape and magnitude of each of the components, taken directly from the MC, alongside the estimated shape and magnitude of each of the components as computed from the fitting process when applied to this spectrum.

The fitting process used for the data sample was tested on the reconstructed spectrum created from the MC sample. The ρ peak within this spectrum was extracted by this fitting process and corrected for efficiency by using the efficiency calculated in figure 3.3 and compared to the original generated ρ peak as seen in figure 3.4a. This is further seen in figure 3.4b, which shows the ratio of the extracted ρ after the efficiency corrections and the original MC generated peak.

The extracted yield of the corrected ρ peak in figure 3.4b is also checked against the generated peak yield in table 3.1.

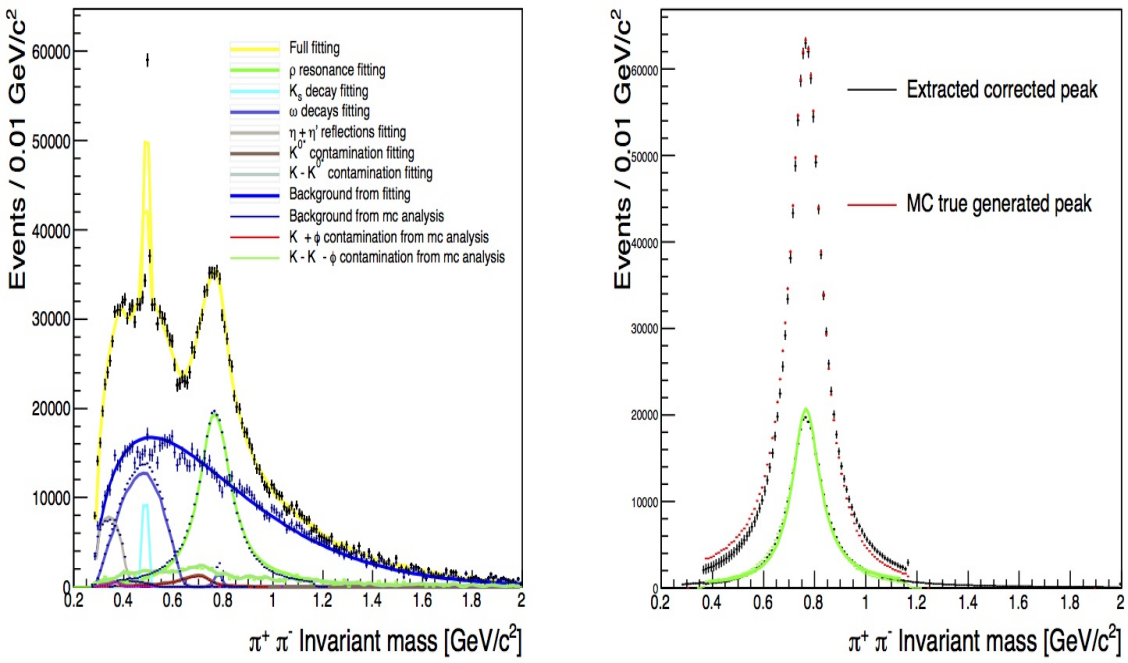

(a)

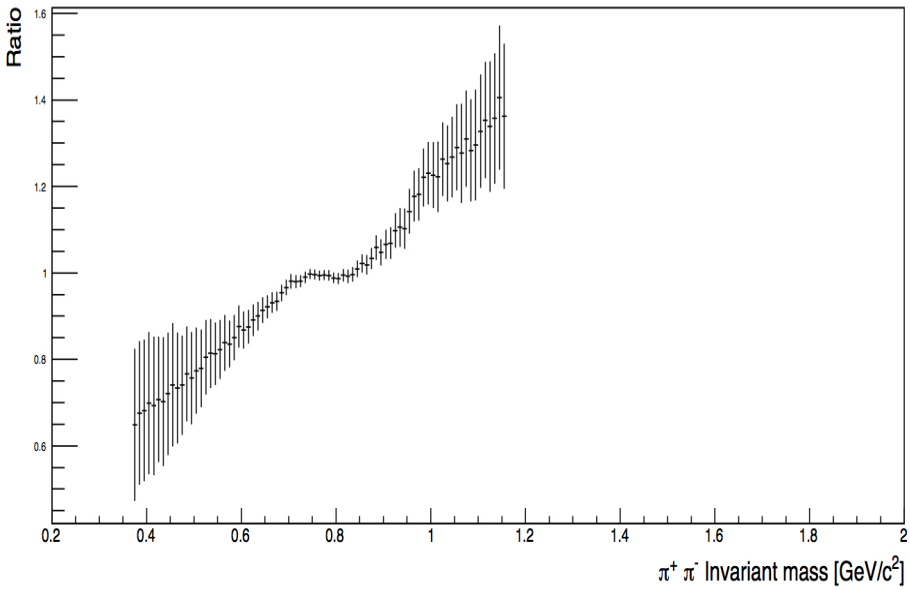

(b)

Figure 3.4: ((a) Left) MC spectrum fitted with the same fitting process used in figure 3.11 (minus the f_0 and f_2 peaks). ((a) Right) extracted and efficiency corrected ρ peak as compared to the original generated MC ρ peak. (b) Ratio of the extracted corrected ρ peak from the fitting process and the original generated MC ρ peak.

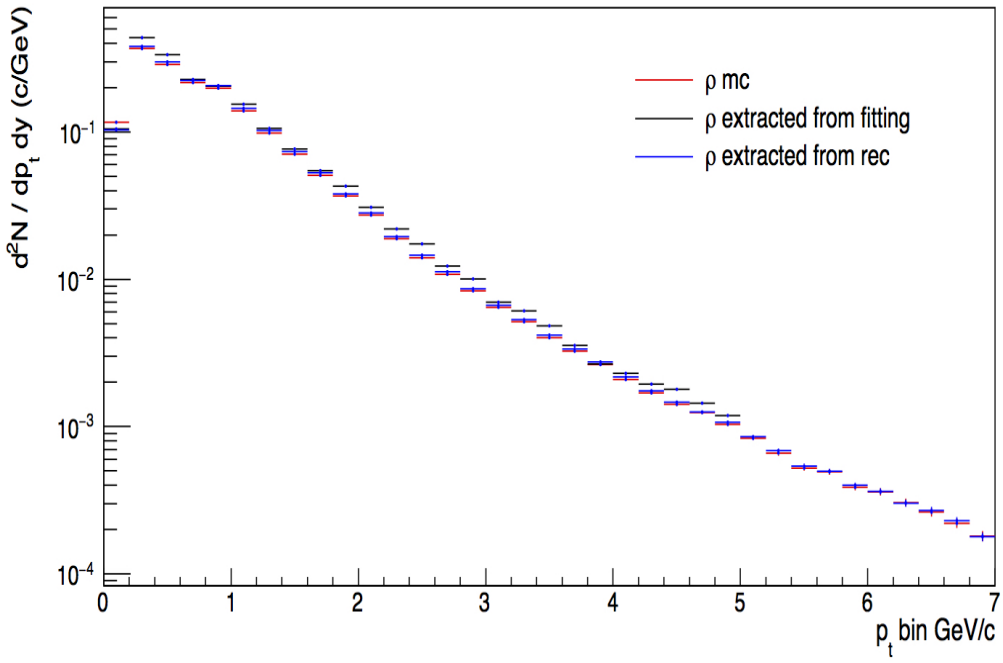

Figure 3.5: ρ spectrum extracted from the MC fitting process shown in figure 3.4a as compared to the ρ spectrum obtained by integrating the ρ peaks generated in the MC study as well as the spectrum obtained by using the pure reconstructed ρ peaks after applying the efficiency corrections to them.

Using this fitting method the yield of the extracted ρ within MC can be obtained with a deviation less than one percent from the true value. However, even though the tested values shown in table 3.1 largely agree with the true values, the overall shape of the peak, as estimated by the fitting process, has a clear considerable invariant mass bias, as shown in figures 3.4a and 3.4b.

This yield check was also conducted on the numerous spectra when split into the chosen p_t bins; from this the ρ spectra were extracted using the normalisation and correction methods outlined in section 4.2. This extracted ρ spectrum was compared to the spectrum obtained by integrating the generated ρ peaks in the same p_t regions and can be seen in figure 3.5.

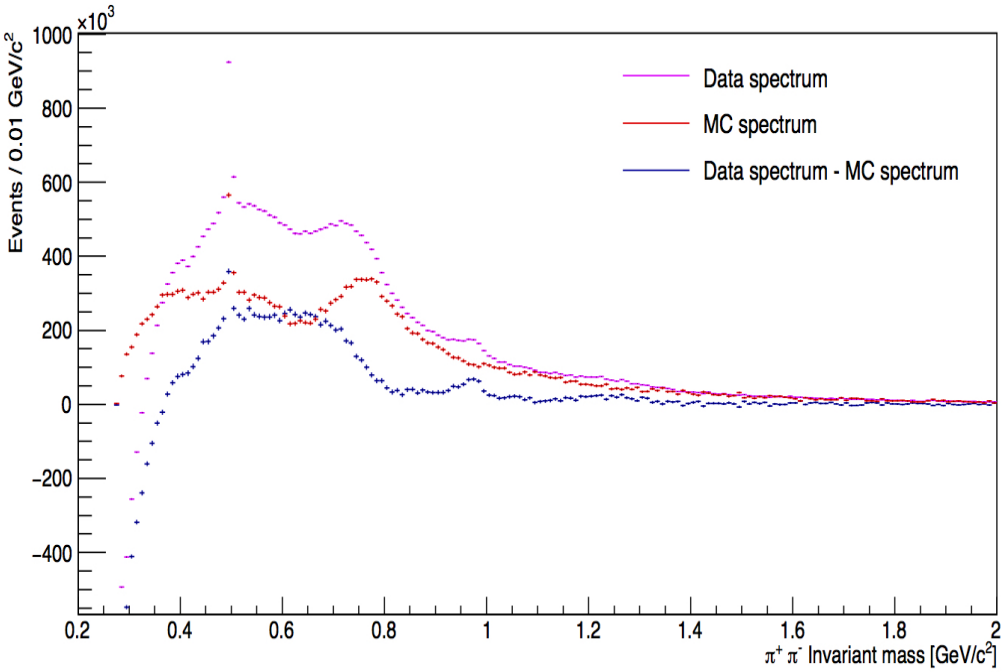

Figure 3.6: π^+ π^- spectrum obtained in data sample as shown in figure 3.11 alongside the π^+ π^- spectrum obtained in the MC sample as shown in figure 3.4a (normalised to the number of events) plotted alongside the difference between the two spectra.

3.2.4 Templates

As discussed in section 3.4, a number of components within the π^+ π^- spectrum could not be described with simple functions; therefore the shapes of these components needed to be described with the aid of the MC study.

The shape of the residual background shown in figure 3.4a is of a different form from the one seen by fitting the data (figure 3.11). Figure 3.6 shows the extent of this difference by comparing the spectrum obtained in MC with the spectrum obtained in data (after combinatorial like-sign background is removed from both and the MC is scaled to reflect the difference in the number of events between the data and MC samples).

This difference implies a problem with using equation 3.7 solely to describe the residual background. This is further highlighted as tests to fit the π^+ π^- spectrum obtained in data (figure 3.11) using only equation 3.7 to describe the residual background resulted in sub-par fitting of the spectrum.

Therefore, this difference between the MC and data spectrum is used as a template and added as an additional component to the residual background function. The template was truncated at an invariant mass value of 0.9 GeV/c^2 to remove contributions from $f_0(980)$ and $f_2(1270)$ peaks.

This difference is estimated for each p_t and then used as a template within the fitting, alongside the other MC templates discussed below. As shown in figures A.1 and A.2 as well as figures A.6 and A.7, this component dominates the spectrum in the low p_t regions and decreases to $\sim$ zero in the higher p_t regions, showing the discrepancy between data and the MC sample is the result of a mismatch at these low p_t values. This mismatch also appears in other MC generators, such as Phojet.

Possible problems with using this approach include uncertainty in the MC generators to produce an accurate representation of the p_t dependence of this effect. It can also be questioned as to how the components within the spectrum are represented within the MC and how this can affect the production of the template. However, as seen in figures A.6 and A.7, this effect is p_t dependent and as such becomes less dominant above $p_t \sim 0.8$ GeV/c. Therefore it is possibly not required in the fitting of this higher p_t region.

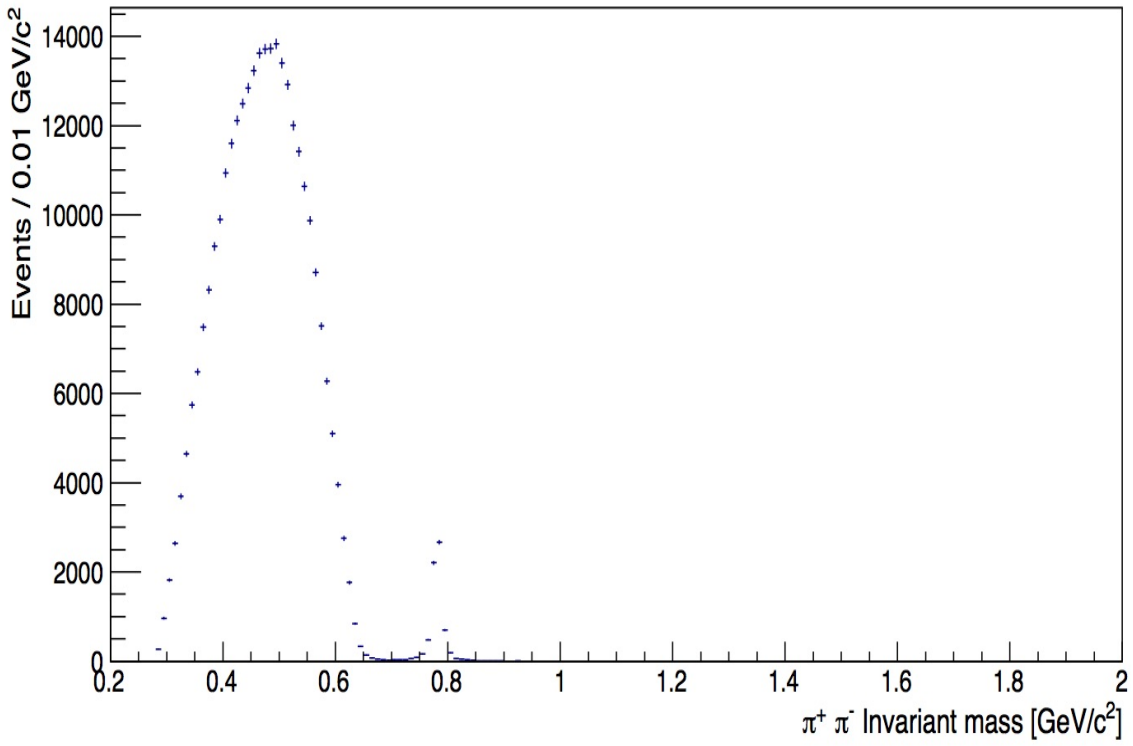

Figure 3.7: Identified ω (782) decay contributions to the π^+ π^- spectrum as seen within the MC sample.

The ω (782) reflection is another example of a feature whose shape could not be described by a continuous function within the fitting process. As such, a template for this feature was obtained from this MC study and used as a template within the fitting process of the real data set as seen in figure 3.11. The template used for this feature, for the p_t integrated spectrum, is shown in figure 3.7 and was obtained by identifying π^+ and π^- pairs that originated from the same ω mother in π^+ π^- π^0 decays. Figure 3.7 also shows the ω resonance decaying to π^+ and π^- between 0.7 and 0.8 GeV/c^2. This component of the spectrum was also taken from this template, thus allowing a smooth representation of this component within the fitting process throughout the p_t regions.

This method also applies to the η and η' (958) reflections identified within the MC

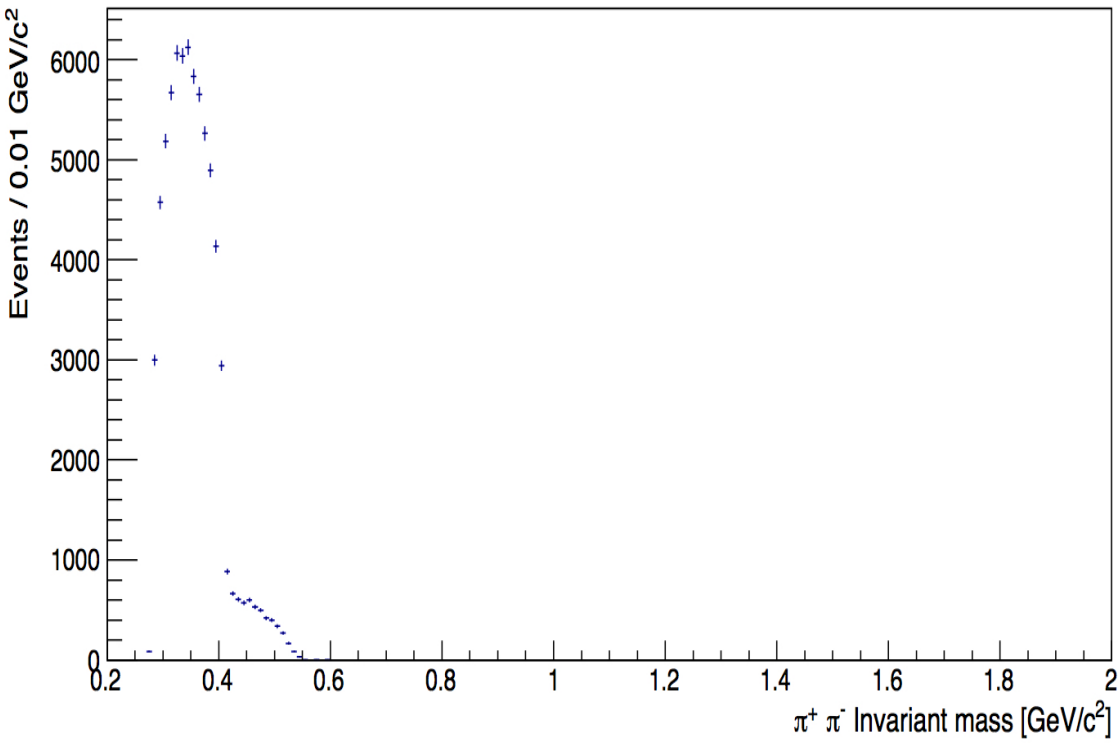

Figure 3.8: Identified η decay contributions to the π^+ π^- spectrum as seen within the MC sample.

study as shown in figures 3.8 and 3.9, for the p_t integrated case.

All of these templates were used within the fitting process displayed in figures 3.11 and 3.4a and the magnitudes of these templates were set as variable parameters within the fitting process.

A final contribution that required a MC template to fit the data spectrum comes from the misidentification of Kaon tracks as Pion tracks within the PID method. The shapes of these templates were estimated by allowing K tracks to be misidentified as π tracks within the MC study (non perfect PID) by simulating a standard cut of 3 n_σ on the expected value of the $\mathrm{d}E/\mathrm{d}x$ measurement in the TPC. This contaminated spectrum could then be compared to a non-contaminated (perfect PID using MC

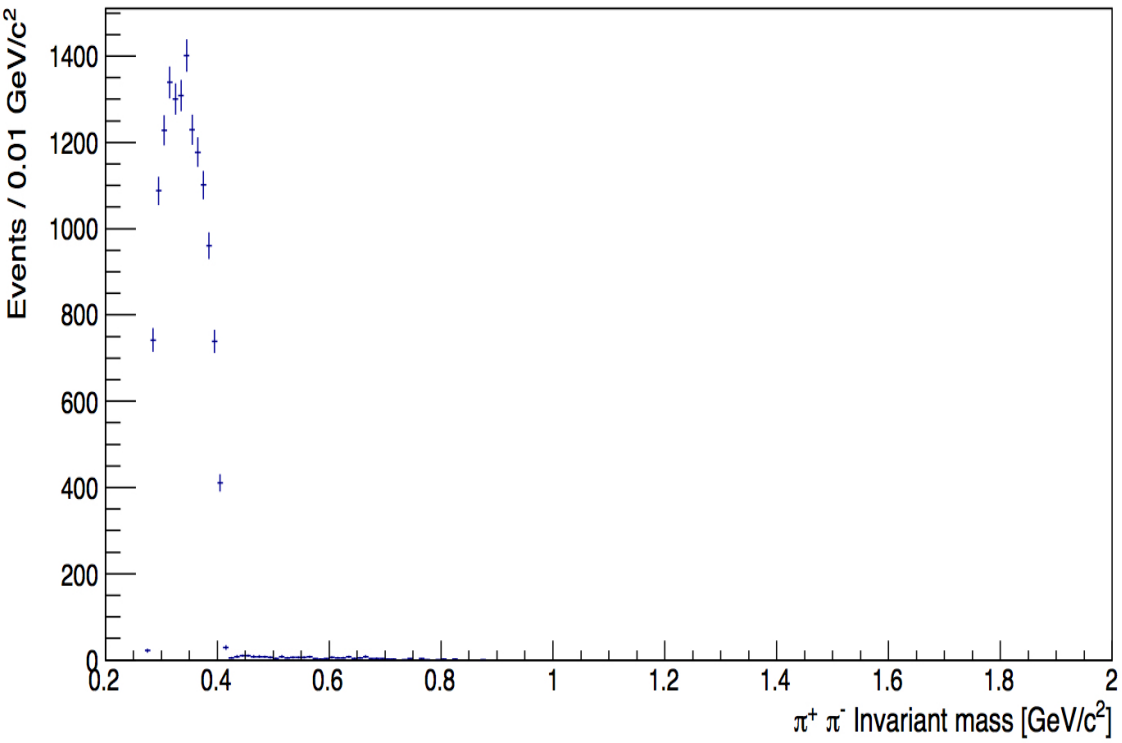

Figure 3.9: Identified η' (958) decay contributions to the π^+ π^- spectrum as seen within the MC sample.

truth information) spectrum to give an estimate of the contamination resulting from the PID method. Specific components of this contamination could also be singled out by identifying the mother particle of the misidentified K tracks.

The templates used for the p_t integrated spectrum are shown in figure 3.10. This component was treated as three different components within the fitting process. The constraints on these templates is described in section 3.4.1.

The contamination template was split to allow components originating from known decays to be fitted independently; these included the K^* (892) resonance decaying to $\pi^{\pm}$ $K^{\mp}$ daughters where the K decay product is misidentified as a π particle within the PID, resulting in a deformed shape and magnitude of this peak. The

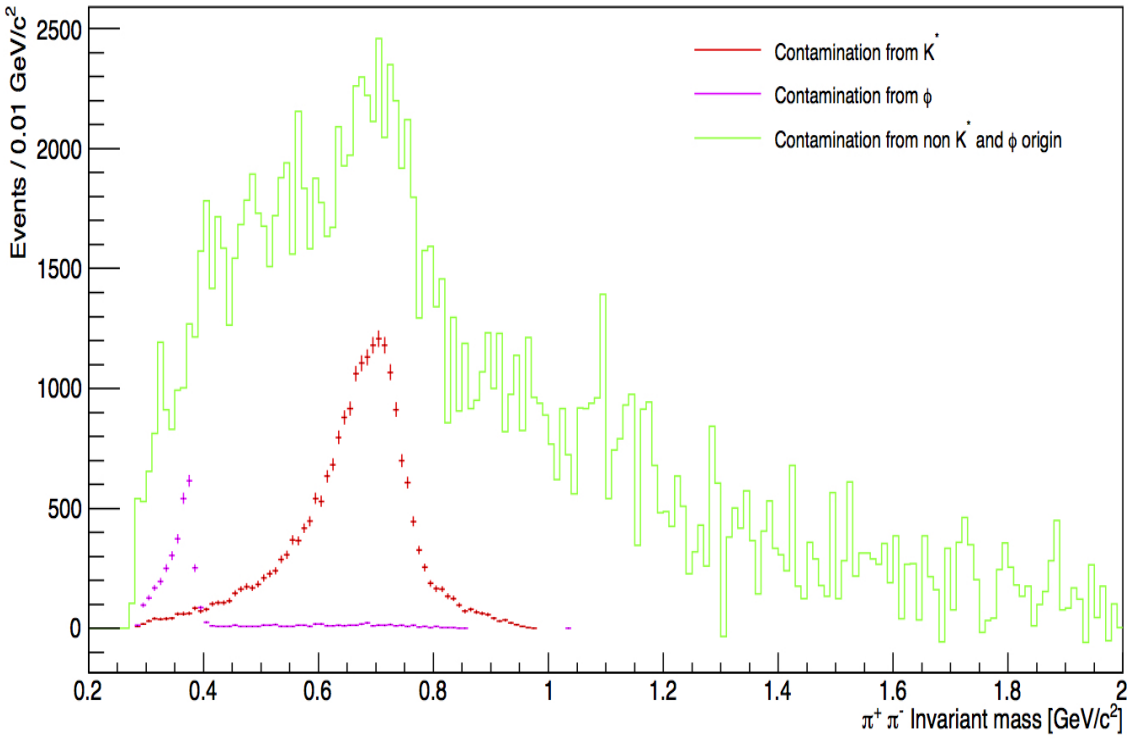

Figure 3.10: Identified contamination contributions to the π^+ π^- spectrum as seen within the MC sample.

other distorted resonance component is the ϕ (1020) decaying to K^+ K^- where both K decay products are misidentified as π tracks; this results in a smaller peak in the low mass region of the spectrum. The remainder of this contribution was treated as one broad background template alongside the K^* and ϕ templates.

These three different components were treated separately largely due to the position of the K^* component, which is situated under the ρ mass region; as such it was necessary to ensure that the fitting of this component was not biased towards the fitting of the rest of this contamination contribution.

Table 3.2: Branching ratios of each of the extracted resonances in the $\pi^+\pi^-$ channel [1].

Resonance	BR($\pi^+\pi^-$)
$\rho(770)$	$\sim 100\%$
$f_0(980)$	Dominant (Taken to be 58% in most Pythia builds [71] and this analysis)
$f_2(1270)$	$84.8^{+2.4}_{-1.2}\%$

3.3 Signal Extraction

The spectrum resulting from the removal of the combinatorial background (with the like-sign method taken as the default in this analysis) is shown in figure 3.11; this figure has also been fitted via the fitting procedure described in section 3.4, thus showing the different identifiable components within the spectrum. Figure 3.12 shows the ratio of fitted spectrum over the fitted function.

3.4 Spectrum components

This process is applied to the all the spectra obtained, by splitting the data into different p_t regions in order to extract the desired resonances for each region. The fitting process applied to each of these regions is shown in the appendix figures A.1 and A.2.

The desired resonances that were extracted from the spectrum are the $\rho(770)$, the $f_0(980)$ and the $f_2(1270)$, and appear as wide prominent peaks within the spectrum. The branching ratios of the desired resonances to the π^+ π^- channel are listed in table 3.2.

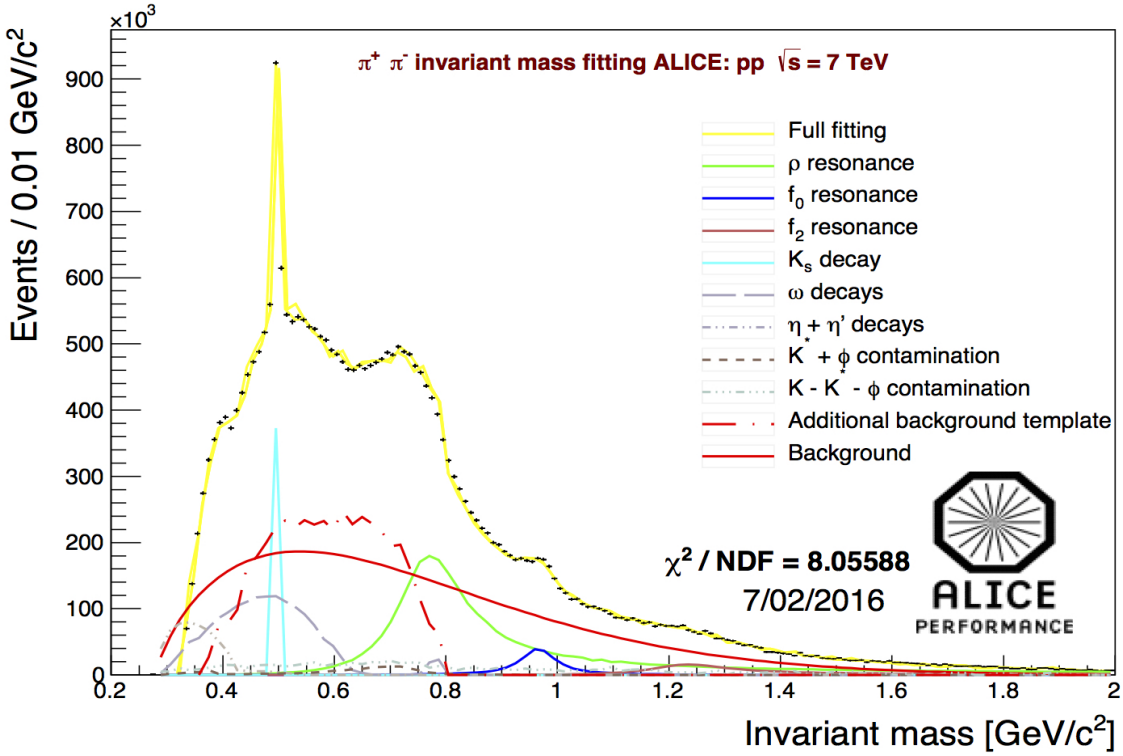

Figure 3.11: Plot produced by author showing the full fitting process of the π^+ π^- spectrum after the like-sign combinatorial background has been removed from the π^+ π^- spectrum shown in figure 3.1.

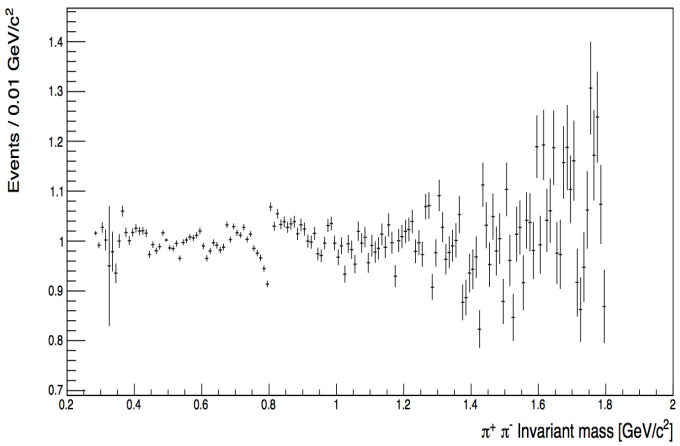

Figure 3.12: Plot produced by author showing the ratio of the π^+ π^- spectrum over the full fitting process of the applied in figure 3.11 as a function of the invariant mass.

The only other pure resonance to appear in the spectrum is the ω (782), located in the same mass region as the ρ peak. However, due to its small branching ratio to the π^+ π^- channel ($\sim 1.53\%$), its magnitude is significantly smaller than that of the ρ, imposing a small but not negligible effect on the fitting of the ρ peak.

In the lower mass region of the spectrum there are also three components attributed to the reflections of three-body particle decays, two of which (the π^+ and π^- decay products) are measured in the construction of the spectrum. These reflection components appear as non trivial peaks in the spectrum, due to incomplete measurement of the total energy from these decays, resulting from non-measurement of the third decay product. The largest of these are the reflections from the ω (782) decaying to $\pi^+\pi^-\pi^0$, the η decaying to $\pi^+\pi^-\pi^0$, and η' (958) to $\pi^+\pi^-\eta$.

The sharp peak seen in the ~ 0.5 MeV/c^2 region of the spectrum was due to K^0_s decays with small DCA tracks. This was a very localised peak, only affecting $\sim$ three of the bins in figure 3.11.

The non-resonant portion of the spectrum was defined to be the residual background, as it did not originate from either resonances or any other identifiable source other than mini-jets [72] i.e correlated tracks but not associated with a resonance decay or reflection.

A number of different templates and fitting functions were used to describe each of these features. The extracted resonances were each described by a relativistic Breit-Wigner function [73] as given by equation 3.2,

$$F_M = \frac{M_0 M \Gamma(M)}{\pi \left(M^2 - M_0^2\right)^2 + \left(M_0^2 \Gamma^2(M)\right)}, \tag{3.2}$$

where M_0 is the mean of the Breit-Wigner peak (mass value of the resonance), M is the $\pi^+ \pi^-$ invariant mass value and $\Gamma(M)$ is the momentum dependent width of the peak.

In this case the momentum dependence of the width can be described by equation 3.3,

$$\Gamma(M) \approx \Gamma_0 \left(\frac{q}{q_0}\right)^{2l+1} \frac{M_0}{M}, \tag{3.3}$$

where q is the momentum of the decay products in the rest frame of the mother particle, q_0 is the momentum of the decay products when $M = M_0$, Γ_0 is the constant width of the resonance and L is the relative angular momentum of the resonance ($l = 1$ for ρ, $l = 0$ for f_0, and $l = 2$ for f_2). Also, M_0 and M retain their meanings from equation 3.2.

This width correction is important for resonances with larger widths or near thresholds, as this dependence can affect the central mass position of the resonance peak [73].

Another element which will distort the ρ resonance peak from a true relativistic Breit-Wigner shape comes about due to Bose-Einstein correlations. The attraction acting between identical pions that have similar phase space can have a large effect

on the phase space of the π^+ π^- spectrum.

Due to the ρ resonance's short lifetime (< 1 fm) it is much more susceptible to these effects than the other other resonances studied in this analysis. The decaying charged pions more susceptible to influences from directly created pions.

This effect was studied at LEP [74] and observed at STAR [[32],[33]]. It was also found that the enhancement by Bose-Einstein correlations in the phase space density (Q) distribution of a π^+ π^- system was greatest in the region below 0.4 GeV/c^2 [75]. This coupled with the observation that the cross over region for this introduced enhancement (and reduction in Q above ~ 0.8 GeV/c^2) lies very close to the ρ peak central value. This broadens the tails of the ρ mass peak and shifts the central mean value to a lower mass (by $\sim$ MeV/c^2). The effects on the ρ peak due to the position of the cross over region is also something that is unique to this peak within this analysis.

This effect can be accounted for by adding a Söding term [76]. This term is given by equation 3.4,

$$I_M = A\frac{M_0^2 - M^2}{M\Gamma(M)}F_M \equiv I_0 F_M, \tag{3.4}$$

where A is a free magnitude parameter for this correction, F_M denotes the relativistic Breit-Wigner shape used to descibe the peak and M_0 and M retain their meanings from above.

The Söding term is solely a phenomenological description of the data, which happens to reproduce the effect of the residual Bose-Einstein correlations in the spectrum. Therefore within this analysis this correction is applied to the fitting by using equation 3.5,

$$F(M) = F_M\,(1 + I_0) = F_M + I_M, \tag{3.5}$$

where equations 3.2 and 3.4 are combined to give a corrected fitting shape.

At LEP parameter A was found to be ~ 1 at low momentum and ~ 0 for high momentum. However, this correction, or similar, was not applied in the STAR analysis and, as explained in [32], is a likely reason for the modifications to the ρ mass values they observe. Due to the limited phase region that is effected by Bose-Einstein correlations, this correction term was only applied to the ρ peak and not the other resonances.

Figure 3.13 shows the ρ peak obtained through the MC study (discussed in section 3.2) fitted with equation 3.2 as compared to fitting the same peak with the Söding interference term (equation 3.4) combined with equation 3.2 as seen in equation 3.5.

As seen in table 3.3 using the Söding correction results in a much better χ^2 / NDF and also a closer central value to the well known Particle-Data-Group (PDG) mass for the ρ (~ 775.49 MeV/c^2) with the width value remaining largely unchanged.

By splitting the ρ peak MC statistics into different p_t regions figure 3.14 shows how

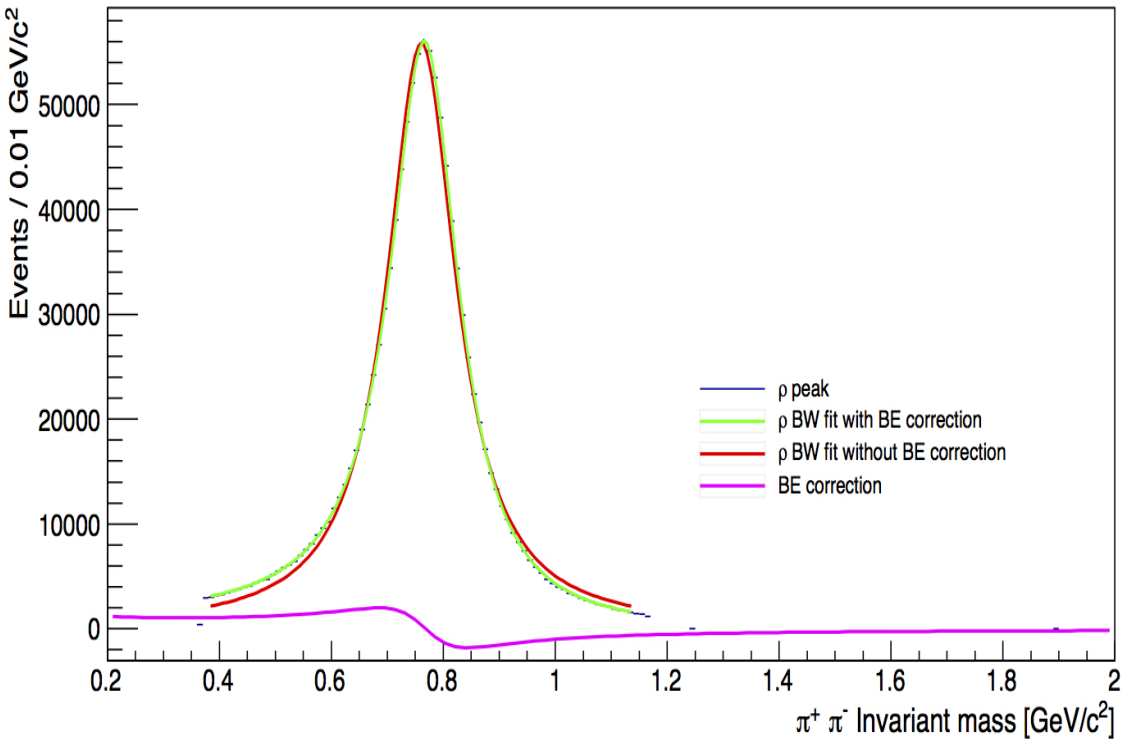

Figure 3.13: MC ρ peak fitted with equation 3.2 and with equation 3.5 (with Söding interference).

Table 3.3: Comparison between fitted MC peak with and without Söding correction.

	With Söding correction	Without Söding correction
Mean (MeV/c^2)	768.72	760.66
Width (MeV/c^2)	150.68	149.70
χ^2 / NDF	118 / 72	8532 / 73

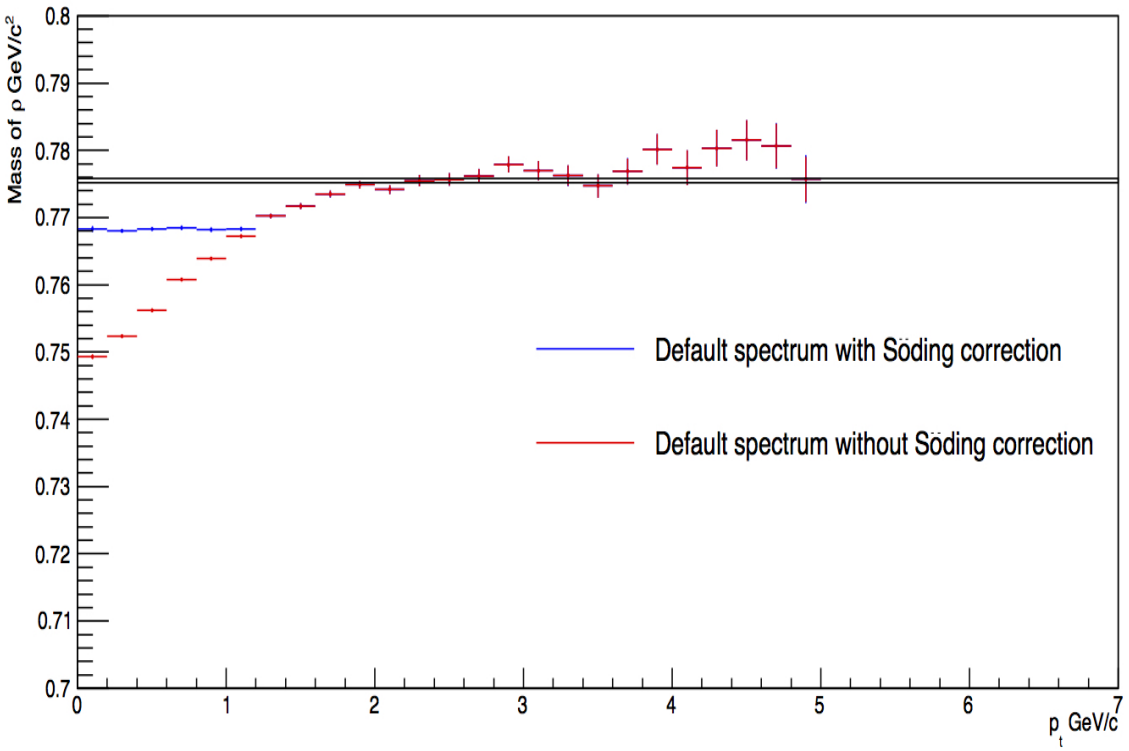

Figure 3.14: MC ρ peak fitted with equation 3.2 and with equation 3.2 with Söding interference in different p_t regions ranging from 0 to 5 GeV/c.

much of an effect this correction has as a function of p_t.

Figure 3.14 shows a clear underestimation of the ρ mass value when fitted solely with equation 3.2 at low p_t values; this is corrected somewhat by instead fitting the ρ peaks with equation 3.5.

This effect can also be seen with the mean values of the ρ peak in the data extraction as shown in figures A.1 and A.2; figure 3.15 shows the mass values of the ρ as a function of p_t with and without the term.

As shown in figure 3.15, fitting the spectrum without this term causes the mass of the ρ to be underestimated in every p_t region; this, coupled with the improved χ^2 value shown in table 3.3 is reason enough to include this correction factor as default

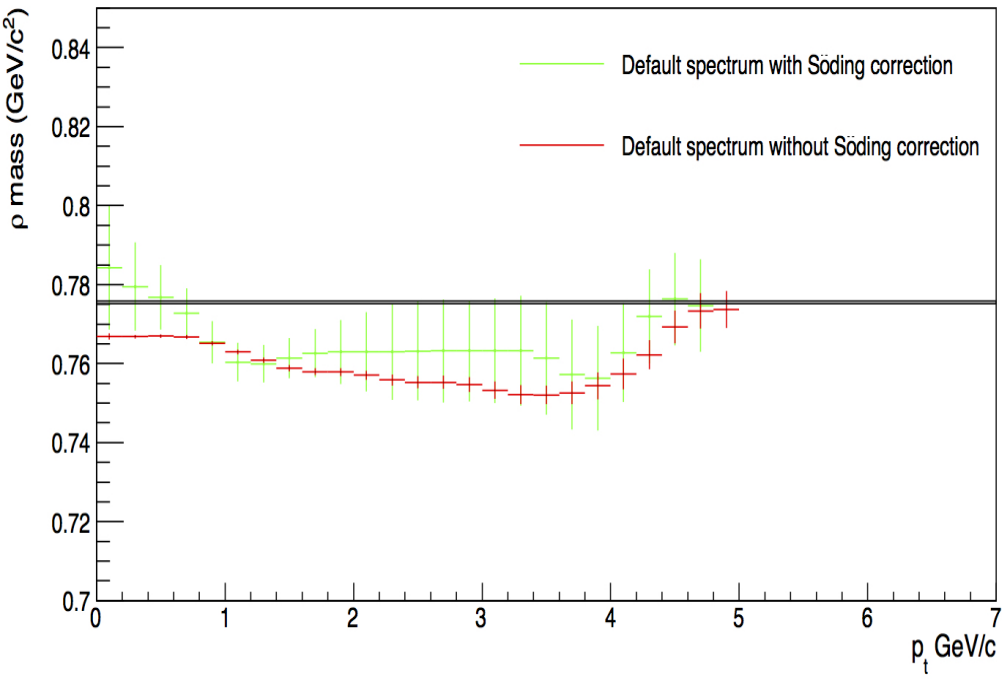

Figure 3.15: ρ peaks extracted from data sample fitted with equation 3.2 (with statistical errors only) and with equation 3.2 with Söding interference (with both statistical and systematic errors combined) in different p_t regions ranging from 0 to 5 GeV/c.

in this analysis.

The effects due to the available phase space were corrected for by using the same method applied by the ρ STAR analysis [32]; the relativistic Breit-Wigner shape of the resonance signals was multiplied by a phase space factor (Boltzmann factor) given by equation 3.6,

$$PS = \frac{M}{\sqrt{M^2 + p_t^2}} \exp - \frac{\sqrt{M^2 + p_t^2}}{T}, \tag{3.6}$$

where M retains its above meaning, p_t is the transverse momentum and T is the kinetic freeze-out temperature set to $T \sim 160$ MeV in the proton - proton study and ~ 120 MeV in the heavy ion study. There was no real justification from the STAR

analysis [32] for this correction, but it was considered for a systematic check of the results within this analysis as seen in section 4.3.1.1 where the inclusion of this phase space correction was taken as default with its exclusion used as a systematic check.

The remaining non-resonant component (residual background) was described by the function given in equation 3.7 [72], as it was found to best describe this background when it was recreated in the MC study seen in section 3.2,

$$B(M) = (M - 2M_{\pi})^{\alpha}\, e^{\beta+\gamma M+\delta M^3}, \tag{3.7}$$

where M_{π} is the mass of the charged pion and α, β, γ and δ are the free fitting parameters. An example of this function describing the p_t integrated background within the MC study is shown in figure 3.16. The evolution of this background as estimated in the MC study in each p_t region is shown in figures A.4 and A.5, each bin is fitted with equation 3.7.

As shown in figure 3.11 however, this shape was not completely representative of the residual background shape observed within the $\pi^+\,\pi^-$ spectrum obtained in real data, thus an extra component was added to account for this difference within the fitting process. This is discussed further in the section 3.2.4.

The shapes of the three-body decay components were taken from MC templates as discussed in section 3.2.

The final contribution shown in figure 3.11 comes from the contamination of charged

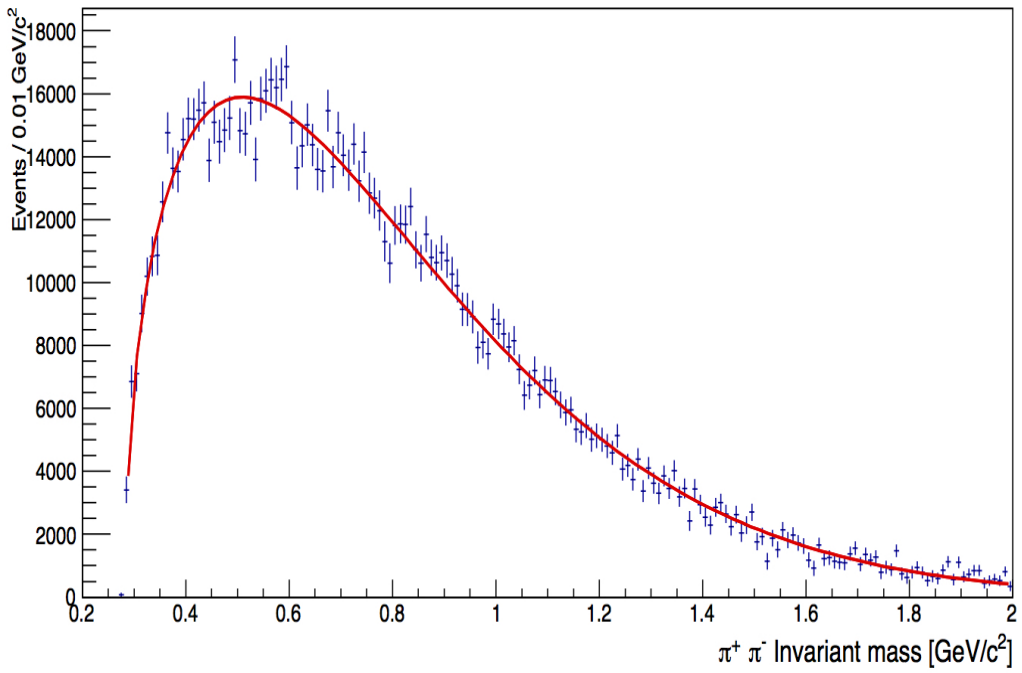

Figure 3.16: Fitting of non-resonant background using the function given in equation 3.7. Background estimated from MC tracks not decaying from identified components of the spectrum.

K tracks that are misidentified as π tracks in the TPC PID method. This was accounted for by the addition of three extra components within the fitting process.

The origin of these contaminations was mostly due to the crossings of expectation values of the energy loss $\mathrm{d}E/\mathrm{d}x$ for pions with the expectation values for other stable particles as seen in figure 2.6, this is mainly due to the fact that the majority of stable particles measured within a given event are pions due to their low mass and stability.

However, this fact has the added benefit of allowing the π^+ π^- spectrum to be constructed without any PID cuts with manageable contaminations from non-pion tracks (mostly from kaons which are the second most common stable particle tracks measured).

The K track contamination was described by three separate components: one for tracks which originated from the K^* resonance, another for the tracks which originated from the ϕ resonance and a last component representing the rest of the spectrum resulting from K tracks not including those that originated from the K^* or ϕ resonances. All three component shapes were estimated in the MC study.

3.4.1 Constraints applied to the fitting process

Constraints on the total fitting were as follows.

- The ρ resonance central mass value was set as a free parameter, with the width parameter fixed to the value obtained from fitting the MC ρ peaks in both the reconstructed MC for the efficiency uncorrected peaks and the generated MC for the efficiency corrected peaks. These width values are shown in figure 3.17, which also shows the mass values alongside the width values extracted from the generated and reconstructed MC ρ peaks and their evolution as a function of p_t.

- The f_0 resonance central value was set as a free parameter and the width was set so as not to deviate from constrained limits of 40 and 100 MeV/c^2 as documented in the PDG. This was done so as not to allow systematic effects to dramatically affect the extracted yield of this peak by causing the width of the peak to change by a large amount.

- The f_2 resonance central value was set as a free parameter and the width was

completely fixed to the PDG value of 0.1851 GeV/c^2.

- The K_s decay central value and width value were fixed to the PDG values of mass $\sim$ 498 MeV/c^2 and width $\sim 7 \times 10^{-6}$ eV/c^2.

- The ω reflection magnitude was constrained so that the extracted raw yield for this peak normalised to the number of events was within 10% of the same ratio in the MC study. Thus by using this constraint the evolution of the yield of this component would be stable as a function of p_t. The extracted magnitude of this component within the MC study as a function of p_t is shown in figure 3.18a.

- The ω resonance was also fitted using a MC template. This template and ω reflection template were created together and shared the same constraints. In this way this component would also evolve smoothly as a function of p_t. This was important since the magnitude of this component would affect the raw yield extracted from the fitted ρ peak as both of these components exist within the same mass range (ρ mass $\sim$ 775 MeV/c^2 and ω mass $\sim$ 782 MeV/c^2).

- The K contamination magnitudes were constrained so that the yield of this background normalised to the number of events was within 10% of the same ratio in the MC study. Again this was to ensure that the evolution of the amount of K contamination was stable as a function of p_t. This was also important because much like the ω resonance component the deformed K^* constructed from the misidentified K tracks also lies within the ρ peak mass range. The extracted magnitude of this component within the MC study as a

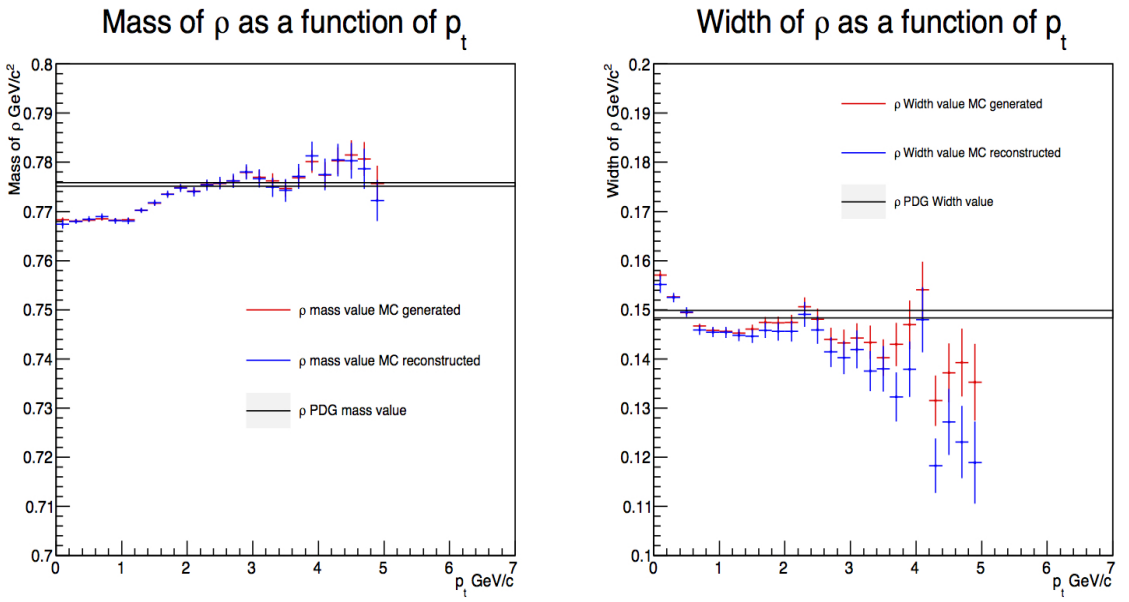

Figure 3.17: Mass and width values of the ρ extracted from fitting the ρ peak within the generated and reconstructed MC sets within the different studied p_t regions.

function of p_t is shown in figure 3.18b.

- The magnitude of the extra background template discussed in the section 3.2.4, was constrained so that the yield of this background normalised to the number of events was within 10% of the same ratio in the MC study. Again this was to ensure the evolution of this background component was stable as a function of p_t. The extracted magnitude of this component within the MC study as a function of p_t is shown in figure 3.18c.

The limits of these constraints were only met in the very low p_t regions and kept as constraints as a safety precaution in the higher p_t regions. This reinforced the assumption that all of the components discussed in section 3.3 encapsulated the whole of the spectrum in the studied mass region.

These extracted resonance peaks then required a correction to account for the de-

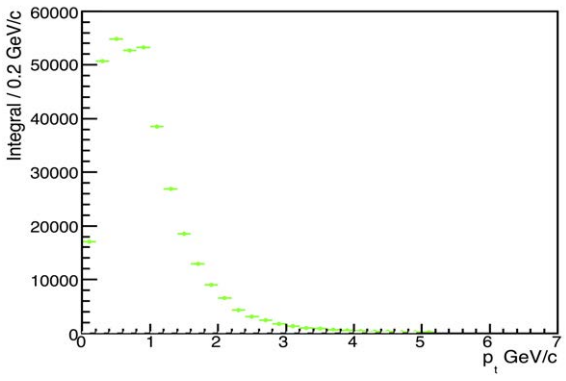

(a)

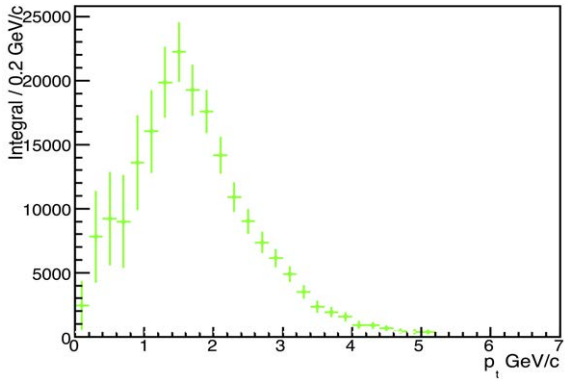

(b)

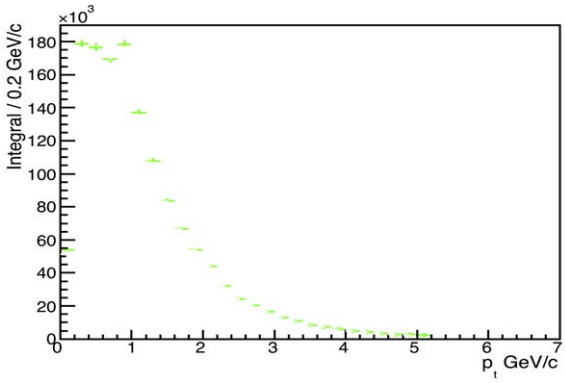

(c)

Figure 3.18: Extracted integrals from the templates acquired from the MC study in order to observe evolution of the templates as a function of p_t. The values of each p_t bin were used to constrain the MC templates within the data fitting process. (a) shows the evolution of the ω (782) template, (b) shows the contribution due to K contamination template and (c) shows the evolution of the extra background shape.

tector efficiency by the method outlined in section 3.2. After these corrections the peaks were refitted using the same modified relativistic Breit-Wigner shape discussed above (the combination of equations 3.2, 3.3 and 3.4); this was done to account for any shifts in mass value caused by a non-constant efficiency value as a function of invariant mass, again described in section 3.2.2. The corrected extracted peaks for the p_t integrated mass spectrum are shown in figure 3.19.

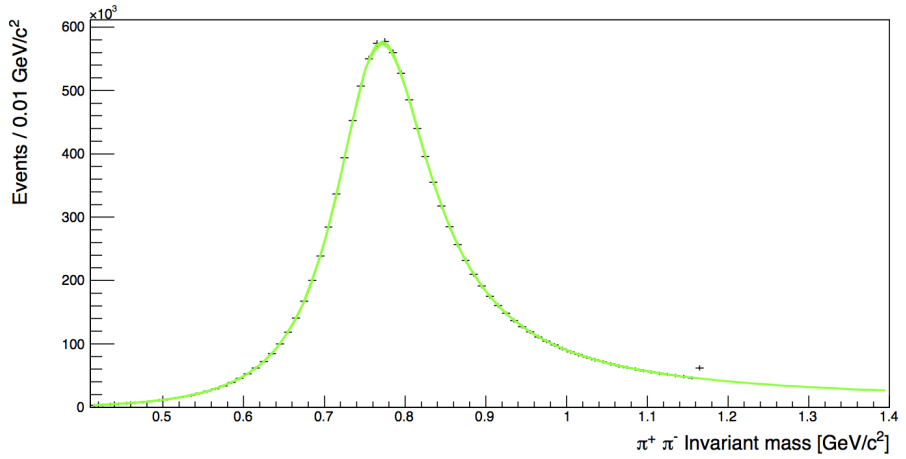

(a)

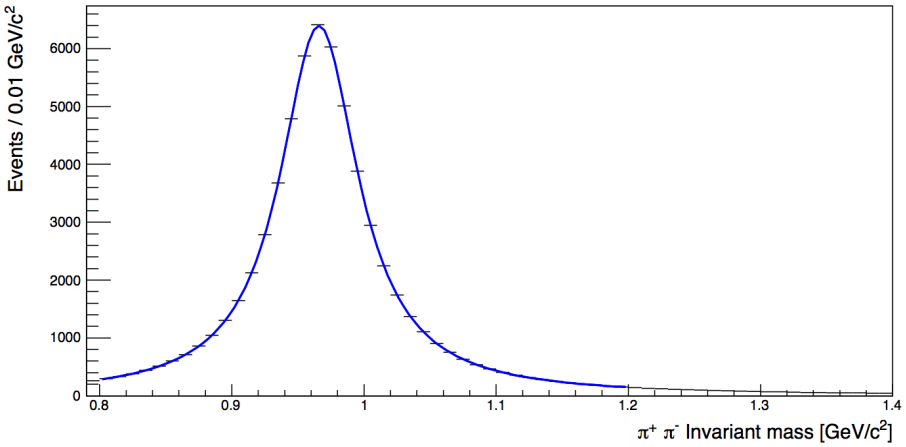

(b)

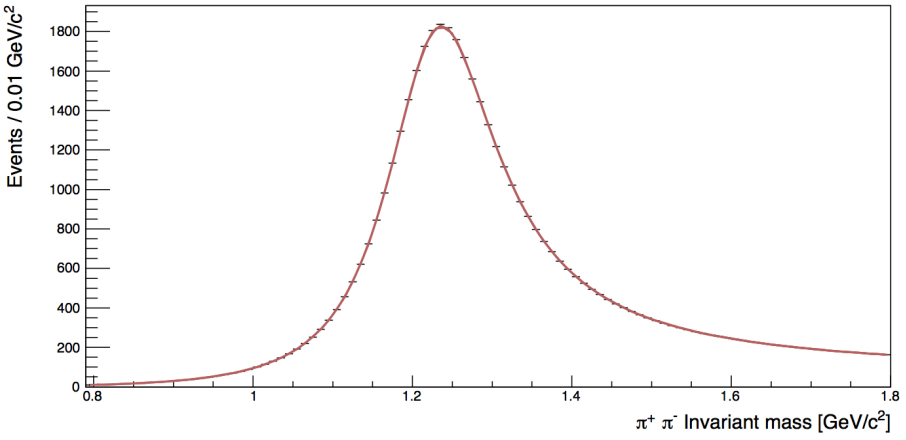

(c)

Figure 3.19: Refitting of the resonance peaks extracted within data sample using the fitting method outlined in section 3.4. Peaks include $\rho(770)$ resonance (a), f_0 (980) resonance (b) and f_2 (1270) resonance (c), after they have been corrected for the effects due to the acceptance efficiency as discussed in section 3.2.2.

CHAPTER 4

Results

4.1 Additional checks

A number of checks were conducted to ensure that the templates and constraints applied to the fitting process with the data sample are reasonable, especially when observed as a function of p_t.

The first check used the extraction of the K_s peak from the fitting process. To do this, the ratio of the raw number of K_s extracted over the number of events was calculated in both the MC and data studies and can be seen in figure 4.1.

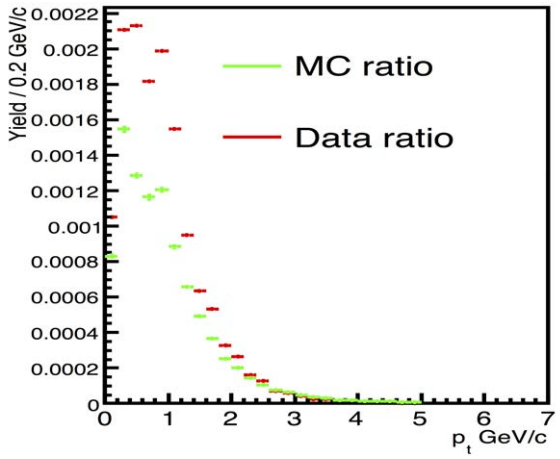

Figure 4.1: Extracted raw K_s yield relative to the total number of events from the fitting process in data p_t bins as compared to the reconstructed MC K_s yield in the same p_t regions.

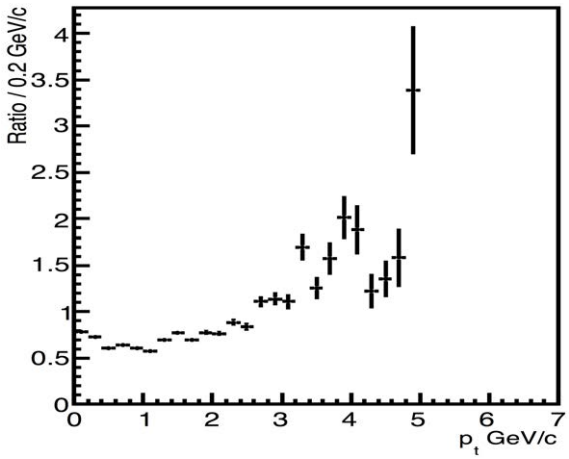

Figure 4.2: Ratio of reconstructed MC K_s yield over the extracted raw K_s yields from the fitting process in data in the same p_t regions.

The ratio of identified reconstructed MC K_s peak yield over the extracted K_s yield from the data fitting process is shown in figure 4.2.

As shown in figure 4.3 the Pythia tune used in this analysis (Perugia 0) underestimated the number of Kaons by $\sim 30\%$ to $\sim 40\%$, which is roughly the same amount in which the MC underestimated the extracted K_s in this analysis as shown in figure 4.2. Other tuning options shown in figure 4.3 are Phojet, Pythia D6T and Perugia 2011.

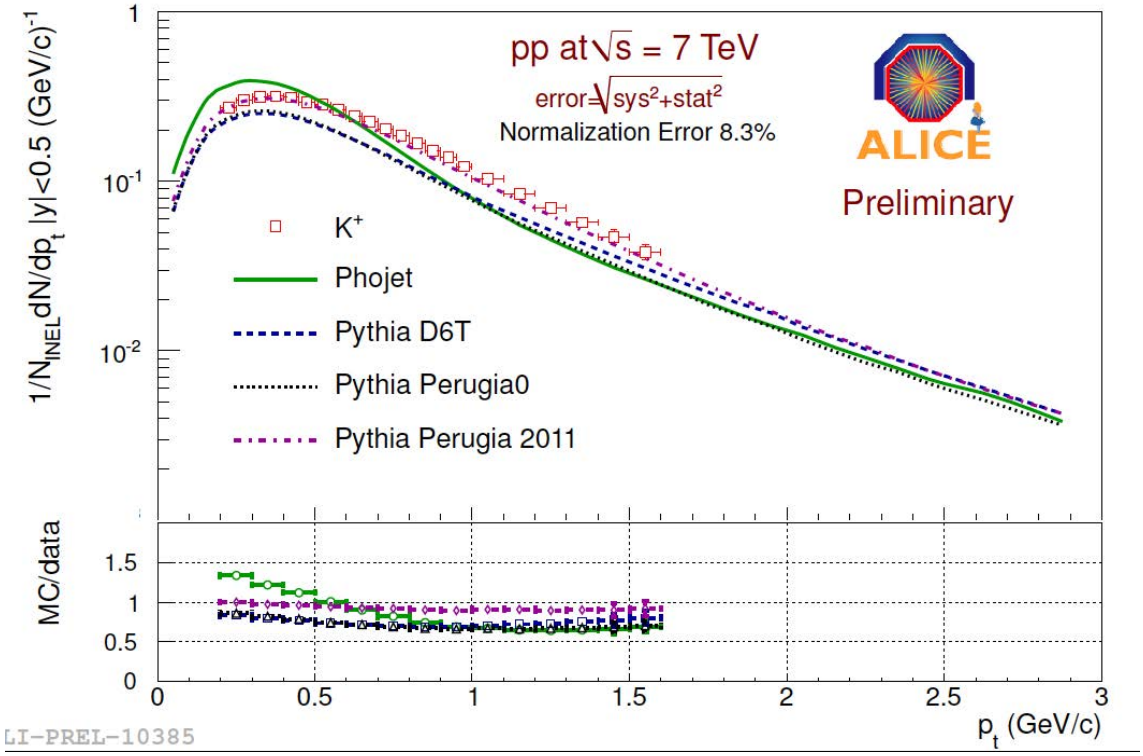

Figure 4.3: Extracted K_s yield from analysis in proton - proton collision at 7 TeV compared to a variety of different MC expectations of the K_s yield [77]

This same logic is also applied to the extraction of the K^* particle constructed from the misidentification of K tracks. For each p_t bin in the data fittings the yield of the K^* component is extracted; using this, the ratio of K^* over the number of events can be calculated in both MC and data as shown in figure 4.4.

The ratio of computed expectation yield of the K^* contamination over the measured yield of this contamination within the data fitting process is shown in figure 4.5.

As shown in figure 4.6 the Pythia tune used in this analysis (Perugia 0) also underestimates the number of K^* particle by roughly $\sim 30\%$ to $\sim 40\%$, roughly the same amount in which the MC underestimated the extracted K^* in this analysis as shown in figure 4.5. This is less consistent than for the K^* study.

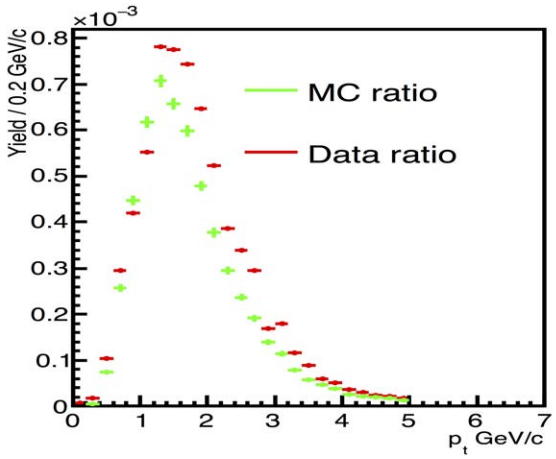

Figure 4.4: Extracted raw K^* yield relative to the total number of events from the fitting process in data p_t bins as compared to the reconstructed MC K^* yield in the same p_t regions.

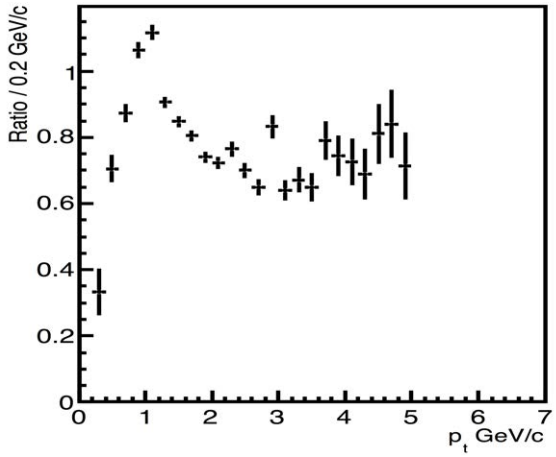

Figure 4.5: Reconstructed MC K^* contamination expectation yields over the extracted raw K^* contamination yields from the fitting process in data in the same p_t regions.

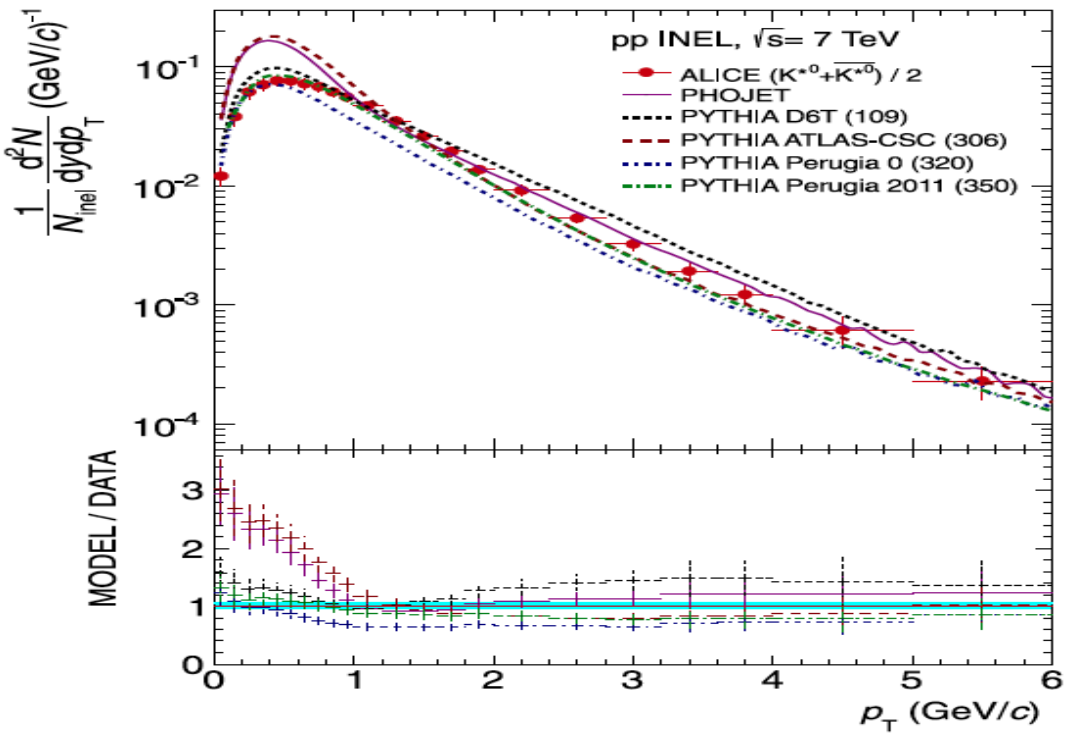

Figure 4.6: Extracted K^* yield from analysis in proton - proton collision at 7 TeV compared to a variety of different MC expectations of the K^* yield [78].

This strengthens the assumption that the fitting constraints applied within the analysis are a fair representation of the evolution of the different components as a function of p_t, since one of the tested components that is not constrained in the fitting process (K_s) shows the same behaviour when compared to the MC study as a constrained component (K^*).

4.2 Normalisation of Spectra

The extracted yields for each of the desired resonances in a given p_t bin (of width Δp_t) and in the rapidity range of $\Delta y = 1.0$ were normalised via equation 4.1 to obtain the absolute yields per inelastic collision,

Table 4.1: Branching ratios of each of the extracted resonances in the $\pi^+\pi^-$ channel [1].

Resonance	BR($\pi^+\pi^-$)
$\rho(770)$	$\sim 100\%$
$f_0(980)$	Dominant (Taken to be 58% in most Pythia builds [71] and this analysis)
$f_2(1270)$	$84.8^{+2.4}_{-1.2}\%$

$$\frac{\mathrm{d}^2N}{\mathrm{d}p_t\mathrm{d}y} = \frac{\epsilon \cdot \epsilon_{trigger} \cdot N_{raw}}{N_{events} \cdot BR \cdot \mathrm{d}p_t\mathrm{d}y \cdot \epsilon_{\frac{\mathrm{d}E}{\mathrm{d}x}}}, \tag{4.1}$$

where N_{raw} is the extracted minumim bias yield obtained from integrating the extracted distributions and ϵ is the efficiency corrections factor described in section 3.2.2. N_{events} is the total number of events used to create the full distribution ($\sim$ 35 million events) within the vertex cut, $\epsilon_{trigger}$ is the trigger selection efficiency for inelastic collisions for proton - proton collisions in ALICE (measured with a value of $0.852^{+0.062}_{-0.03}$ [79]) and BR is the branching ratio for the decay channel (the branching ratio of each extracted resonance can be seen in table 4.1).

$\epsilon_{\frac{\mathrm{d}E}{\mathrm{d}x}}$ is the energy-loss cut efficiency for a given resonance measured using the π^+ π^- channel. With an energy-loss cut of $A \leq x \leq B$ (where x is the normalised TPC energy loss) applied to all pion tracks in the TPC PID, the energy-loss efficiency for a single pion is given by the fraction of the area of a Gaussian with mean zero and variance one. The energy-loss efficiency of a resonance in the π^+ π^- channel would be the square of the single pion energy-loss efficiency,

$$\epsilon_{\frac{\mathrm{d}E}{\mathrm{d}x}} = \left(\frac{\int_A^B exp\left(-\frac{1}{2}\frac{x^2}{\sigma_\pi}\right)\mathrm{d}x}{\int exp\left(-\frac{1}{2}\frac{x^2}{\sigma_\pi}\right)\mathrm{d}x} \right)^2. \tag{4.2}$$

The statistical error on $\frac{\mathrm{d}^2N}{\mathrm{d}p_t\mathrm{d}y}$ is calculated by using equation 4.3,

$$\sigma_{stat} = \frac{\sqrt{S+BG}}{S}, \tag{4.3}$$

where S is the integral of the extracted resonance peak (not corrected for efficiency) within the extraction region and $BG+S$ is defined as the integral of the whole spectrum before the combinatorial background subtraction within the same extraction region.

Using this normalisation the spectra for the desired resonances can be constructed. However, it is first important to understand the systematic effects that can impact on the shape and size of these extracted spectra.

4.3 Systematic Uncertainties

The extracted values of the desired resonances can vary due to different systematic effects. This section details the different checks that were conducted in order to understand these effects and to assign stable systematic errors to the extracted results.

4.3.1 Sources of systematic errors

Different sources of systematic errors related to uncertainties arising from analysis cuts and raw yield extraction are discussed below.

4.3.1.1 Extracted peak shapes systematic study

The uncertainty for the assumptions made about the raw peak shape for the resonances extracted came from the uncertainties in the shape of the raw and corrected peaks. Both the phase space (equation 3.6) and the Söding (equation 3.4) correction terms are used as default, with the peaks corrected with an invariant mass dependent efficiency correction. Systematic checks were conducted with the removal of these corrections and the difference in spectra and mass values observed.

Figure 4.7 shows by how much the raw extracted yield changes when removing the phase space correction, by calculating the ratio of the spectrum obtained from removing the correction and the default spectrum. Figure 4.8 shows the same study applied to the extracted mass values of the ρ.

In figure 4.7 it is shown there is a systematic effect associated with the removal of the phase space correction, however, this is shown to have an effect of $\sim 5\%$ in the extracted yield at low p_t and less than 0.5% for the extracted mass value of the ρ.

A study was conducted as to the variation caused by using the invariant mass dependent acceptance efficiency (an example of which is shown in figure 3.3) as compared to using a single efficiency value (the values of which are shown in figure

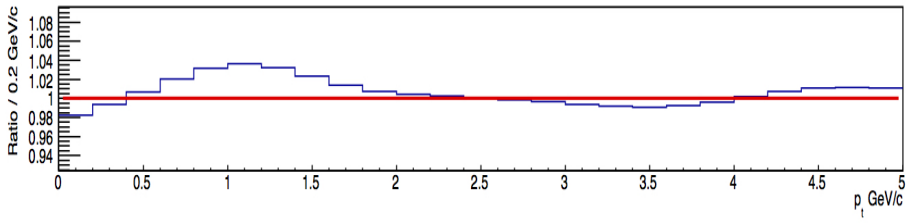

(a)

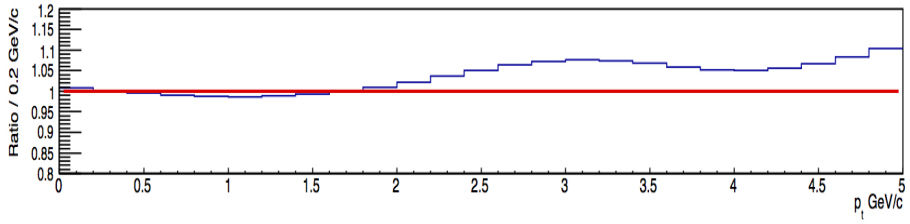

(b)

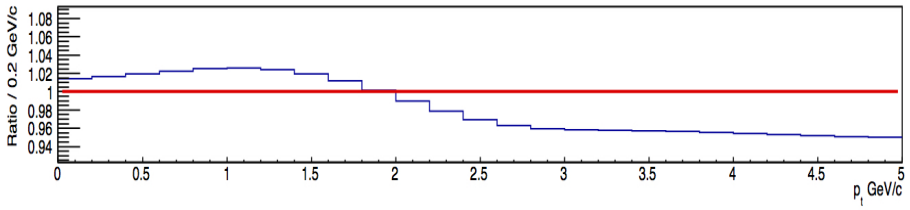

(c)

Figure 4.7: Ratio of p_t spectra obtained without phase space correction and default p_t spectrum for the (a) ρ, (b) f_0 and (c) f_2.

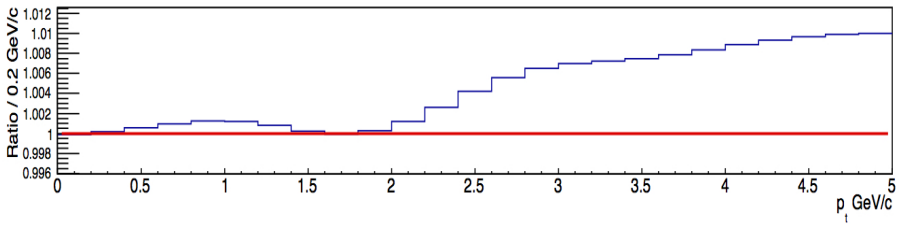

Figure 4.8: Ratio of ρ mass values obtained without phase space correction and default mass values.

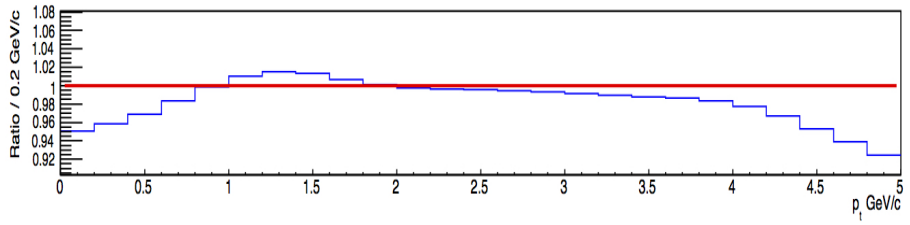

(a)

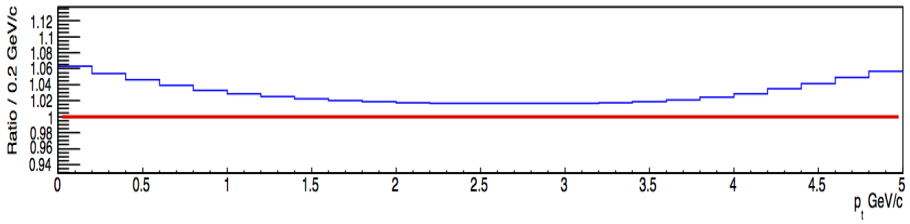

(b)

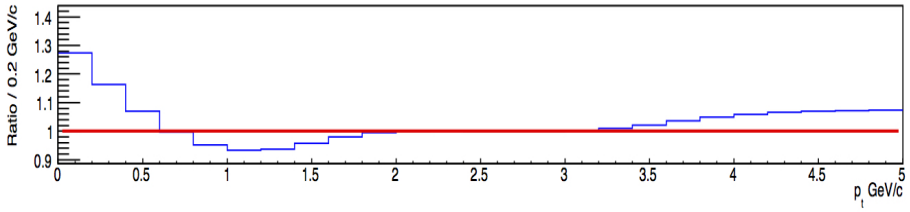

(c)

Figure 4.9: Ratio of p_t spectra obtained without invariant mass dependent efficiency correction and default p_t spectrum for the (a) ρ, (b) f_0 and (c) f_2.

3.2). The invariant mass dependent acceptance efficiency was used as default for this analysis. Figure 4.9 shows the ratio between the default p_t spectrum and the p_t spectrum extracted by using the single efficiency correction term for each p_t bin.

Much like the phase space correction term this correction affects the shape of the peaks but to a lesser degree, therefore these differences reach a maximum of $\sim 10\%$ for extracted yields and $\sim 0.5\%$ for the ρ mass value.

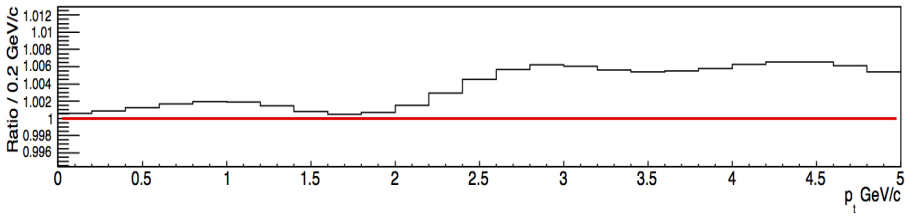

Figure 4.10: Ratio of ρ mass values obtained without invariant mass dependent efficiency correction and default mass values.

4.3.1.2 Spectrum fitting range systematic study

The default fitting range of the π^+ π^- spectrum was 0.28 GeV/c^2 to 1.8 GeV/c^2 to allow the f_2 to be fully fitted. The fitting range used in the analysis was limited to the cut off of the spectrum at low mass ($\sim$ 0.28 GeV/c^2 $\sim$ twice the mass of charged pion) and the upper edge of the studied region ending at 2.0 GeV/c^2.

Therefore a check was conducted whereby the resonance peaks were extracted with different fitting ranges, firstly by increasing the high mass fitting limit to the maximum of 2.0 GeV/c^2 and secondly by increasing the low mass fitting limit to 0.5 GeV/c^2 so as to see the effects of removing several of the spectrum components from the fitting range (i.e the K_s, η and η' (958) components).

Figures 4.11 and 4.12 show the effects of varying the fitting range of the π^+ π^- spectrum on the extracted resonance spectra and the extracted mass value respectively.

The difference caused by varying the fitting range seems to be dominated by the effects resulting from the increase in the low mass fitting limit. This is mostly due to the large effect this has on the constraint of the shape of the residual background, which, due to a high background to signal ratio at low p_t values causes a large effect

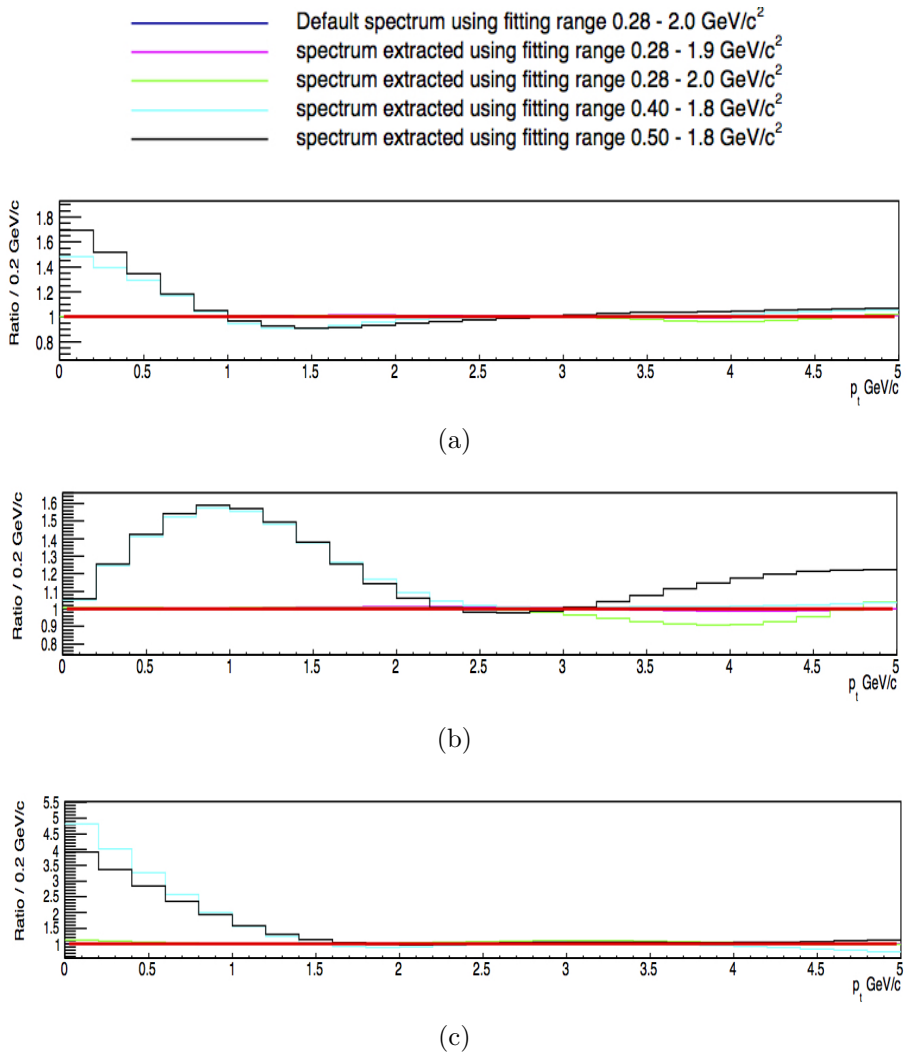

(a)

(b)

(c)

Figure 4.11: Ratio of p_t spectra obtained with different fitting ranges in the π^+ π^- p_t spectrum for the (a) ρ, (b) f_0 and (c) f_2.

of $\sim 100\%$ in the very low p_t regions.

The fitting ranges studied are compacted into a single systematic error by taking the average of the effects caused by varying the fitting range. In this way the large differences caused by increasing the low mass fitting limit due to unjustifiably removing the components in the low mass region of the spectrum is countered by the relativity small effect of increasing the high mass fitting limit.

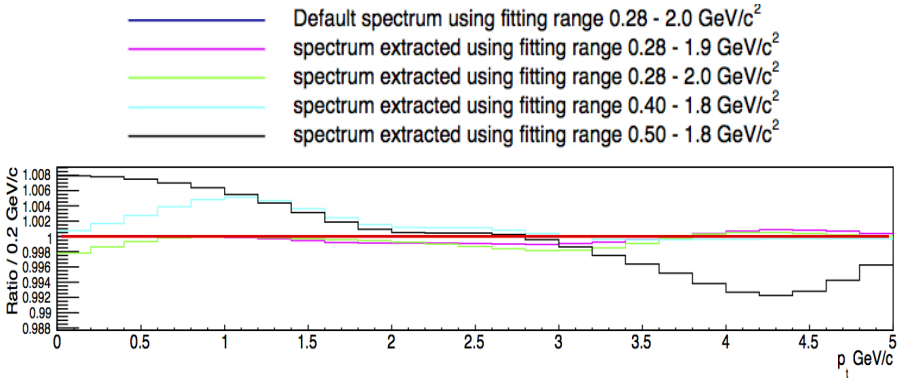

Figure 4.12: Ratio of ρ mass values obtained with different fitting ranges in the π^+ π^- p_t spectrum.

4.3.1.3 Template constructions systematic study

As discussed in section 3.4.1 the various templates used within the fitting process were constrained to evolve smoothly with p_t. This had the possibility of creating a bias due to an inaccurate estimation of these components' evolution as a function of p_t, thus the amount of contribution these templates had on the extracted resonance peaks was studied. These templates included the ω (782), η and η' (958) templates, the extra residual background templates discussed in section 3.2.4 and the K track misidentification background also discussed in section 3.2.4.

This results in a similar effect as seen with the fitting range, as the fitting process prioritises the fitting of an individual spectrum over allowing a smooth evolution of the components as a function of p_t. Figure 4.13 shows the effects of removing these constraints and was taken as a systematic uncertainty.

With less constraints on the K^* contamination, ω and η components, the shape of the residual background is less controlled. This allows the ρ peak to dominate in the low p_t regions resulting in a larger effect on the extracted f_2 yield and a relatively

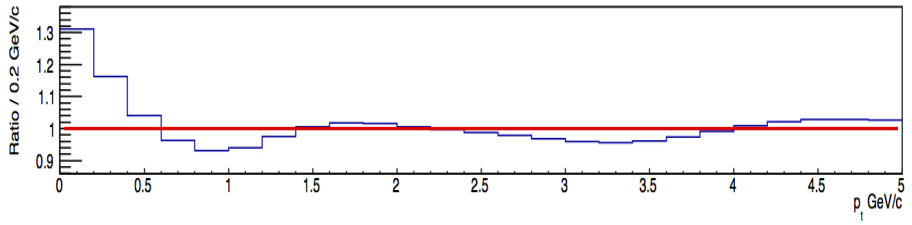

(a)

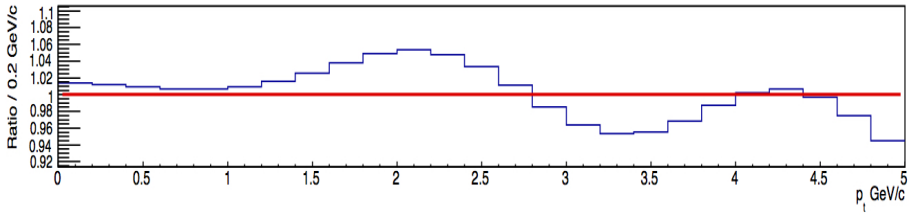

(b)

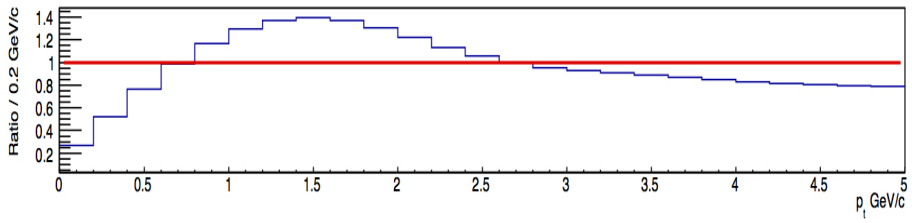

(c)

Figure 4.13: Ratio of p_t spectra obtained with no template constraints when fitting the π^+ π^- spectrum and the p_t spectra for the (a) ρ, (b) f_0 and (c) f_2 obtained with template constraints.

reduced effect on the extracted f_0 yield. This is due to the shape of the f_2 peak being more reliant on the shape of the ρ peak than the shape of the residual background.

In figure 4.14 it is shown that the mass values have a simple systematic effect due to the removal of the template constraints. This is due to the magnitude of the K^* contamination not having the necessary influence within the fitting to manipulate the central value of the ρ.

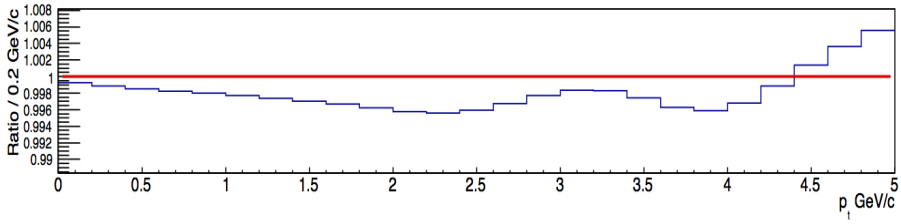

Figure 4.14: Ratio of ρ mass values obtained with no template constraints when fitting the π^+ π^- spectrum and mass values obtained with template constraints.

4.3.1.4 PID systematic study

Figures 4.15 and 4.16 show the effects of changing the TPC PID cut to both extremes ($n_\sigma = 1$ to the removal of the PID cut).

The TPC PID cut of n_σ was varied to see its effects on the extracted resonance peak. This had a large effect on all results, mostly due to the fact that all the components (MC templates, magnitudes and relative ratios) were affected by this cut. The average of the effect caused by the two extremes was taken as the systematic error for the cut.

4.3.1.5 Track cuts systematic study

The variations caused by the chosen track cuts, described in section 3.1.2, were estimated by varying these cuts by the amounts listed below. Any inaccuracies by the MC to simulate the detector efficiencies as well as the shapes of the various templates used in the analysis will be explored with this check. By varying these cuts the effect they have on the extracted spectra (figure 4.17) and extracted mass values (figure 4.18) can be estimated.

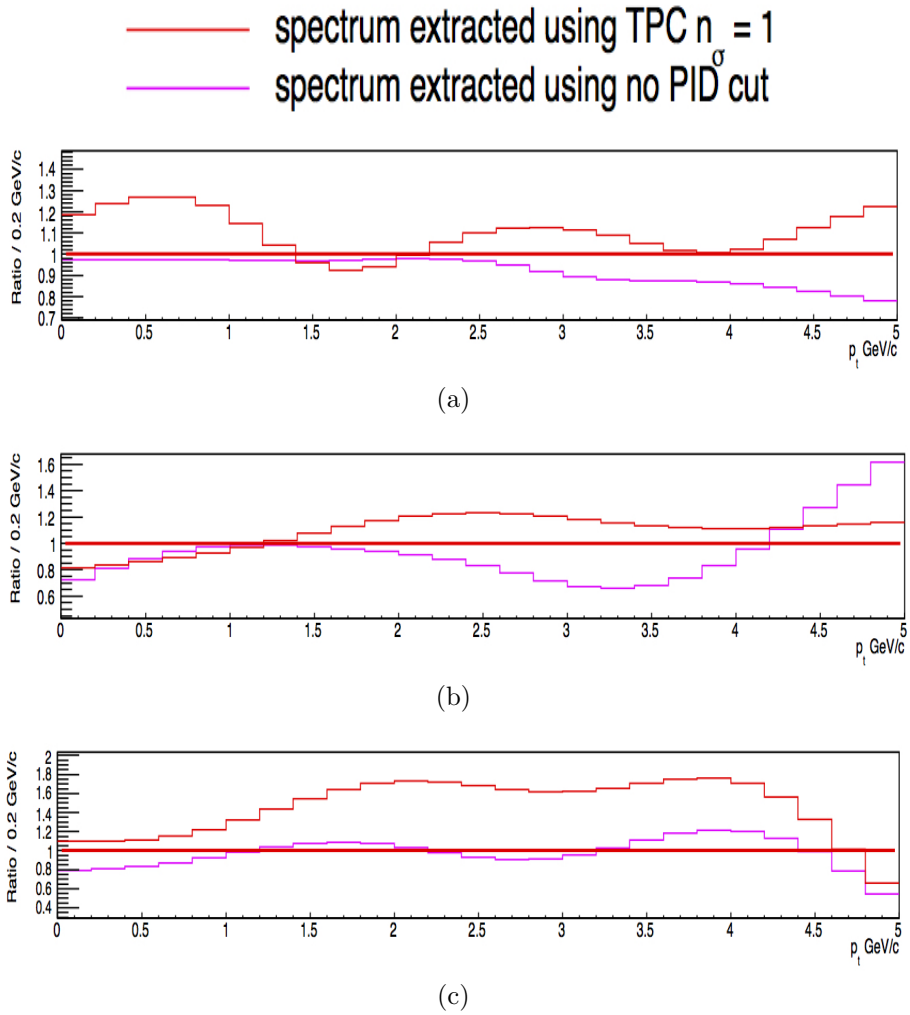

(a)

(b)

(c)

Figure 4.15: Ratio of p_t spectra obtained with varying the TPC PID n_σ cut from $n_\sigma = 1$ to the removal of the cut and p_t spectra obtained with default cut of $n_\sigma = 3$ for the (a) ρ, (b) f_0 and (c) f_2.

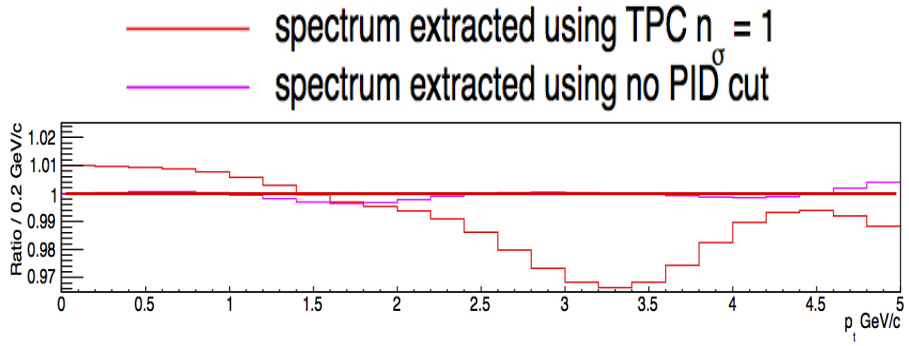

Figure 4.16: Ratio of ρ mass values obtained with varying the TPC PID n_σ cut from $n_\sigma = 1$ to the removal of the cut and the mass values obtained with default cut of $n_\sigma = 3$.

The track cuts variations studied were:

- DCA in the R direction is varied between a 6 and 8 σ cut in equation 3.1.
- DCA in the z direction is varied between 0.1 and 0.3 cm.
- The minimum track p_t is changed to 0.2 GeV/c from the default value of 0.15 GeV/c.
- The minimum TPC track χ^2 is increased to 6 from the default value of 4.
- The minimum number of clusters in the TPC is decreased to 50 from the default value of 70.

The dominating cuts appear to be the minimum track p_t and the DCA cuts, since both highly affect the relative magnitudes of the components used to control the fitting process. This results in higher systematic differences in the lower p_t regions due to high background to signal ratios and in high p_t regions due to lower overall statistics. The average of all of these effects were evaluated as the systematic error due to this effect.

4.3.1.6 Monte Carlo (MC) generator systematic study

Two different MC generators were used in this analysis. A systematic check was conducted to ensure that the choice of MC generator would not create a bias within this analysis.

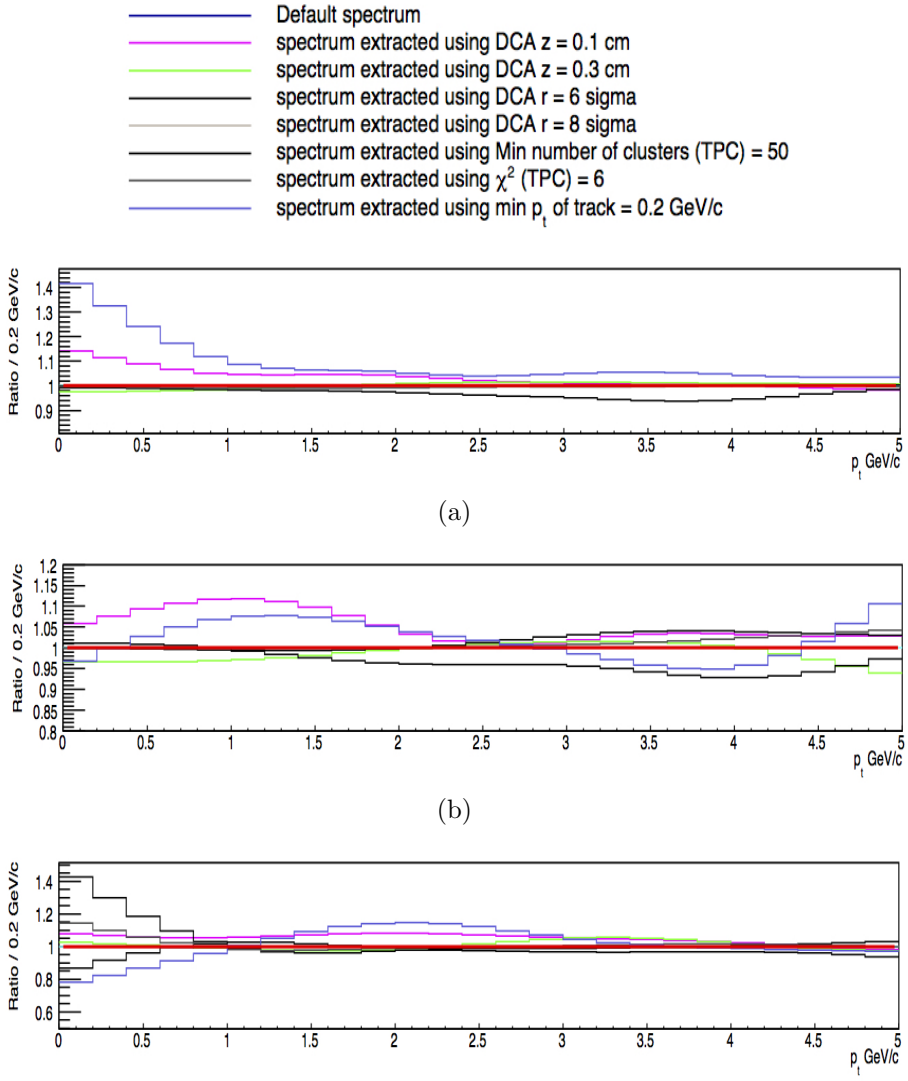

(a)

(b)

(c)

Figure 4.17: Ratio of p_t spectra obtained using varying track cuts and the p_t spectra for the (a) ρ, (b) f_0 and (c) f_2 obtained using default track cuts.

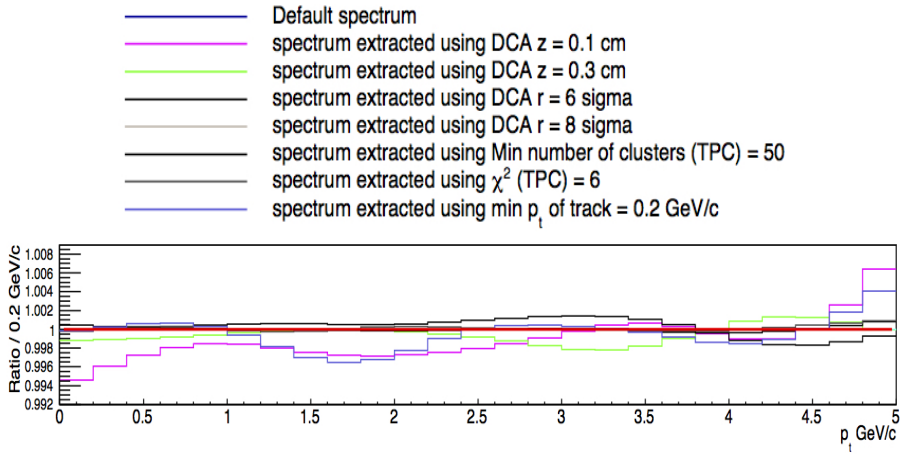

Figure 4.18: Ratio of ρ mass values obtained using varying track cuts and mass values obtained using default track cuts.

As figures 4.19 and 4.20 show, this is a systematic effect, since the efficiencies and MC templates shapes computed were reasonably consistent between the two MC generators.

4.3.1.7 Material budget

The uncertainty on the extracted yield due to the uncertainty of the material budget between the interaction point and the active region of the TPC was estimated from another analysis in proton - proton collisions [80]. This uncertainty was estimated to be $\sim 8\%$ within the study [80]. The average value was agreed upon due to the uncertainty from this effect being found to range from a maximum of 9% at the lower p_t values and a minimum of 3% above a p_t of $\sim 1\text{GeV}/c$ in [81]. The material budget was measured in [80] by the measurement of electron positron pairs in the TPC from photon conversions and comparing the measurement to expected MC estimations.

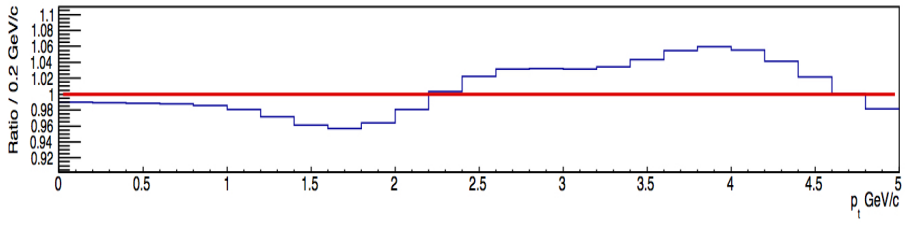

(a)

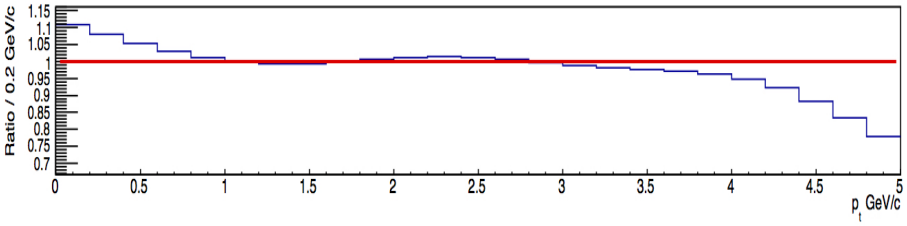

(b)

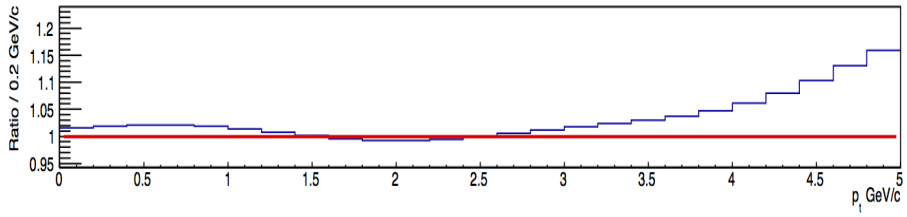

(c)

Figure 4.19: Ratio of p_t spectra obtained using Phojet MC and the p_t spectra for the (a) ρ, (b) f_0 and (c) f_2 obtained using Pythia MC.

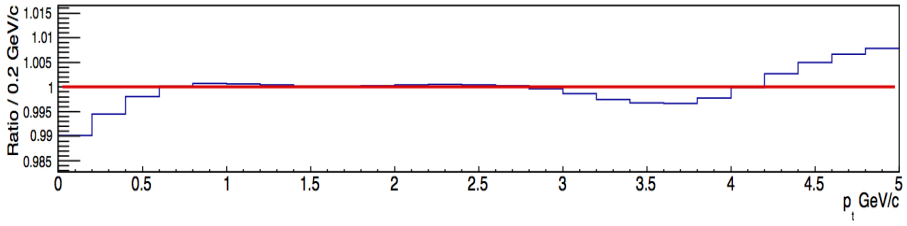

Figure 4.20: Ratio of ρ mass ρ values obtained using Phojet MC and mass values obtained Pythia MC.

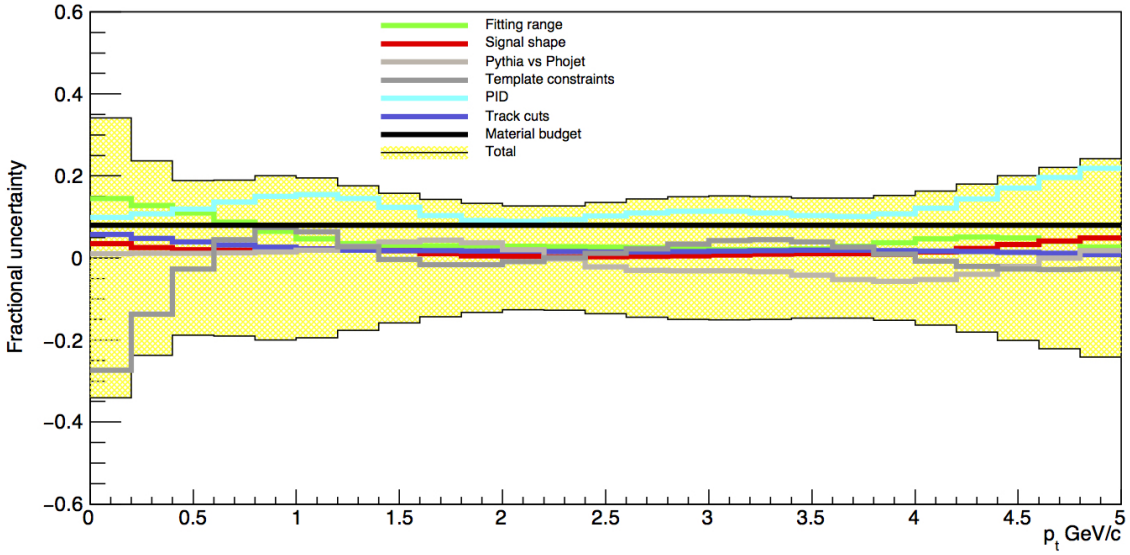

Figure 4.21: Total fractional systematic errors applied for ρ yield ($\mathrm{d}n/\mathrm{d}y$)

4.3.2 Total systematic errors applied

The systematic uncertainties listed above represent the main systematic effects on both the mass values of the ρ and the extraction of the desired resonance spectra. These error estimations were combined in a quadratic sum to produce the symmetrised total applied systematic error as shown in figures 4.21 and 4.22 for the ρ values and figures 4.23 and 4.24 for the f_0 and f_2 p_t spectra respectively.

4.4 Result - ρ mass

The mass values of the ρ extracted in each p_t bin are shown in figure 4.25. The mass value lies relatively close to the well known PDG value and is on average ~ 10 MeV/c^2 below this value.

However, since there is an absence of MC, this same measurement can not be made

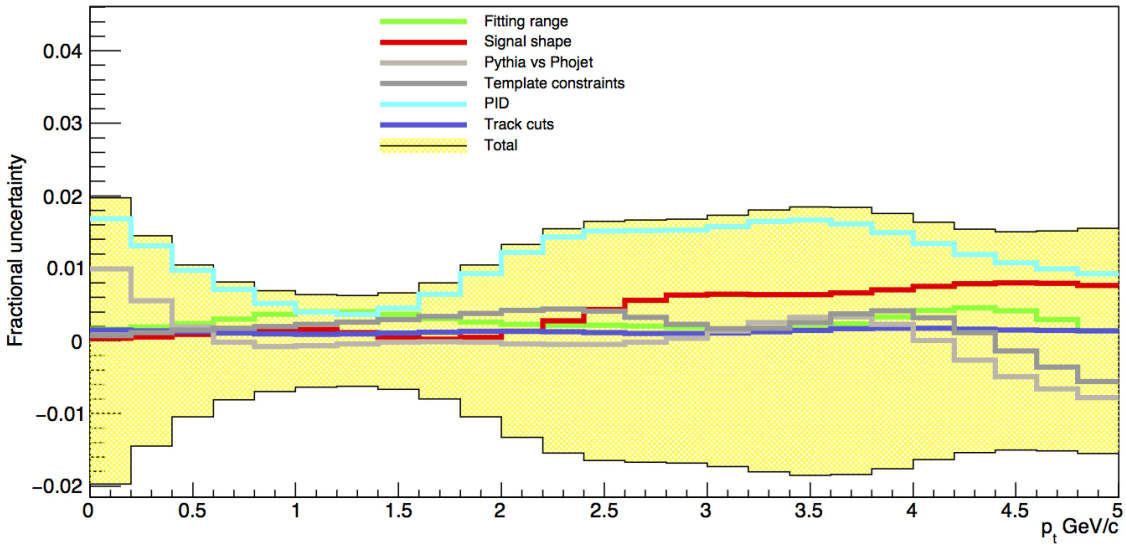

Figure 4.22: Total fractional systematic errors applied for ρ mass value as a function of p_t.

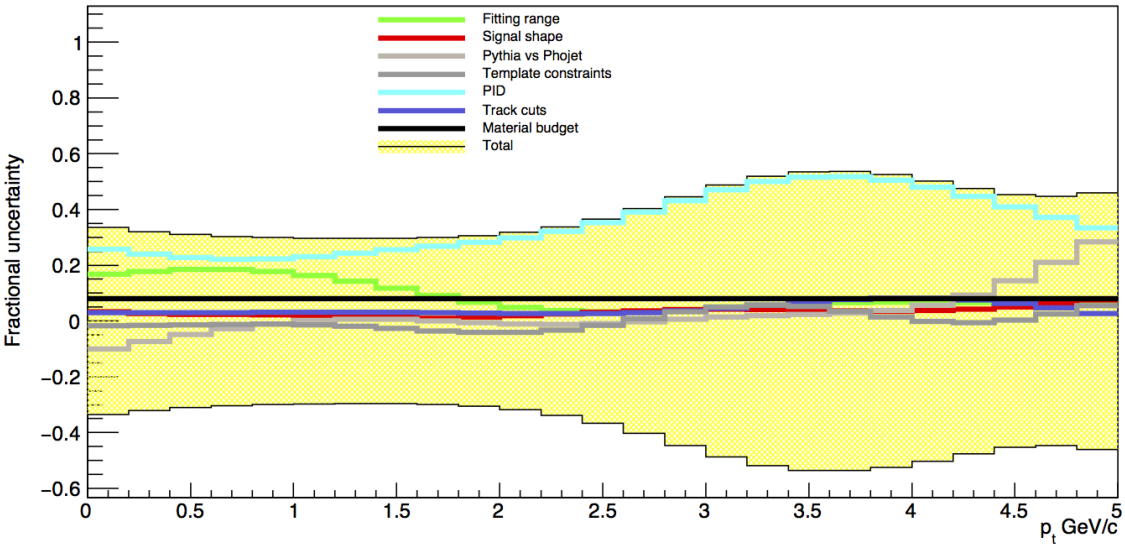

Figure 4.23: Total fractional systematic errors applied for f_0 yield ($\mathrm{d}n/\mathrm{d}y$).

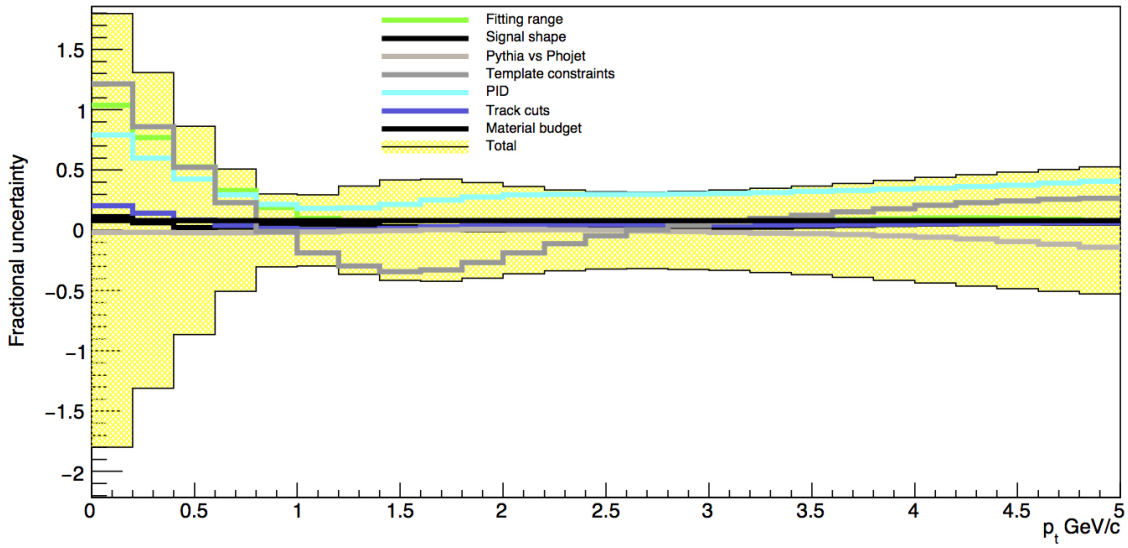

Figure 4.24: Total fractional systematic errors applied for f_2 yield (dn/dy).

for the f_0 and f_2 due to lack of knowledge of how these peaks would evolve as a function of p_t, much like how the width and efficiency of the ρ peak is dependent on p_t as shown in figure 3.17 and 3.2. Therefore to measure these values within this analysis the p_t integrated π^+ π^- spectrum seen in figure 3.11 is used. This has the advantage of using all of the statistics collected; however, it will not be possible to confirm any p_t dependence on these values. The measured mass values of all three of the resonance peaks are shown below, along with the measured width value of the $f_0(980)$ peak. The systematic uncertainties for these values were calculated by fitting the p_t integrated π^+ π^- spectrum created using the data obtained, with varying each parameter as described in section 4.3. The full tables of the variances on the extracted spectra fitting are shown in tables A.5, A.10 and A.16 for the measured mass values of the ρ, f_0 and f_2 respectively and table A.11 for the measured width value of the f_0.

- ρ mass (mean) $= 0.777 \pm 0.001(stat) \pm 0.069(syst)$ GeV/c^2

- f_0 mass (mean) = 0.969 $\pm 0.001(stat) \pm 0.02(syst)$ GeV/c^2
- f_0 width = 0.687 $\pm 0.003(stat) \pm 0.114(syst)$ GeV/c^2
- f_2 mass (mean) = 1.26 $\pm 0.01(stat) \pm 0.03(syst)$ GeV/c^2

This analysis measures the mass of the ρ to be close to the PDG. The mass and width f_0 measured values also lie within the known range seen in table 1.2. There is also opportunity in the future for even more accurate measurements of the f_0 properties with the proper addition of f_0 MC. The measured mass value of the f_2 is still ~ 10 MeV/c^2 lower than the PDG value in the p_t integrated measurement. This is likely due to a combination of low statistics and again the absence of f_2 MC; because of the large width of the f_2 it will experience distortion due to reconstruction, much like the ρ peak.

4.5 Result - Total $\mathrm{d}N/\mathrm{d}y$

4.5.1 Spectra Fittings

The extracted yields of the ρ, f_0 and f_2 are normalised via equation 4.1 in order to compare and contrast to analysis of other resonances within ALICE as well as other experiments.

These normalised spectra were then fitted via a Tsallis function (also known as Lévy function) [82] by default (shown in equation 4.4), which is shown along with

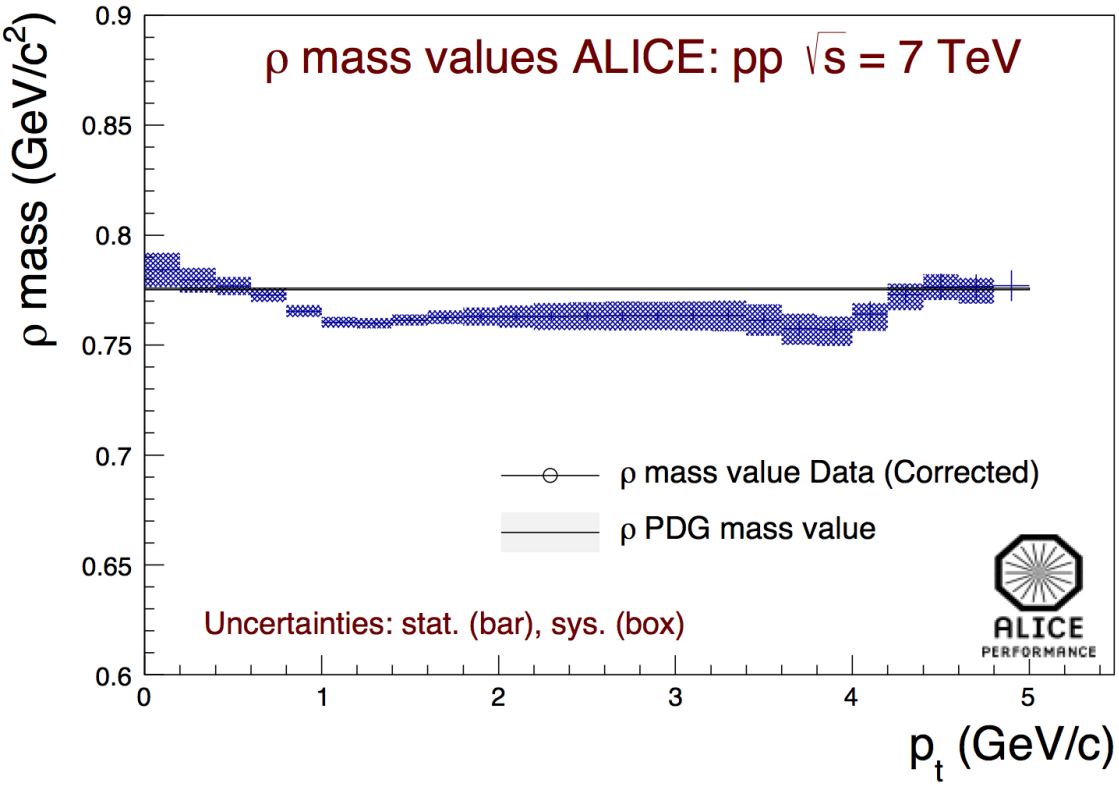

Figure 4.25: Mass values of the ρ resonance with systematic uncertainties.

the normalised spectrum for the ρ resonance in figure 4.26, the f_0 resonance in figure 4.27 and the f_2 resonance in figure 4.28,

$$\frac{d^2N}{dp_t dy} = \frac{p_t(n-1)(n-2)}{nT(nT+m(n-2))}\left(1+\frac{\sqrt{m^2+p_t^2}-m}{nT}\right)^{-n}, \tag{4.4}$$

where p_t is the transverse momentum (GeV/c), m is the mass of the particle in question (GeV/c^2) and n and T are the free fitting variables which are expressed in equations 4.5 and 4.6,

$$n = \frac{q}{q-1}, \tag{4.5}$$

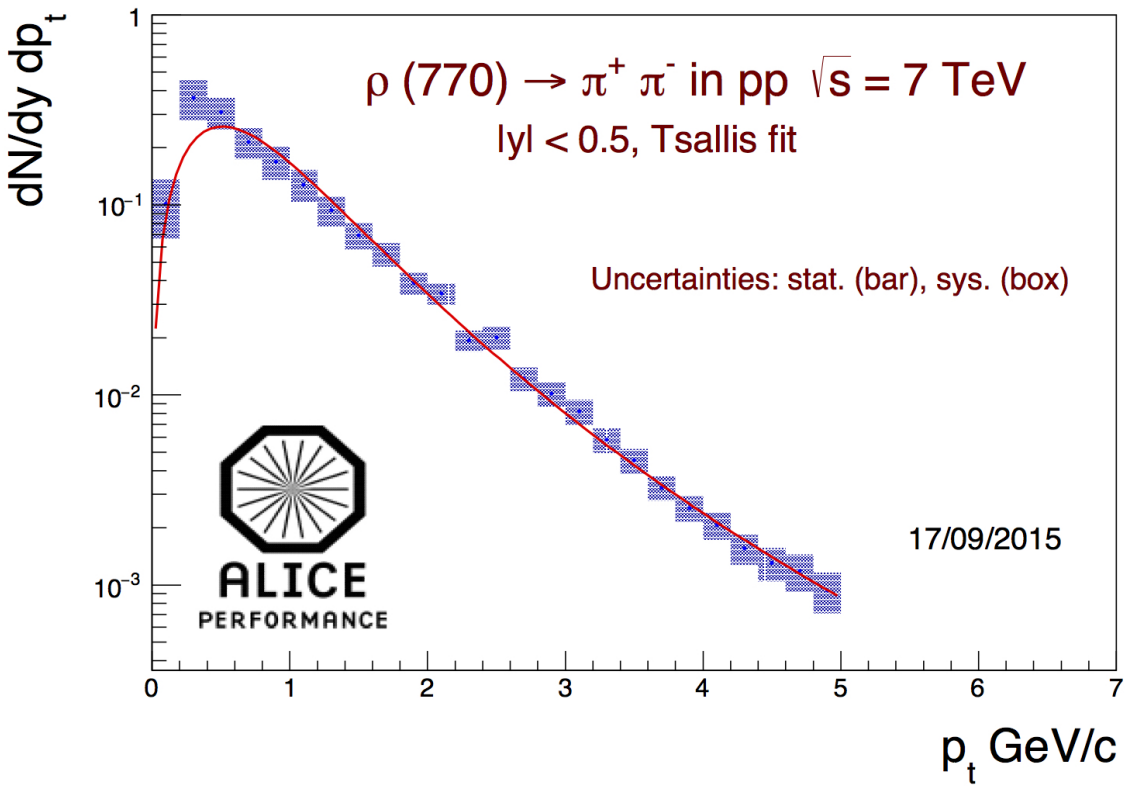

Figure 4.26: Author's own plot showing $\rho(770)$ spectrum with both systematic and statistical errors fitted via Tsallis fitting.

$$nT = \frac{T + m(q-1)}{q-1}, \tag{4.6}$$

which relate these parameters to m and q [83], where the parameter q is representative of the degree of the non-extensivity of the spectra (by how much the spectra follows non-extensive statistical mechanics as opposed to BoltzmannGibbs statistics).

The function is best used to describe such spectra within a large p_t range and can be derived using non-extensive thermodynamics. Non-extensive thermodynamics is defined based on the Tsallis entropy instead of the Boltzmann-Gibbs entropy [83].

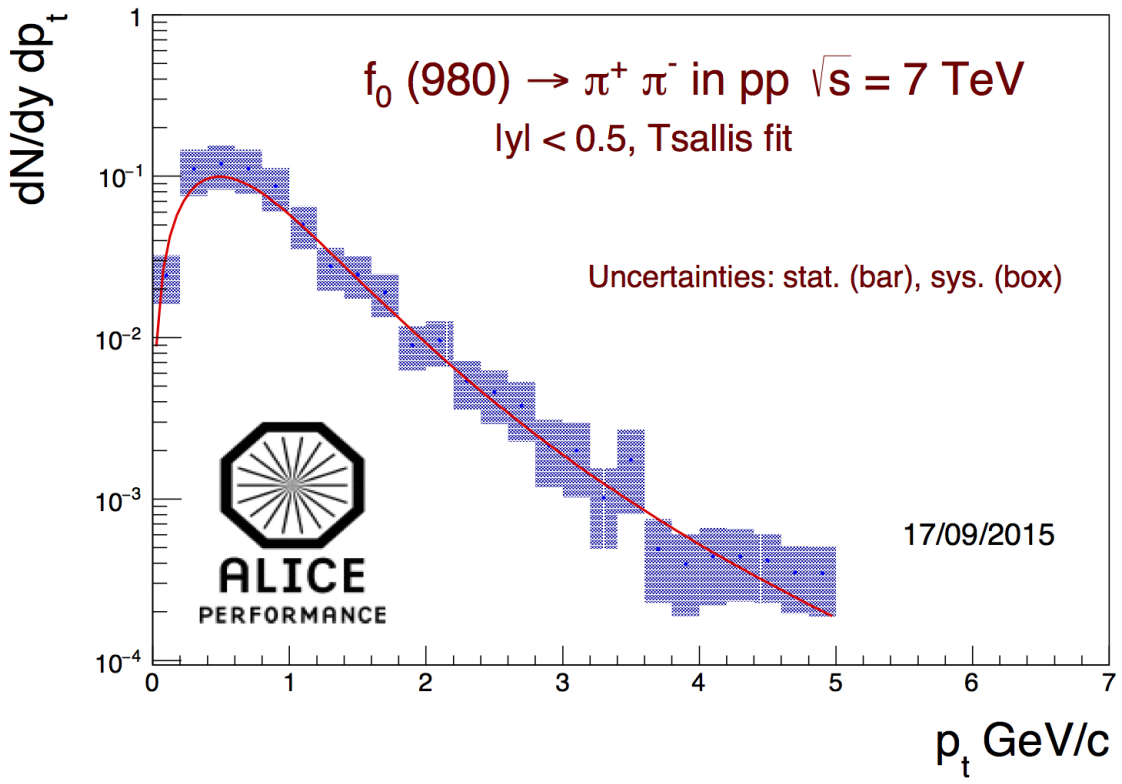

Figure 4.27: Author's own plot showing $f_0(980)$ spectrum with both systematic and statistical errors fitted via Tsallis fitting.

The parameters obtained from the fit are shown below with both statistical and systematic errors.

- ρ $n = 7.70 \pm 0.69(stat) \pm 1.59(syst)$
- ρ $T = 0.279 \pm 0.022(stat) \pm 0.059(syst)$ GeV/c
- f_0 $n = 6.33 \pm 0.69(stat) \pm 1.77(syst)$
- f_0 $T = 0.195 \pm 0.021(stat) \pm 0.064(syst)$ GeV/c
- f_2 $n = 12.98 \pm 0.69(stat) \pm 7.15(syst)$
- f_2 $T = 0.492 \pm 0.021(stat) \pm 0.241(syst)$ GeV/c

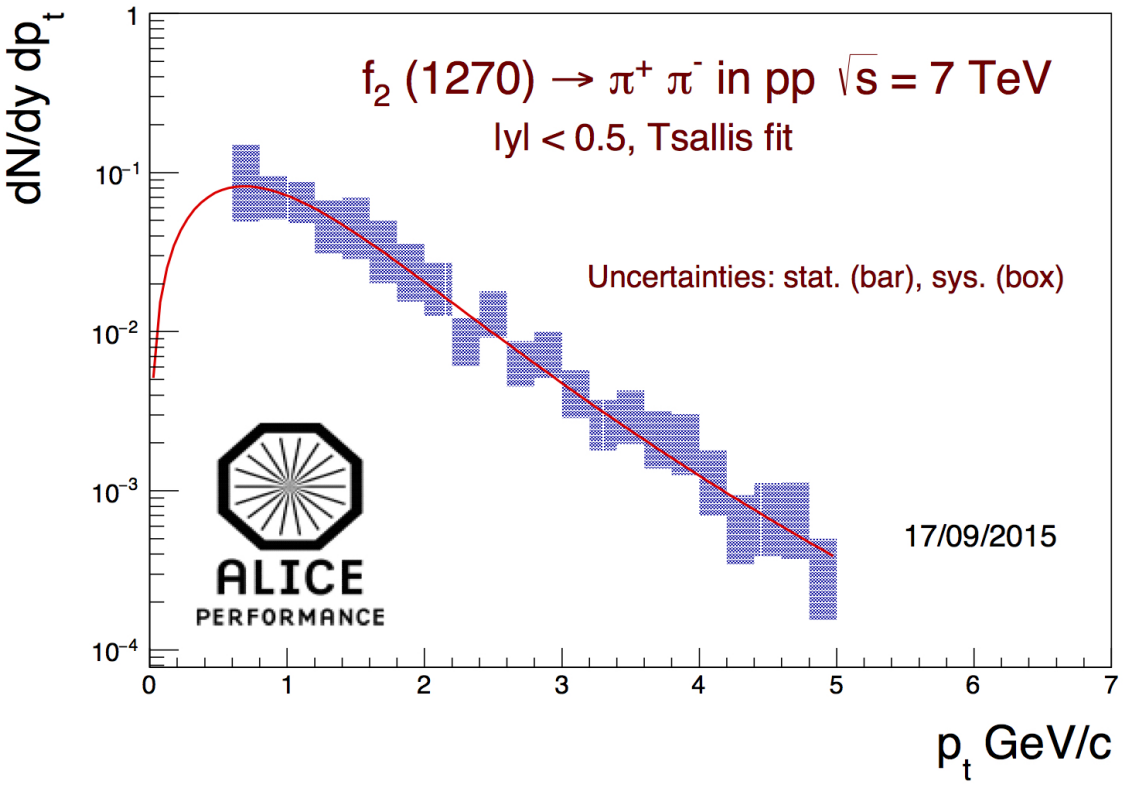

Figure 4.28: Author's own plot showing $f_2(1270)$ spectrum with both systematic and statistical errors fitted via Tsallis fitting.

The systematic errors for these values were calculated by fitting the spectra, produced using the data obtained, and varying each parameter as described in section 4.3. The full tables of the variances on the extracted spectra fitting are shown in tables A.3 and A.4 for the ρ T and n values respectively, tables A.8 and A.9 for the f_0 T and n values respectively and A.14 and A.15 for the f_2 T and n values respectively.

The measured value of $\mathrm{d}n/\mathrm{d}y$ is defined as the full integral over p_t of the Tsallis function $\frac{\mathrm{d}^2N}{\mathrm{d}p_t\mathrm{d}y}$. This is done by summing up the three integrated segments of the spectrum, the measured region integrated by bin counting the data points and the segments either side of the measured region, which are integrated by using the Tsallis function that is fitted to the data points.

The measured values for $\mathrm{d}n/\mathrm{d}y$ with statistical and systematic errors are listed below.

- ρ $\mathrm{d}n/\mathrm{d}y = 0.337 \pm 0.003(stat) \pm 0.042(syst)$
- f_0 $\mathrm{d}n/\mathrm{d}y = 0.124 \pm 0.001(stat) \pm 0.020(syst)$
- f_2 $\mathrm{d}n/\mathrm{d}y = 0.150 \pm 0.001(stat) \pm 0.035(syst)$

The estimation of the systematic errors employed a similar strategy as the n and T parameter results, the full tables of which are shown in tables A.1, A.6 and A.12 for the ρ f_0 and f_2 values respectively.

4.6 Result - $\langle p_t \rangle$

The mean transverse momentum $\langle p_t \rangle$ was calculated from the ρ p_t distribution via equation 4.7,

$$\langle p_t \rangle = \frac{\int p_t f(p_t) \mathrm{d}p_t}{\int f(p_t) \mathrm{d}p_t} \tag{4.7}$$

where $f_{(p_t)}$ is the function used to fit the given spectrum and p_t is the transverse momentum.

The calculated $\langle p_t \rangle$ values are listed below, and include the statistical and systematic errors assigned to each measurement.

- ρ $\langle p_t \rangle = 0.876 \pm 0.003(stat) \pm 0.072(syst)$ GeV/c
- f_0 $\langle p_t \rangle = 0.895 \pm 0.001(stat) \pm 0.089(syst)$ GeV/c
- f_2 $\langle p_t \rangle = 1.25 \pm 0.01(stat) \pm 0.157(syst)$ GeV/c

The systematic error for these values were calculated using the values of the results obtained with each of the changed parameters as described in section 4.3. The calculated $\langle p_t \rangle$ values of the extracted resonance results are compared to other measured resonances as shown in figure 4.29. The full tables of the systematic error estimates are shown in tables A.2, A.7 and A.13 for the ρ, f_0 and f_2 $\langle p_t \rangle$ errors respectively.

Figure 4.29 shows the dependence the $\langle p_t \rangle$ value of a given resonance has on the

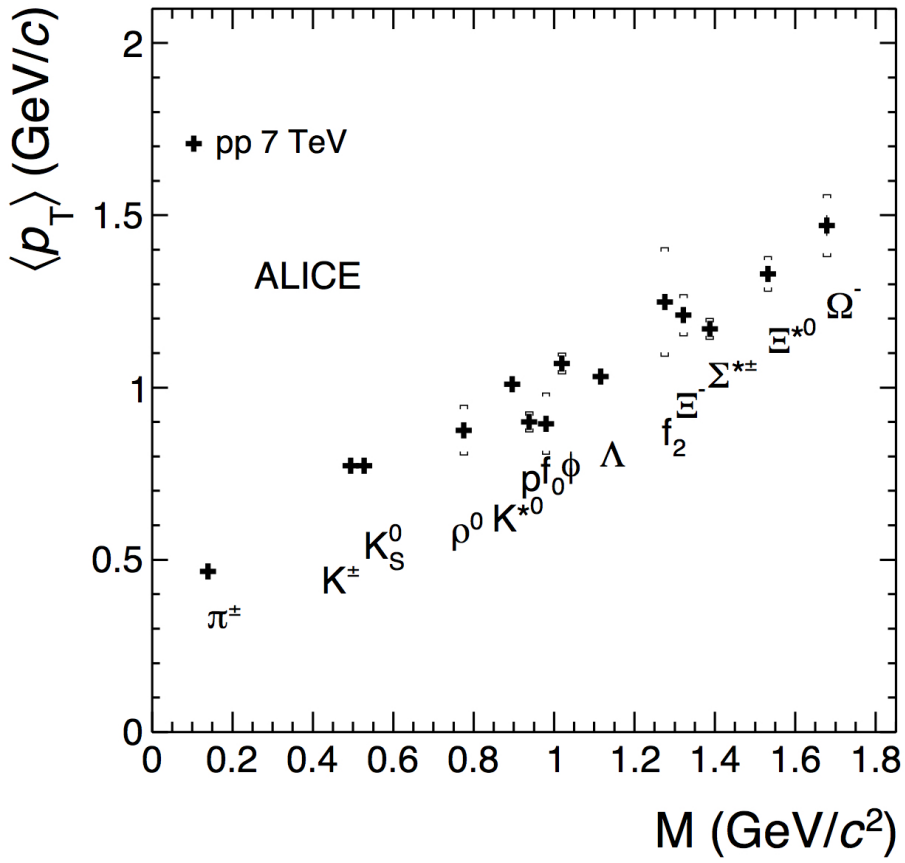

Figure 4.29: Mean p_t value extracted compared to values of extracted resonances from ALICE [50] including author's own ρ, f_0 and f_2 points extracted from this analysis.

Table 4.2: Normalised yields of π^+ and π^- from analysis in [2]

Particle	Normalised yield ($\frac{d^2N}{dp_t dy}$)
π^+	2.22 ± 0.125 (syst) ± 0.072 (stat)
π^-	2.22 ± 0.125 (syst) ± 0.071 (stat)

mass value. The pattern shown in figure 4.29 can be interpreted as the combined effects of different production methods, either from recombination (where lower momentum partons combine to form higher momentum heavier hadrons) or from fragmentation (where higher momentum partons fragment to form lower momentum lighter hadrons). Figure 4.29 also shows how the added points from this analysis continue the observed pattern of the $\langle p_t \rangle$ as a function of resonance mass.

4.7 Result - Extracted resonance / π ratio

The normalised yields for the pion spectra are listed in table 4.2. The measurement of a resonance yield compared to a stable particle yield is useful when comparing the yield result to other experiments and also different energy and collision sets within the same experiment, as changes caused by different collision energies and densities are mostly countered and normalised by the stable particle measurement.

The measured values of the desired resonances over the pion yield ratio.

- $\rho/\pi = 0.151 \pm 0.004(stat) \pm 0.019(syst)$
- $f_0/\pi = 0.0557 \pm 0.0001(stat) \pm 0.009(syst)$
- $f_2/\pi = 0.0429 \pm 0.0001(stat) \pm 0.013(syst)$

The overall suppression of these resonances, as compared to the stable π particle is partly explained by the fact that π mesons are created both directly and via the decays of short lived resonances within the event. They are also amongst the lightest mesons and thus created in greater quantities.

The measurements of the ρ/π and f_0/π ratio at ALICE are shown in figure 4.30, which most notably highlights the proton - proton collision results for the ρ in a different analysis at 2.76 TeV and the author's own analysis at 7 TeV collision sets and f_0 in 7 TeV.

The result of ~ 0.13 for the ρ/π ratio obtained from the 2.76 TeV and 7 TeV analyses are thus consistent with previous measurements. Before the addition of the ALICE points to figure 4.30 it was not clear if the ρ/π ratio was increasing or would flatten out. The ALICE points at energies 2.76 TeV and this analysis' point at 7 TeV shows this ratio levelling out at ~ 0.13.

Additionally with the added ALICE point, figure 4.30 shows a continuous dependence of the f_0/π ratio with energy.

The evolution of this ratio as a function of p_t is shown in figures 4.31a and 4.31b; these show the ratio of the given extracted resonance normalised yield over the normalised yield of the π as a function of p_t. The trend of the ratios as a function of p_t highlights that heavier particle production is increased as more phase space is made available at higher values of p_t.

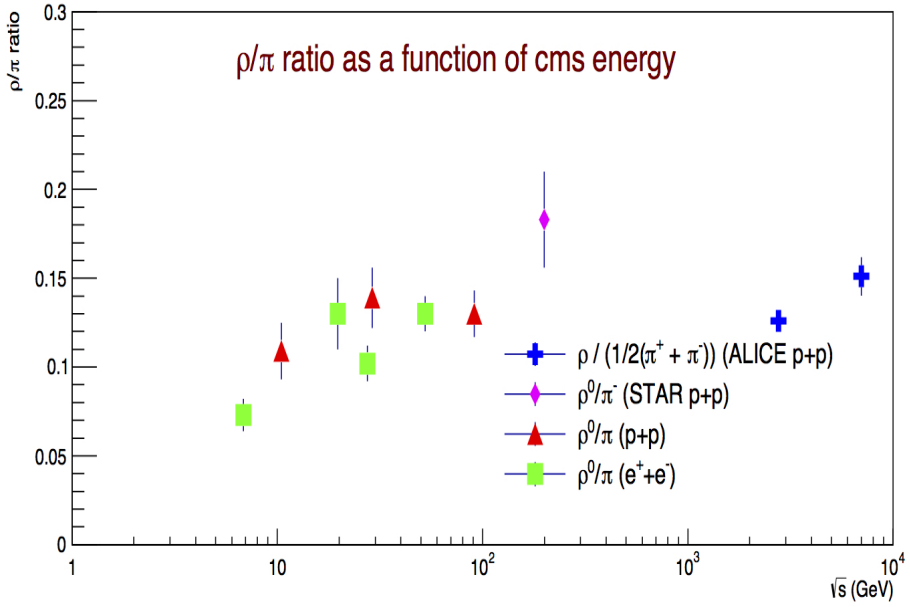

(a)

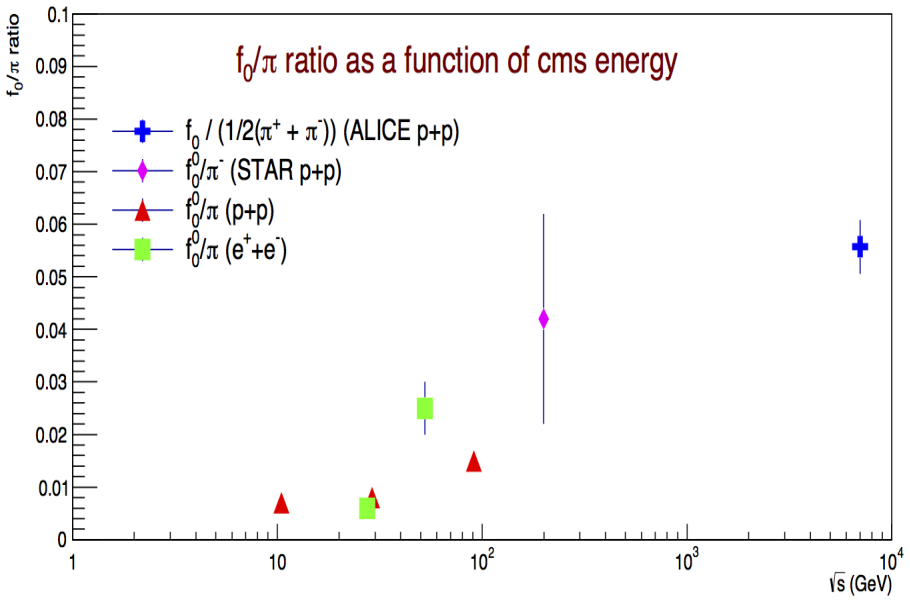

(b)

Figure 4.30: Ratio of the (a) $\rho(770)$ and (b) $f_0(980)$ resonances to charged pion ratio as a function of beam energy. Data points are taken from STAR at 200 GeV [32], e^+e^- collisions at 91 GeV [84], 29 GeV [85] and 10.45 GeV [86] as well as proton - proton collisions at 52.5 GeV [34], 27.5 GeV [87], 19.7 GeV [88], 6.84 GeV [89], 2.76 TeV ALICE analysis and author's own 7 TeV analysis.

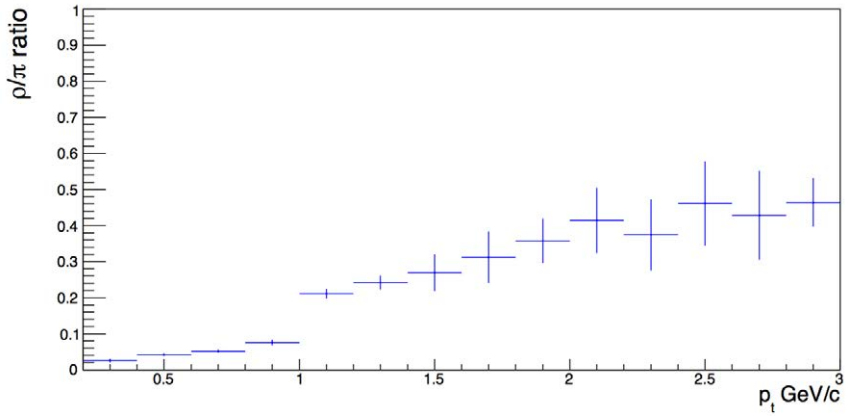

(a)

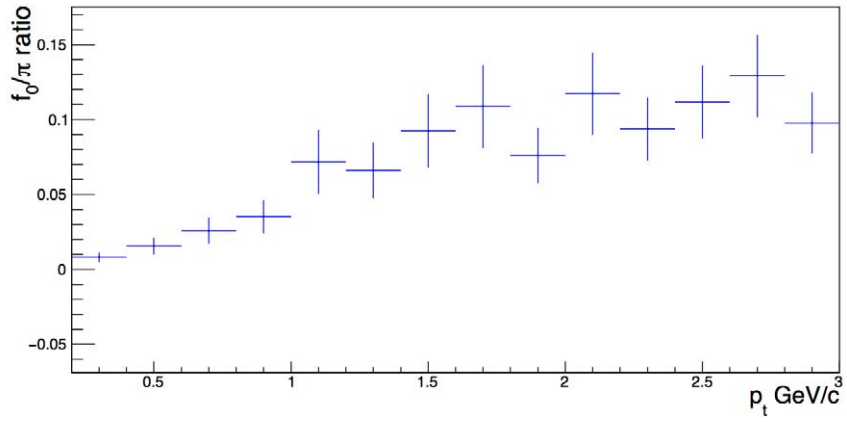

(b)

Figure 4.31: Ratio of the (a)$\rho(770)$ and (b) $f_0(980)$ resonances to charged pion yields as a function of p_t extracted from author's own analysis.

CHAPTER 5

Summary and Conclusions

The analysis has obtained preliminary results on the extraction of the $\rho(770)$, $f_0(980)$ and $f_2(1270)$ at mid-rapidity in proton - proton collisions at 7 TeV. The masses of all three extracted resonances are fairly consistent with previously catalogued measurements seen in [1], arguably due to the inclusion of raw resonance peak corrections being applied to the extraction process thus accounting for the deformities from a pure relativistic Breit-Wigner shape (equation 3.2). These corrections include a residual momentum dependence of the widths of the peaks (equation 3.3) and the inclusion of a interference term resulting from Bose-Einstein correlations (3.4) applied to the ρ peak, which has a very notable effect at low p_t values as seen in the

STAR analysis.

This analysis, therefore, shows very minimal dependence on the mass values extracted as a function of p_t with minimal noticeable shifts from the established values. The importance of this is that this analysis can serve as a control for future ρ heavy ion analysis within ALICE. This will allow any centrality dependence of the mass value to be observed in comparison to the non heavy-ion environment. This will be further aided by the addition of an analysis within proton - heavy ion collisions to further act as a control for the non heavy ion analysis.

This analysis also measured the mass and width values of the f_0 peak to a degree that appears to have the potential in matching the accuracy of the ρ analysis.

The results obtained from the extracted spectra for these resonances also contain useful information relating to the environment of the proton - proton collisions and if they agree with previously established experiments and models. All three spectra fit well with the Tsallis function used in most non heavy-ion spectra constructions and from these fittings the pure fitting parameters T and n are extracted.

The extracted $\langle p_t \rangle$ results for these resonances also agree with the trend seen in the obtained $\langle p_t \rangle$ values for other studies resonances at ALICE.

This analysis requires the additional input of MC simulation (ALICE official or otherwise) to better establish estimations of the f_0 and f_2 efficiencies, as well as to estimate how the mass and width values evolve through p_t. To do so would allow these values to be better controlled within the fitting process and to possibly allow

more precise measurements of the mass and width value of the f_0 and f_2 peaks.

This analysis also presents the first look at the spectrum of the f_2 in proton - proton collisions at 7 TeV in the $\pi^+ \pi^-$ channel; as it is much harder to extract this component, the results presented within this analysis have larger systematic errors compared to the ρ extraction. The extraction of this peak would be aided by an additional fitting of the $\pi^+ \pi^-$ spectrum, separately from the other two desired peaks with wider p_t bins studied. This would allow more statistics to be made available, as well as to fully control the parameters of the ρ and f_0 components from previously conducted fitting with the smaller p_t regions.

This analysis made use of a method to estimate the residual background of the π^+ π^- spectrum, which encountered a number of short comings. However this method was only required to fit the low p_t bins and as such the analysis can still be supported by the removal of these low p_t bins.

Using the ρ/π and f_0/π ratios assists with the understanding of the spectra evolution as a function of collision centre-of-mass energy for these two resonances. The ρ/π ratio appears to be stable with the addition of the recent ALICE points and the f_0/π ratio appears to be increasing with energy.

REFERENCES

[1] K. Olive *et al.*, "Review of particle physics," *Chinese Physics C*, vol. 38, no. 9, p. 090001, 2014.

[2] J. Adam *et al.*, "Measurement of pion, kaon and proton production in protonproton collisions at $\sqrt{s} = 7$ TeV," *Eur. Phys. J.*, vol. C75, no. 5, p. 226, 2015.

[3] K. Krane, *Introductory Nuclear Physics*. Wiley, 1987.

[4] X. Qian and P. Vogel, "Neutrino Mass Hierarchy," *Prog. Part. Nucl. Phys.*, vol. 83, pp. 1–30, 2015.

[5] R. Cahn and G. Goldhaber, *The Experimental Foundations of Particle Physics*. Cambridge books online, Cambridge University Press, 2009.

[6] H. Fritzsch, "Quantum Flavor Dynamics," *Conf. Proc.*, vol. C770117, pp. 275–322, 1977.

[7] J. Gribbin, *Q is for Quantum: An Encyclopedia of Particle Physics*. Touchstone, 2000.

[8] H. Arodz, J. Dziarmaga, and W. Zurek, *Patterns of Symmetry Breaking*. NATO science series: Mathematics, physics, and chemistry, Springer, 2003.

[9] S. Chatrchyan *et al.*, "Observation of a new boson at a mass of 125 GeV with the CMS experiment at the LHC," *Phys.Lett.*, vol. B716, pp. 30–61, 2012.

[10] G. Aad *et al.*, "Observation of a new particle in the search for the Standard Model Higgs boson with the ATLAS detector at the LHC," *Phys.Lett.*, vol. B716, pp. 1–29, 2012.

[11] CERN, "LHC experiments join forces to zoom in on the Higgs boson." `http://press.web.cern.ch/press-releases/2015/03/lhc-experiments-join-forces-zoom-higgs-boson`.

[12] R. Aaij *et al.*, "Observation of the resonant character of the $Z(4430)^-$ state," *Phys.Rev.Lett.*, vol. 112, p. 222002, 2014.

[13] R. Aaij *et al.*, "Observation of J/ψp Resonances Consistent with Pentaquark States in Λ_b^0 to J/ψ K^-p Decays," *Phys. Rev. Lett.*, vol. 115, p. 072001, 2015.

[14] H. S. Chung, J. Lee, and D. Kang, "Cornell Potential Parameters for S-wave Heavy Quarkonia," *J.Korean Phys.Soc.*, vol. 52, pp. 1151–1154, 2008.

[15] A. V. Radyushkin, "Optimized Λ - Parametrization for the QCD Running Coupling Constant in Space - Like and Time - Like Regions," *JINR Rapid Commun.*, vol. 78, pp. 96–99, 1996.

[16] Z. Fodor and S. Katz, "Critical point of QCD at finite T and mu, lattice results for physical quark masses," *JHEP*, vol. 0404, p. 050, 2004.

[17] A. Chodos, R. L. Jaffe, K. Johnson, C. B. Thorn, and V. F. Weisskopf, "New extended model of hadrons," *Phys. Rev. D*, vol. 9, pp. 3471–3495, 1974.

[18] A. R. Erwin, R. March, W. D. Walker, and E. West, "Evidence for a π - π resonance in the i=1, j=1 state," *Phys. Rev. Lett.*, vol. 6, pp. 628–630, Jun 1961.

[19] C. McNeile and C. Michael, "Properties of light scalar mesons from lattice QCD," *Phys.Rev.*, vol. D74, p. 014508, 2006.

[20] N. A. Törnqvist and M. Roos, "Confirmation of the σ meson," *Phys. Rev. Lett.*, vol. 76, pp. 1575–1578, Mar 1996.

[21] I. Bediaga, F. S. Navarra, and M. Nielsen, "The Structure of $f_0(980)$ from charmed mesons decays," *Phys. Lett.*, vol. B579, pp. 59–66, 2004.

[22] R. L. Jaffe, "Multi-Quark Hadrons. 1. The Phenomenology of (2 Quark 2 anti-Quark) Mesons," *Phys. Rev.*, vol. D15, p. 267, 1977.

[23] R. L. Jaffe, "Multi-Quark Hadrons. 2. Methods," *Phys. Rev.*, vol. D15, p. 281, 1977.

[24] J. D. Weinstein and N. Isgur, "K anti-K Molecules," *Phys.Rev.*, vol. D41, p. 2236, 1990.

[25] J. D. Weinstein and N. Isgur, "Do Multi-Quark Hadrons Exist?," *Phys. Rev. Lett.*, vol. 48, p. 659, 1982.

[26] J. D. Weinstein and N. Isgur, "The q q anti-q anti-q System in a Potential Model," *Phys. Rev.*, vol. D27, p. 588, 1983.

[27] T. Sekihara and S. Kumano, "Constraint on $K\bar{K}$ compositeness of the $a_0(980)$ and $f_0(980)$ resonances from their mixing intensity," *Phys. Rev.*, vol. D92, no. 3, p. 034010, 2015.

[28] L. Geng and E. Oset, "Vector meson-vector meson interaction in a hidden gauge unitary approach," *Phys.Rev.*, vol. D79, p. 074009, 2009.

[29] R. Molina, H. Nagahiro, A. Hosaka, and E. Oset, "Scalar, axial-vector and tensor resonances from the ρD*, ωD* interaction in the hidden gauge formalism," *Phys.Rev.*, vol. D80, p. 014025, 2009.

[30] R. Molina, D. Nicmorus, and E. Oset, "The ρ ρ interaction in the hidden gauge formalism and the $f_0(1370)$ and $f_2(1270)$ resonances," *Phys. Rev. D*, vol. 78, p. 114018, Dec 2008.

[31] S. Damjanovic, "First measurement of the rho spectral function in nuclear collisions," *Eur. Phys. J.*, vol. C49, pp. 235–241, 2007.

[32] J. Adams *et al.*, "ρ Production and Possible Modification in Au + Au and p+p Collisions," *Phys. Rev. Lett.*, vol. 92, p. 092301, 2004.

[33] P. Fachini, "$\rho^0(770)$ and $f_0(980)$ production in Au+Au and pp collisions at $\sqrt{s_{NN}} = 200$ GeV," *J.Phys.*, vol. G30, pp. S565–S570, 2004.

[34] D. Drijard *et al.*, "Production of vector and tensor mesons in proton proton collisions at $\sqrt{s_{nn}} = 52.5$ GeV," *Z.Phys.*, vol. C9, p. 293, 1981.

[35] D. Adamova *et al.*, "Enhanced production of low mass electron pairs in 40-AGeV Pb - Au collisions at the CERN SPS," *Phys. Rev. Lett.*, vol. 91, p. 042301, 2003.

[36] "ALICE Collaboration home page." `http://aliweb.cern.ch/`.

[37] M. A. Stephanov, "QCD phase diagram: An Overview," *PoS*, vol. LAT2006, p. 024, 2006.

[38] S. Ejiri, F. Karsch, and K. Redlich, "Hadronic fluctuations at the QCD phase transition," *Phys.Lett.*, vol. B633, pp. 275–282, 2006.

[39] J. M. Lattimer, "The nuclear equation of state and neutron star masses," *Ann.Rev.Nucl.Part.Sci.*, vol. 62, pp. 485–515, 2012.

[40] A. Watson, *The Quantum Quark*. Cambridge University Press, 2004.

[41] R. D. Pisarski, "Phenomenology of the Chiral Phase Transition," *Phys. Lett.*, vol. B110, p. 155, 1982.

[42] "RHIC home page." `https://www.bnl.gov/rhic/`.

[43] CERN, "LHC home page." `http://home.web.cern.ch/topics/large-hadron-collider/`.

[44] CERN, "LHC Layout." `http://www.lhc-closer.es/img/subidas/3_4_1_1.jpg`, 2011.

[45] M. Barnes, L. Ducimetiere, T. Fowler, V. Senaj, and L. Sermeus, "Injection and extraction magnets: Kicker magnets," 2011.

[46] "TOTEM home page." `http://home.web.cern.ch/about/experiments/totem`.

[47] "LHCf home page." `http://hep.fi.infn.it/LHCf`.

[48] "ALFA home page." `http://atlas-project-lumi-fphys.web.cern.ch/atlas-project-lumi-fphys/ALFA`.

[49] CERN, "LHC schematic." `http://www.maalpu.org/lhc/LHC.chain.png`, 2011.

[50] ALICE, "Figure repository." `http://aliceinfo.cern.ch/Figure/`.

[51] U. W. Heinz and M. Jacob, "Evidence for a new state of matter: An Assessment of the results from the CERN lead beam program," 2000.

[52] P. Petreczky, "Lattice QCD at finite temperature," *Nucl.Phys.*, vol. A785, pp. 10–17, 2007.

[53] F. Carminati *et al.*, "ALICE: Physics performance report, volume i," *J.Phys.*, vol. G30, pp. 1517–1763, 2004.

[54] E. Carminati, F *et al.*, "ALICE: Physics performance report, volume I," *J.Phys.G*, vol. G30, pp. 1517–1763, 2004.

[55] A. Kalweit, "Particle Identification in the ALICE Experiment," *J.Phys.*, vol. G38, p. 124073, 2011.

[56] "ALICE central trigger processor (ctp)." `http://epweb2.ph.bham.ac.uk/user/krivda/alice/`.

[57] "The ALICE Offline Bible." `http://aliweb.cern.ch/offine/aliroot/manual.html`.

[58] "The ROOT team users guide." `http://root.cern.ch/root/doc/rootdoc.html`.

[59] NFN, Sezione di Catania Italy, "Resonance measurement in pp and PbPb collisions at LHC with the ALICE detector,"

[60] "PYTHIA home page." `http://home.thep.lu.se/~torbjorn/Pythia`.

[61] Sjöstrand, Torbjorn and Mrenna, Stephen and Skands, Peter Z., "A Brief Introduction to PYTHIA 8.1," *Comput. Phys. Commun.*, vol. 178, pp. 852–867, 2008.

[62] T. Sjöstrand, P. Eden, C. Friberg, L. Lonnblad, G. Miu, *et al.*, "High-energy physics event generation with PYTHIA 6.1," *Comput.Phys.Commun.*, vol. 135, pp. 238–259, 2001.

[63] "Summary of ATLAS Pythia 8 tunes," 2012.

[64] M. R. Whalley, D. Bourilkov, and R. C. Group, "The Les Houches accord PDFs (LHAPDF) and LHAGLUE," in *HERA and the LHC: A Workshop on the implications of HERA for LHC physics. Proceedings, Part B*, 2005.

[65] P. Z. Skands, "Tuning Monte Carlo Generators: The Perugia Tunes," *Phys. Rev.*, vol. D82, p. 074018, 2010.

[66] Ortiz Velásquez, Antonio and Christiansen, Peter and Cuautle Flores, Eleazar and Maldonado Cervantes, Ivonne and Pai, Guy, "Color Reconnection and Flowlike Patterns in *pp* Collisions," *Phys. Rev. Lett.*, vol. 111, no. 4, p. 042001, 2013.

[67] S. Agostinelli and et al., "G4–a simulation toolkit," *Nuclear Instruments and Methods in Physics Research Section A: Accelerators, Spectrometers, Detectors and Associated Equipment*, vol. 506, no. 3, pp. 250 – 303, 2003.

[68] I. Sarcevic, "KNO scaling in hadron hadron collisions," *Acta Phys. Polon.*, vol. B19, p. 361, 1988.

[69] R. Engel and J. Ranft, "Hadronic photon-photon interactions at high-energies," *Phys. Rev.*, vol. D54, pp. 4244–4262, 1996.

[70] "PHOJET home page." `https://opal.web.cern.ch/opal/group/twophoton/tpg/gen/phojet.html`.

[71] T. Sjostrand, S. Mrenna, and P. Z. Skands, "PYTHIA 6.4 Physics and Manual," *JHEP*, vol. 05, p. 026, 2006.

[72] P. Abreu *et al.*, "Production characteristics of K^0 and light meson resonances in hadronic decays of the Z^0," *Z.Phys.*, vol. C65, pp. 587–602, 1995.

[73] J. D. Jackson, "Remarks on the phenomenological analysis of resonances," *Nuovo Cim.*, vol. 34, pp. 1644–1666, 1964.

[74] J. Duenas, N. Gutierrez, R. Martinez, and F. Ochoa, "Z-prime boson signal at Fermilab-Tevatron and CERN-LHC in a 331 model," *Eur.Phys.J.*, vol. C60, pp. 653–659, 2009.

[75] G. D. Lafferty, "Residual Bose-Einstein correlations in inclusive pi+ pi- systems and the $\rho^0(770)$ line shape in multi - hadronic Z^0 decay," *Z. Phys.*, vol. C60, pp. 659–666, 1993.

[76] P. Acton *et al.*, "Inclusive neutral vector meson production in hadronic Z^0 decays," *Z.Phys.*, vol. C56, pp. 521–536, 1992.

[77] "7 tev k^+ spectra vs mc models and ratio." `https://aliceinfo.cern.ch/Figure/node/1700`.

[78] B. Abelev *et al.*, "Production of $K^*(892)^0$ and $\phi(1020)$ in *pp* collisions at $\sqrt{s} = 7$ TeV," *Eur. Phys. J.*, vol. C72, p. 2183, 2012.

[79] B. Abelev *et al.*, "Measurement of inelastic, single- and double-diffraction cross sections in proton–proton collisions at the LHC with ALICE," *Eur. Phys. J. C*, 2012.

[80] "Proton - proton reference spectra." `https://aliceinfo.cern.ch/Notes/node/188`.

[81] K. Aamodt *et al.*, "Transverse momentum spectra of charged particles in proton-proton collisions at $\sqrt{s} = 900$ GeV with ALICE at the LHC," *Phys. Lett.*, vol. B693, pp. 53–68, 2010.

[82] J. Cleymans, "The Tsallis Distribution for p p collisions at the LHC," *J.Phys.Conf.Ser.*, vol. 455, p. 012049, 2013.

[83] C. Tsallis, "Possible generalization of Boltzmann-Gibbs statistics," *Journal of Statistical Physics*, vol. 52, pp. 479–487, July 1988.

[84] Y.-J. Pei, "A Simple approach to describe hadron production rates in e^+ e^- annihilation," *Z.Phys.*, vol. C72, pp. 39–46, 1996.

[85] M. Derrick, P. Kooijman, J. Loos, B. Musgrave, L. Price, *et al.*, "Neutral K*(890) and ρ^0 meson production in e^+ e^- annihilation at $\sqrt{s}$ = 29 GeV," *Phys.Lett.*, vol. B158, p. 519, 1985.

[86] H. Albrecht *et al.*, "Inclusive production of K*(892), $\rho^0(770)$, and $\omega(783)$ mesons in the Υ energy region," *Z.Phys.*, vol. C61, pp. 1–18, 1994.

[87] M. Aguilar-Benítez, W. Allison, A. Batalov, E. Castelli, P. Cecchia, *et al.*, "Inclusive particle production in 400-GeV/c p p interactions," *Z.Phys.*, vol. C50, pp. 405–426, 1991.

[88] R. Singer, T. Fields, L. Hyman, R. Engelmann, T. Kafka, *et al.*, "ρ^0 Production in 205 GeV/c proton proton interactions," *Phys.Lett.*, vol. B60, p. 385, 1976.

[89] V. Blobel and et al., "Observation of Vector Meson Production in Inclusive p p Reactions," *Phys.Lett.*, vol. B48, p. 73, 1974.

APPENDIX A

APPENDIX

Figures A.1 and A.2 shows the fitting process as discussed in section 3.3 to each of the studied p_t regions. It is from these fittings that the spectra of the desired ρ (770), f_0 (980) and f_2 (1270) peaks are extracted as seen in section 4.5.1. From these fittings figure A.3 shows the χ^2 / NDF value for the fitted spectra in each of these p_t regions.

The residual background estimation in each of the studied p_t regions within the MC study is shown in figures A.4 and A.5. Figures A.6 and A.7 also show the extra residual background component used by estimating the difference between the $\pi^+ \pi^-$

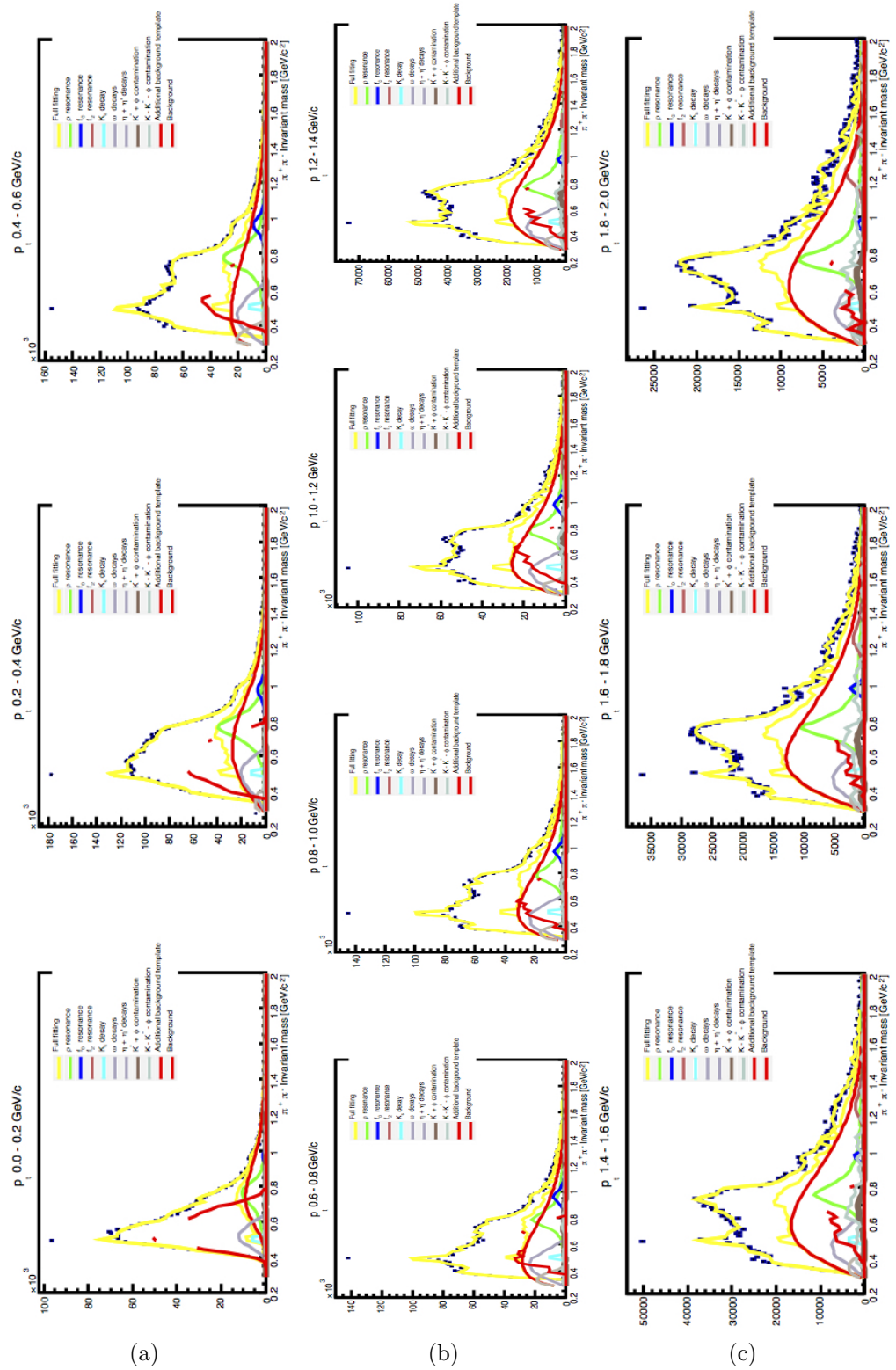

Figure A.1: Fitting process applied to each of the p_t regions (0.0 - 2.0 GeV/c), in order to extract the desired resonances.

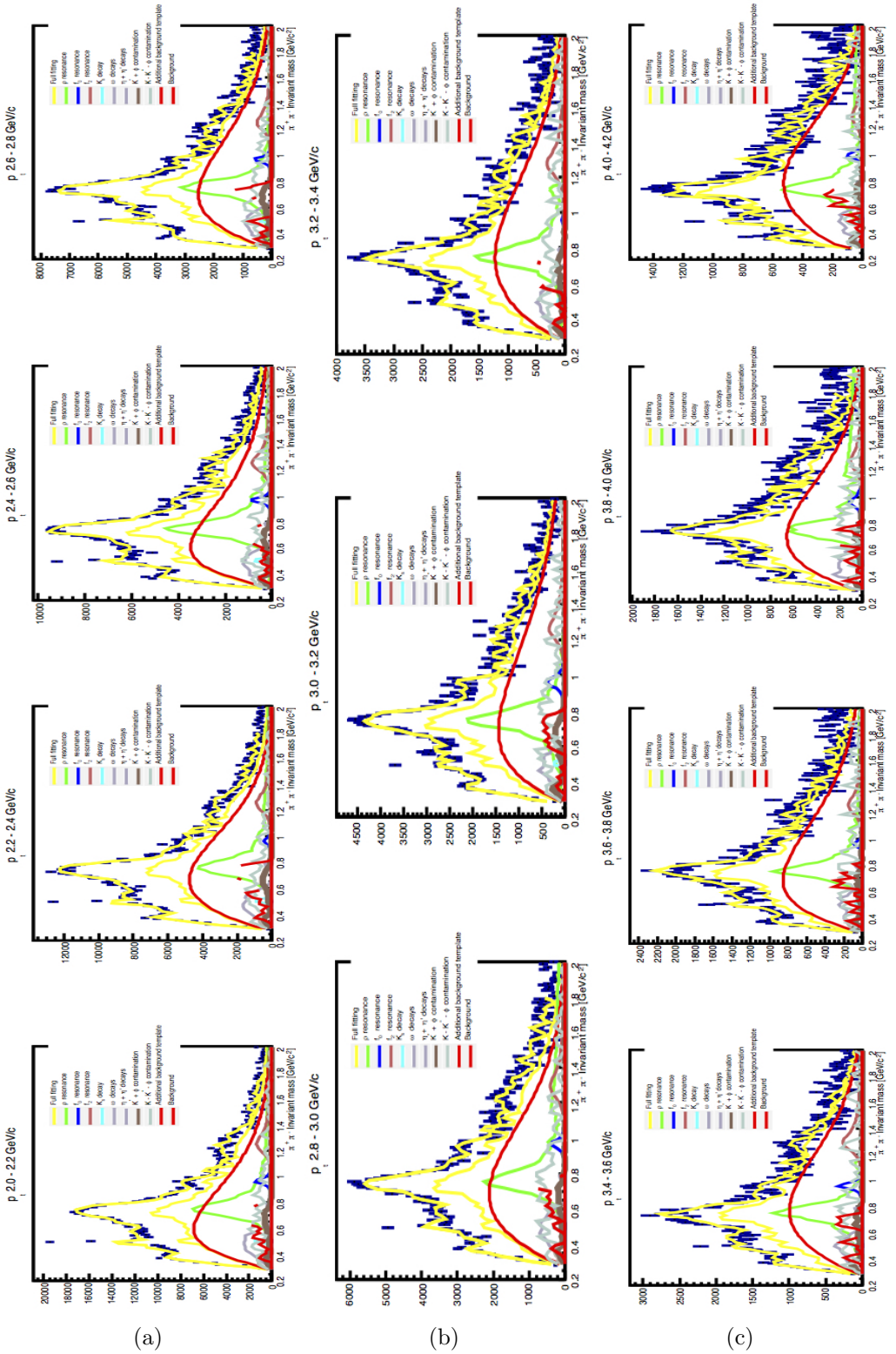

(a) (b) (c)

Figure A.2: Fitting process applied to each of the p_t regions (2.0 - 4.2 GeV/c), in order to extract the desired resonances.

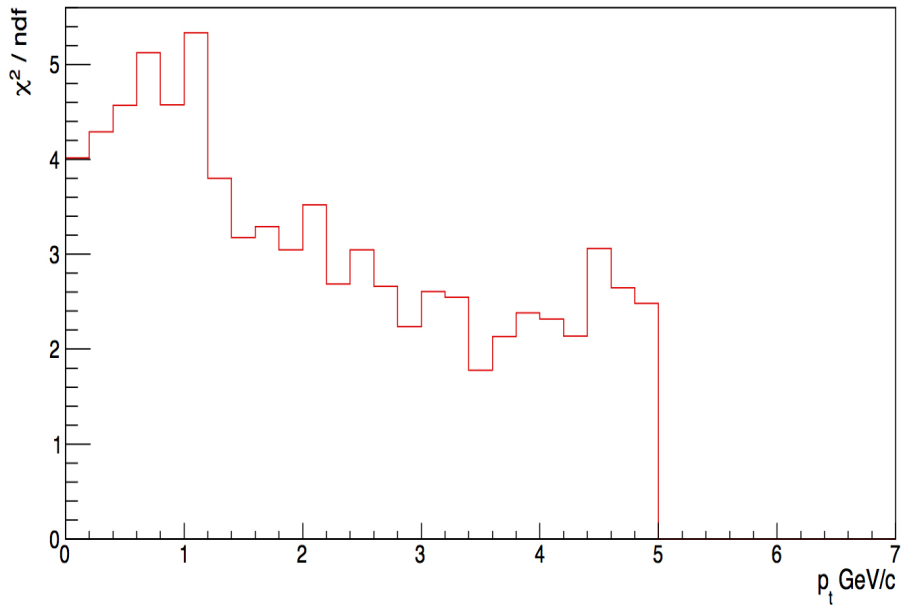

Figure A.3: Value of the χ^2 / NDF for each fitting applied to each of the p_t regions from 0.0 to 5.0 GeV/c.

spectrum obtained in the MC and the spectrum obtained in data after normalisation to the number of events in both. From figures A.6 and A.7 it is shown how this mismatch between the data and MC spectra is most prominent in the low mass and low p_t regions, most likely due to a mis-modelling of the mini-jets within the studied collision set.

Figures A.8 and A.9 show the detection acceptance efficiency calculated within the MC study for the ρ peak as a function of invariant mass as discussed in section 3.2.2. The efficiencies are applied to each of the fitted p_t regions as shown in figures A.1 and A.2. This is to correct for the efficiency effects when extracting the yield and mass values from the desired ρ peak and also to correct for the distortions the reconstruction introduces by modifying the fitted ρ peak shape by using the efficiency calculated in figures A.8 and A.9.

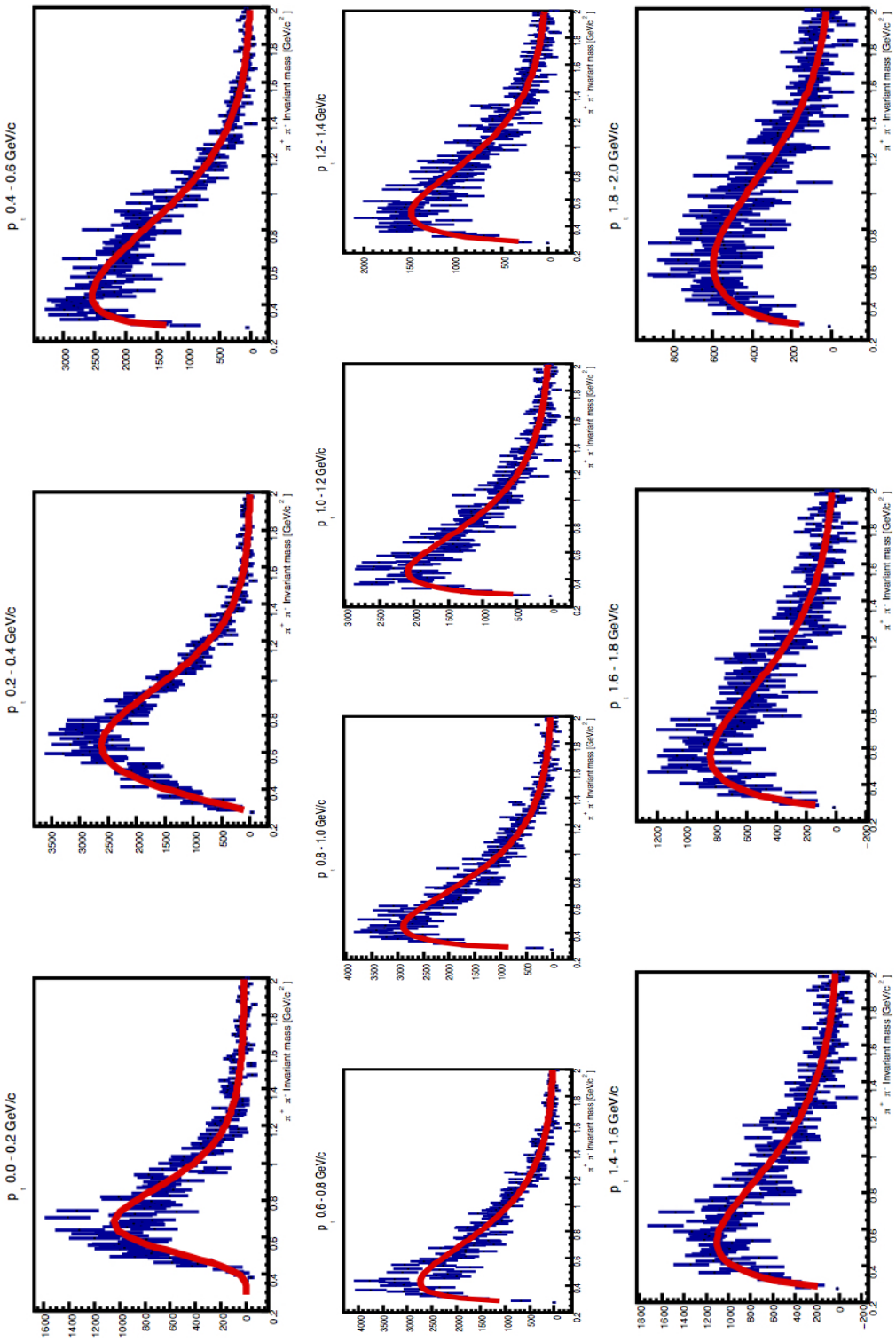

Figure A.4: Non-resonant background as computed by the MC pion tracks from non-identifiable origins in each studied p_t region (0.0 - 2.0 GeV/c).

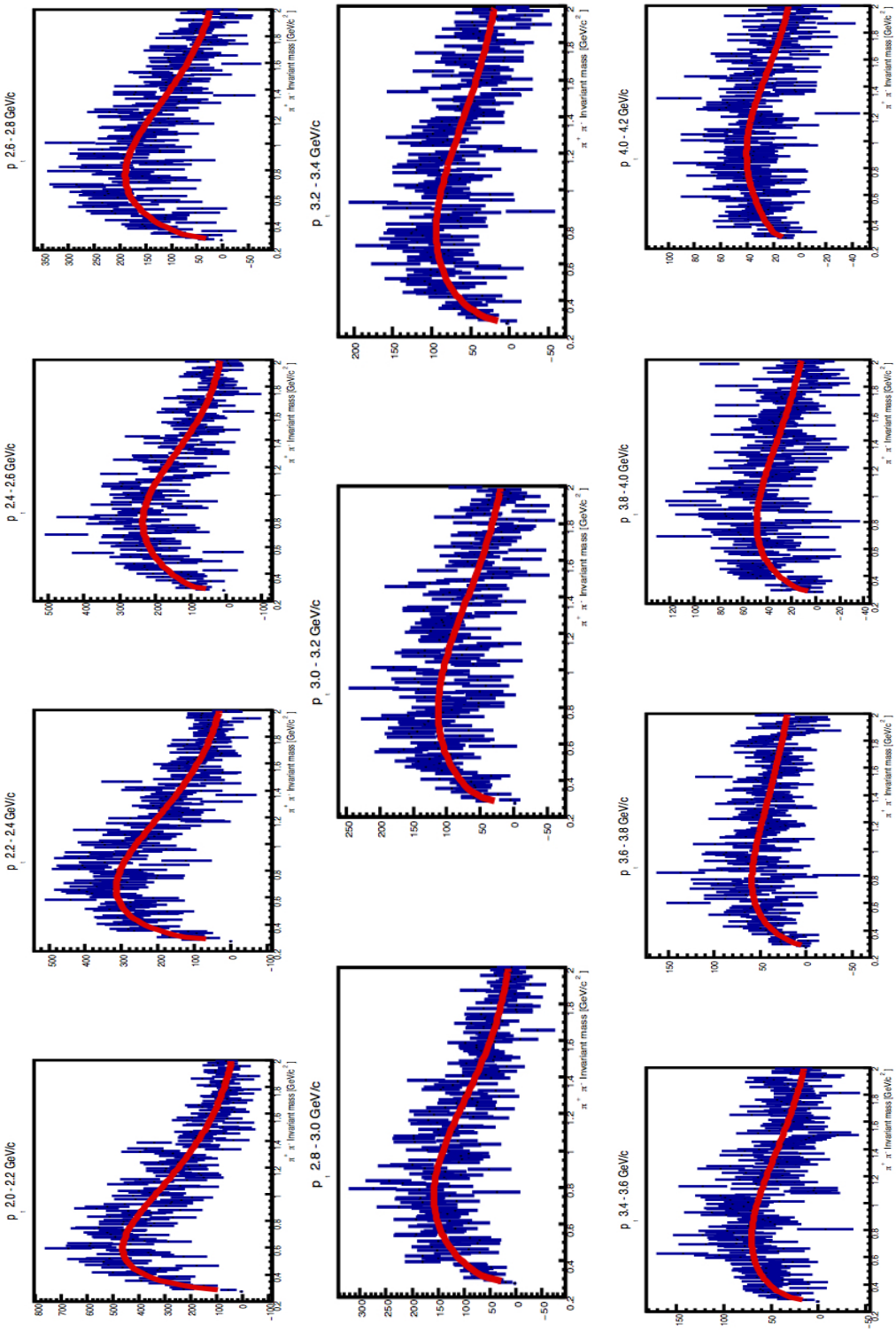

(a) (b) (c)

Figure A.5: Non-resonant background as computed by the MC pion tracks from non-identifiable origins in each studied p_t region (2.0 - 4.2 GeV/c).

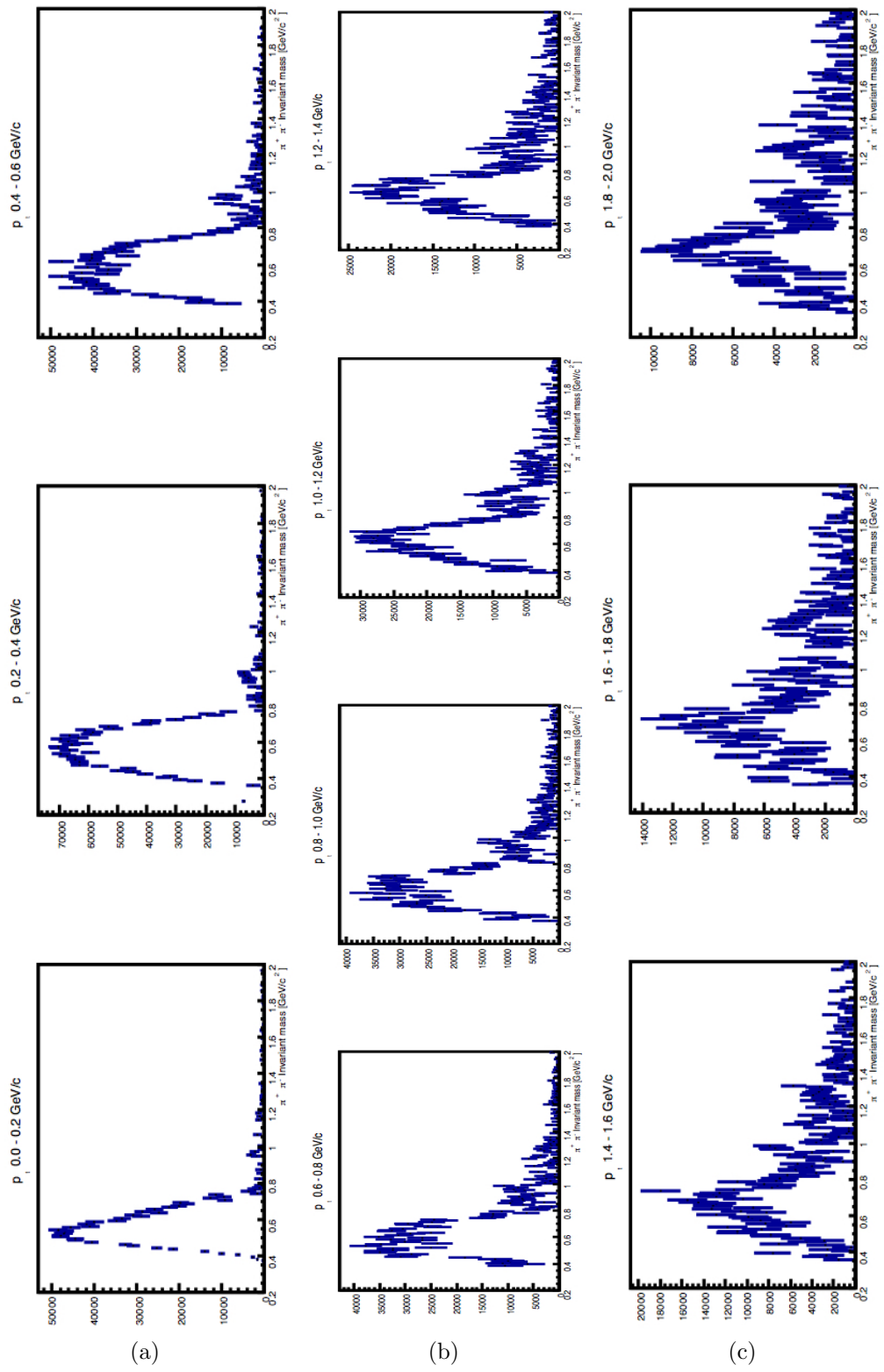

Figure A.6: Non-resonant background template as computed by normalising the π^+ π^- MC spectrum to the number of events studied within the data analysis and subtracting it from the spectrum obtained in the data analysis in each studied p_t region (0.0 - 2.0 GeV/c).

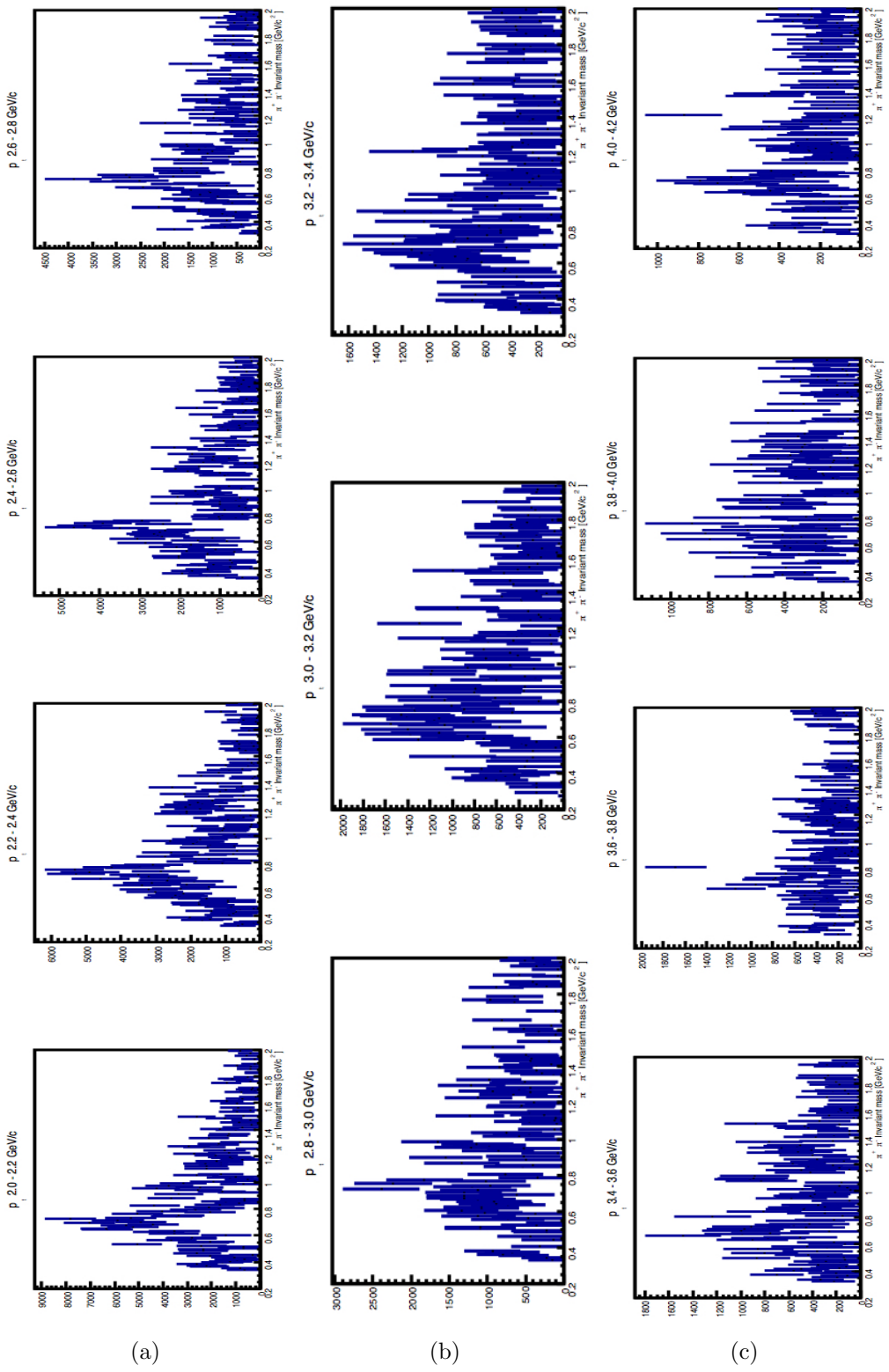

(a) (b) (c)

Figure A.7: Non-resonant background template as computed by normalising the π^+ π^- MC spectrum to the number of events studied within the data analysis and subtracting it from the spectrum obtained in the data analysis in each studied p_t region (2.0 - 4.2 GeV/c).

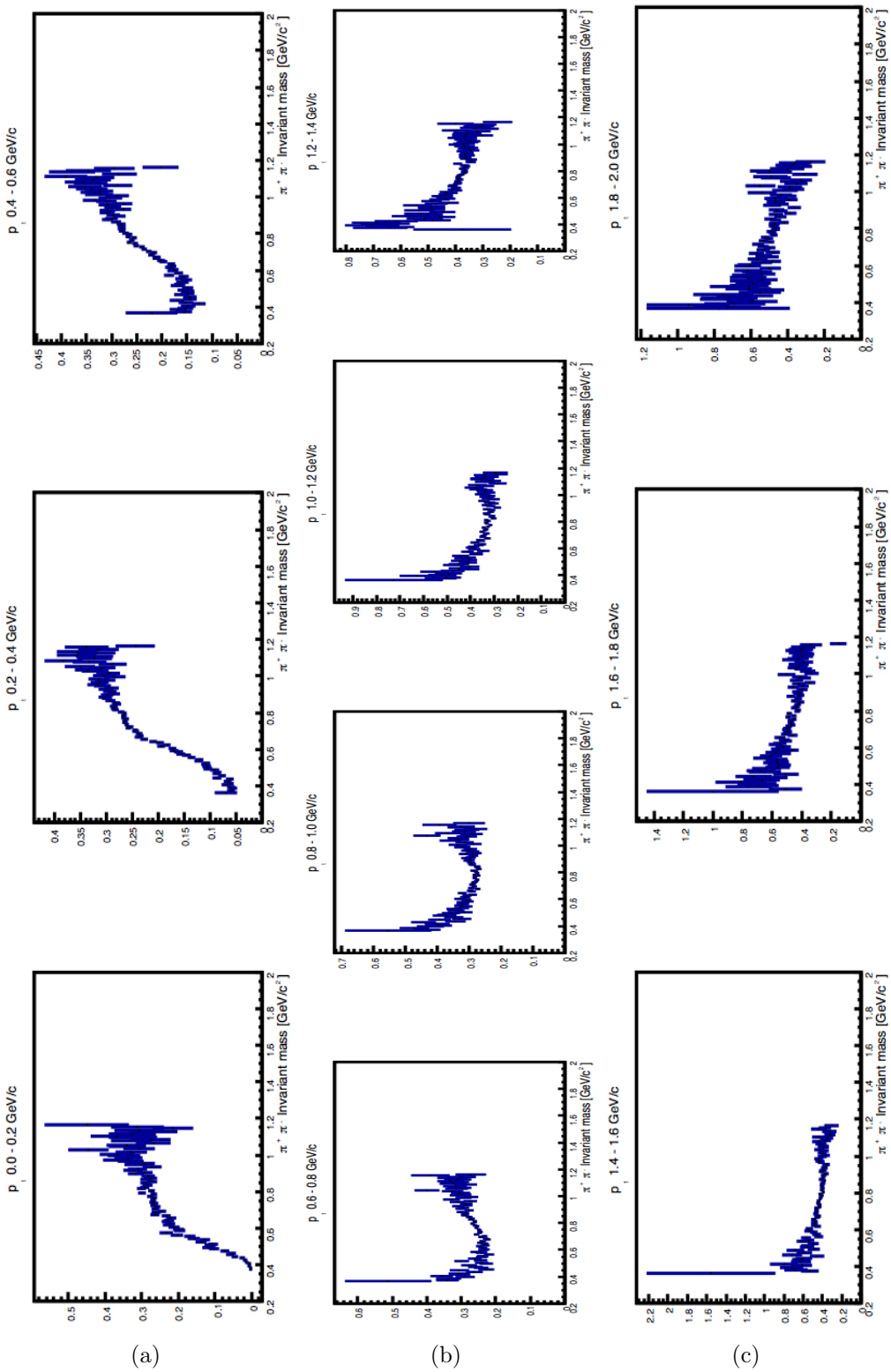

Figure A.8: Invariant mass dependent efficiency calculated using the generated and reconstructed ρ peak within the MC study.

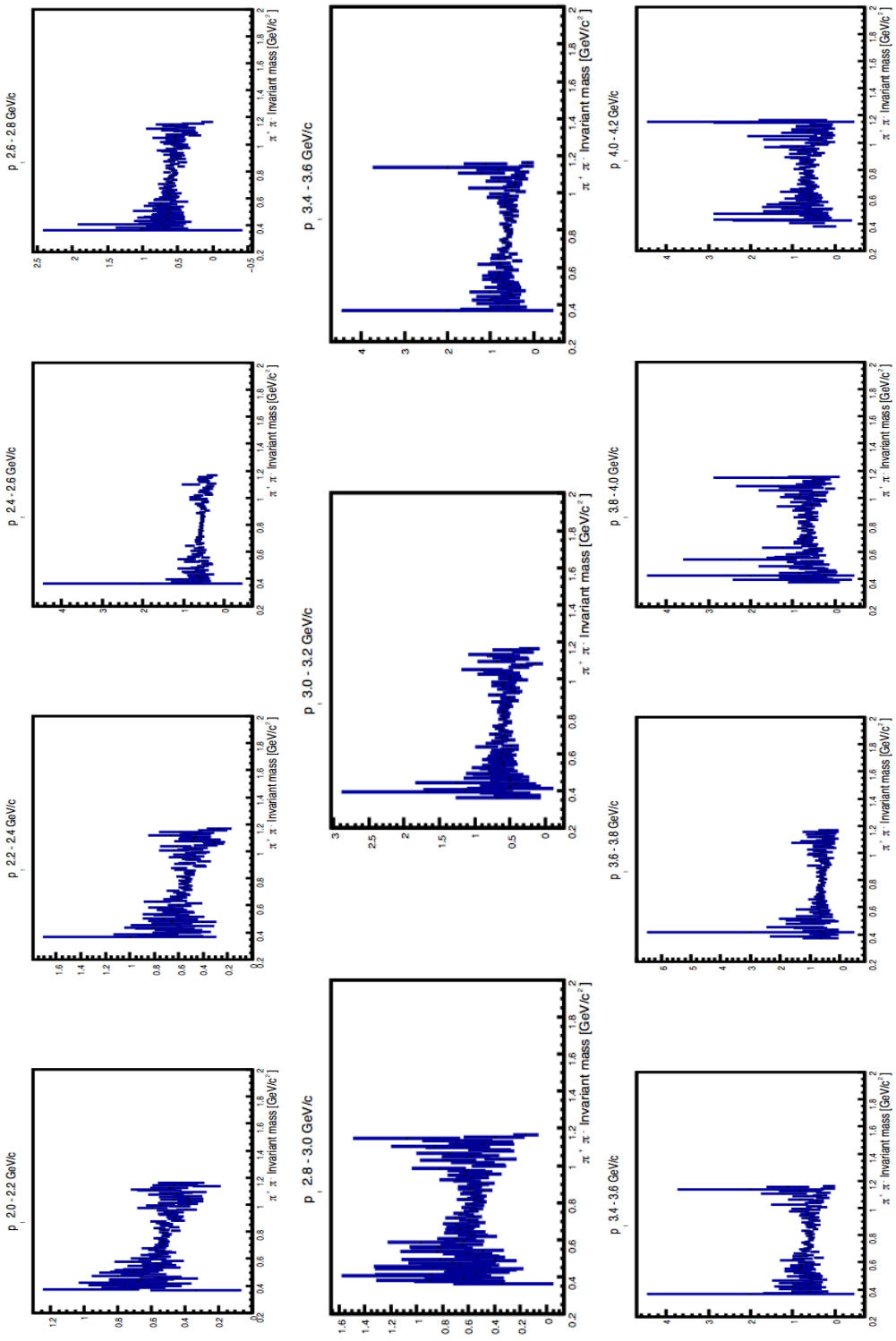

(a) (b) (c)

Figure A.9: Invariant mass dependent efficiency calculated using the generated and reconstructed ρ peak within the MC study; in bins of p_t

Tables A.1, A.2, A.3 and A.4 show the computation of the estimation for the systematic uncertainties applied to the stated results of the normalised yield of the spectrum value ($\mathrm{d}N/\mathrm{d}y$), mean p_t value ($\langle p_t \rangle$) and the n and T values of the fitted Tsallis function (equation 4.4) respectively for the extracted ρ (770). The estimations show the main sources of error, in the size and shape of the extracted ρ spectrum, originates from the chosen fitting range of the π^+ π^- spectrum, most likely due to the difference in constraints the different fitting ranges impose on the residual background shape in the low p_t regions.

Table A.5 show the computation of the estimation for the systematic uncertainties applied to the mass value of the ρ peak from the fitting of the p_t integrated π^+ π^- spectrum.

Tables A.6, A.7, A.8 and A.9 show the computation of the estimation for the systematic uncertainties applied to the stated results of the normalised yield of the spectrum value ($\mathrm{d}N/\mathrm{d}y$), mean p_t value ($\langle p_t \rangle$) and the n and T values of the fitted Tsallis function (equation 4.4) respectively for the extracted f_0 (980). The estimations show the main sources of error in the size and shape of the extracted f_0 spectrum originates from a wider range of sources than the ρ but still mostly caused by the fitting range and the choice of PID cut. This is mostly due to the dependence the f_0 peak has on the ρ peak shape more than the residual background shape. This imposes an increased effect on the f_0 peak from the sources of systematic uncertainty that affect the ρ peak.

Tables A.10 and A.11 show the computation of the estimation for the systematic

Table A.1: Systematic error estimation for the total normalised yield of the ρ (770) spectrum.

	dN/dy	Difference	Difference (%)
dN/dy with default parameters	0.337	N/A	N/A
Fitting range 0.28 - 1.9 GeV/c	0.335	1.5E-3	0.43
Fitting range 0.28 - 2.0 GeV/c	0.334	2.7E-3	0.79
Fitting range 0.40 - 1.8 GeV/c	0.292	4.5E-2	13.5
Fitting range 0.50 - 1.8 GeV/c	0.281	5.6E-2	16.7
Average systematic for fitting range		2.6E-2	7.84
	dN/dy	Difference	Difference (%)
dN/dy with default parameters	0.337	N/A	N/A
DCA$_z$ = 0.3 cm	0.343	5.7E-3	1.69
DCA$_z$ = 0.1 cm	0.317	2E-2	5.89
DCA$_r$ = 6 σ	0.337	4E-6	1.19E-3
DCA$_r$ = 8 σ	0.337	2E-5	5.94E-3
Minimum track p_t = 0.2 GeV/c	0.294	4.3E-2	12.7
TPC minimum number of clusters = 50	0.342	4.6E-3	1.37
TPC max χ^2 = 6	0.339	2.49E-3	0.738
Average systematic for track cuts		7.1E-3	2.11
	dN/dy	Difference	Difference (%)
dN/dy with default parameters	0.337	N/A	N/A
PID No PID	0.341	3.8E-3	1.14
PID n_σ = 1	0.276	6.1E-2	18.01
Average systematic for PID cut		2.8E-2	8.43
Template constraints	0.336	6.9E-4	0.206
MC choice	0.322	1.5E-2	4.54
Efficiency correction method	0.344	7.4E-3	2.19
Phase Space correction	0.334	3.3E-3	0.987
Average systematic for peak shape		3.9E-4	0.12
Total syst		4.23E-2	12.6

Table A.2: Systematic error estimation for the $\langle p_t \rangle$ result of the ρ (770) spectrum.

	$\langle p_t \rangle$	Difference	Difference (%)
$\langle p_t \rangle$ with default parameters	0.876	N/A	N/A
Fitting range 0.28 - 1.9 GeV/c	0.874	1.7E-3	0.189
Fitting range 0.28 - 2.0 GeV/c	0.877	1.3E-3	0.15
Fitting range 0.40 - 1.8 GeV/c	0.966	8.9E-2	10.3
Fitting range 0.50 - 1.8 GeV/c	0.995	0.119	13.6
Average systematic for fitting range		5.2E-2	5.95
	$\langle p_t \rangle$	Difference	Difference (%)
$\langle p_t \rangle$ with default parameters	0.876	N/A	N/A
DCA$_z$ = 0.3 cm	0.87	6.4E-3	0.726
DCA$_z$ = 0.1 cm	0.897	2.2E-2	2.47
DCA$_r$ = 6 σ	0.876	4.2E-5	4.8E-3
DCA$_r$ = 8 σ	0.876	3.5E-5	3.9E-3
Minimum track p_t = 0.2 GeV/c	0.932	5.6E-2	6.43
TPC minimum number of clusters = 50	0.88	4.4E-3	0.49
TPC max χ^2 = 6	0.876	9.9E-5	1.1E-2
Average systematic for track cuts		1.1E-2	1.24
	$\langle p_t \rangle$	Difference	Difference (%)
$\langle p_t \rangle$ with default parameters	0.876	N/A	N/A
PID No PID	0.879	3.8E-3	0.44
PID n_σ = 1	0.892	1.7E-2	1.91
Average systematic for PID		1.02E-2	1.17
Template constraints	0.912	3.6E-2	4.167
MC choice	0.848	2.7E-2	3.13
Efficiency correction method	0.859	1.7E-2	1.89
Phase Space correction	0.873	2.7E-3	0.309
Average systematic for peak shape		9.8E-3	1.12
Total syst		7.2E-2	8.17

Table A.3: Systematic error estimation for the T parameter in the ρ (770) spectrum Tsallis function (equation 4.4) fitting.

	T	Difference	Difference (%)
T value with default parameters	0.188	N/A	N/A
Fitting range 0.28 - 1.9 GeV/c	0.186	1.6E-3	0.845
Fitting range 0.28 - 2.0 GeV/c	0.186	1.9E-3	0.986
Fitting range 0.40 - 1.8 GeV/c	0.253	6.5E-2	34.5
Fitting range 0.50 - 1.8 GeV/c	0.286	9.8E-2	51.9
Average systematic for fitting range		3.9E-2	21.2
	T	Difference	Difference (%)
T value with default parameters	0.188	N/A	N/A
DCA$_z$ = 0.3 cm	0.187	7.7E-4	0.413
DCA$_z$ = 0.1 cm	0.198	9.8E-3	5.21
DCA$_r$ = 6 σ	0.189	1.2E-5	6.4E-3
DCA$_r$ = 8 σ	0.188	1.9E-5	1.1E-2
Minimum track p_t = 0.2 GeV/c	0.219	3.1E-2	16.6
TPC minimum number of clusters = 50	0.187	5.1E-4	0.273
TPC max χ^2 = 6	0.189	1.1E-3	0.610
Average systematic for cuts		5.8E-3	3.10
	T	Difference	Difference (%)
T value with default parameters	0.188	N/A	N/A
PID No PID	0.182	5.8E-3	3.11
PID n_σ = 1	0.169	1.9E-2	10.3
Average systematic for PID		1.3E-2	6.69
Template constraints	0.223	3.5E-2	18.6
MC choice	0.168	1.9E-2	10.5
Efficiency correction method	0.178	1.1E-2	5.67
Phase Space correction	0.182	5.8E-3	3.071
Average systematic for peak shape		9.7E-3	5.15
Total syst		5.9E-2	31.4

Table A.4: Systematic error estimation for the n parameter in the ρ (770) spectrum Tsallis function (equation 4.4) fitting.

	n	Difference	Difference (%)
n value with default parameters	4.87	N/A	N/A
Fitting range 0.28 - 1.9 GeV/c	4.83	3.9E-2	0.799
Fitting range 0.28 - 2.0 GeV/c	4.79	7.8E-2	1.61
Fitting range 0.40 - 1.8 GeV/c	6.39	1.53	31.4
Fitting range 0.50 - 1.8GeV/c	7.72	2.85	58.6
Average systematic for fitting range		1.07	21.9
	n	Difference	Difference (%)
n value with default parameters	4.87	N/A	N/A
DCA$_z$ = 0.3 cm	4.91	0.04	0.815
DCA$_z$ = 0.1 cm	4.99	0.119	2.44
DCA$_r$ = 6 σ	4.87	0	6E-3
DCA$_r$ = 8 σ	4.87	0	7E-3
Minimum track p_t = 0.2 GeV/c	5.39	0.519	10.7
TPC minimum number of clusters = 50	4.81	6.3E-2	1.29
TPC max χ^2 = 6	4.91	4.2E-2	0.864
Average systematic for cuts		9.4E-2	1.92
	n	Difference	Difference (%)
n value with default parameters	4.87	N/A	N/A
PID No PID	4.63	0.237	4.86
PID n_σ = 1	4.13	0.737	15.14
Average systematic for PID		0.487	9.99
Template constraints	5.83	0.957	19.6
MC choice	4.47	0.401	8.23
Efficiency correction method	4.67	0.203	4.17
Phase Space correction	4.69	0.172	3.531
Average systematic for peak shape		0.234	4.803
Total syst		1.585	32.5

Table A.5: Systematic error estimation for the mass measurement for the ρ (770) peak fitting in the p_t integrated π^+ π^- spectrum.

	Mass	Difference	Difference (%)
Mass value with default parameters	7.77	N/A	N/A
Fitting range 0.28 - 1.9 GeV/c	7.77	2.7E-3	3.4E-2
Fitting range 0.28 - 2.0 GeV/c	7.77	2.8E-3	3.6E-2
Fitting range 0.40 - 1.8 GeV/c	7.65	0.12	1.55
Fitting range 0.50 - 1.8 GeV/c	7.63	0.14	1.74
Average systematic for fitting range		6.3E-2	0.804
	Mass	Difference	Difference (%)
Mass value with default parameters	7.77	N/A	N/A
DCA$_z$ = 0.3 cm	7.78	2.5E-3	3.2E-2
DCA$_z$ = 0.1 cm	7.78	9.5E-3	0.12
DCA$_r$ = 6 σ	7.77	2.0E-5	2.6E-4
DCA$_r$ = 8 σ	7.77	7.7E-4	9.9E-3
Minimum track p_t = 0.2	7.79	1.6E-2	0.21
TPC minimum number of clusters = 50	7.79	1.64E-2	0.21
TPC max χ^2 = 6	7.77	8.3E-4	1.1E-2
Average systematic for cuts		5.9E-3	7.6E-2
	Mass	Difference	Difference (%)
Mass value with default parameters	7.77	N/A	N/A
PID No PID	7.77	2.4E-3	3.1E-2
PID n_σ = 1	7.79	2.2E-2	0.29
Average systematic for PID		1.2E-2	0.16
Template constraints	7.77	1.6E-4	2.1E-3
MC choice	7.77	3.3E-3	4.3E-2
Efficiency correction method	7.75	1.8E-2	0.24
Phase Space correction	7.73	3.6E-2	0.47
Average systematic for peak shape		2.7E-2	0.35
Total syst		6.9E-2	0.90

Table A.6: Systematic error estimation for the total normalised yield of the f_0 (980) spectrum.

	dN/dy	Difference	Difference (%)
dN/dy with default parameters	0.124	N/A	N/A
Fitting range 0.28 - 1.9 GeV/c	0.123	3.8E-4	0.307
Fitting range 0.28 - 2.0 GeV/c	0.123	8.8E-4	0.709
Fitting range 0.40 - 1.8 GeV/c	9.0E-2	3.3E-2	26.9
Fitting range 0.50 - 1.8 GeV/c	8.9E-2	3.5E-2	28.19
Average systematic for fitting range		1.7E-2	14.02
	dN/dy	Difference	Difference (%)
dN/dy with default parameters	0.124	N/A	N/A
DCA$_z$ = 0.3 cm	0.127	3.89E-3	3.15
DCA$_z$ = 0.1 cm	0.114	9.3E-3	7.56
DCA$_r$ = 6 σ	0.124	4.0E-6	3.2E-3
DCA$_r$ = 8 σ	0.124	4.1E-4	0.337
Minimum track p_t = 0.2 GeV/c	0.117	6.3E-3	5.09
TPC minimum number of clusters = 50	0.124	6.8E-4	0.548
TPC max χ^2 = 6	0.124	6.3E-4	0.512
Average systematic for cuts		1.4E-3	1.16
	dN/dy	Difference	Difference (%)
dN/dy with default parameters	0.124	N/A	N/A
PID No PID	0.134	1.0E-2	8.29
PID n_σ = 1	0.128	4.1E-3	3.30
Average systematic for PID		7.2E-3	5.79
Template constraints	0.123	6.6E-4	0.537
MC choice	0.119	4.7E-3	3.79
Efficiency correction method	0.119	4.5E-3	3.66
Phase Space correction	0.124	1.9E-4	0.162
Average systematic for peak shape		4.2E-3	3.36
Total syst		1.98E-2	16.05

Table A.7: Systematic error estimation for the $\langle p_t \rangle$ result of the f_0 (980) spectrum.

	$\langle p_t \rangle$	Difference	Difference (%)
$\langle p_t \rangle$ with default parameters	0.852	N/A	N/A
Fitting range 0.28 - 1.9 GeV/c	0.851	9.7E-4	0.114
Fitting range 0.28 - 2.0 GeV/c	0.857	4.6E-3	0.543
Fitting range 0.40 - 1.8 GeV/c	0.811	4.1E-2	4.78
Fitting range 0.50 - 1.8 GeV/c	0.813	3.9E-2	4.60
Average systematic for fitting range		1.9E-2	2.24
	$\langle p_t \rangle$	Difference	Difference (%)
$\langle p_t \rangle$ with default parameters	0.852	N/A	N/A
DCA$_z$ = 0.3 cm	0.846	5.8E-3	0.679
DCA$_z$ = 0.1 cm	0.852	4.8E-4	5.6E-2
DCA$_r$= 6 σ	0.852	2.3E-5	2.7E-3
DCA$_r$ = 8 σ	0.850	1.9E-3	0.228
Minimum track p_t = 0.2 GeV/c	0.812	3.9E-2	4.68
TPC minimum number of clusters = 50	0.864	1.1E-2	1.32
TPC max χ^2 = 6	0.851	1.2E-3	0.139
Average systematic for cuts		5.4E-3	0.638
	$\langle p_t \rangle$	Difference	Difference (%)
$\langle p_t \rangle$ with default parameters	0.852	N/A	N/A
PID No PID	0.763	8.9E-2	10.4
PID n_σ = 1	0.786	6.6E-2	7.76
Average systematic for PID		7.8E-2	9.10
Template constraints	0.843	8.7E-3	1.02
MC choice	0.884	3.2E-2	3.73
Efficiency correction method	0.871	1.9E-2	2.24
Phase Space correction	0.846	6.5E-3	0.764
Average systematic for peak shape		1.9E-2	2.22
Total syst		8.9E-2	10.4

Table A.8: Systematic error estimation for the T parameter in the f_0 (980) spectrum Tsallis function (equation 4.4) fitting.

	T	Difference	Difference (%)
T value with default parameters	0.209	N/A	N/A
Fitting range 0.28 - 1.9 GeV/c	0.207	1.6E-3	0.754
Fitting range 0.28 - 2.0 GeV/c	0.208	7.3E-4	0.348
Fitting range 0.40 - 1.8 GeV/c	0.139	7.0E-2	33.5
Fitting range 0.50 - 1.8 GeV/c	0.145	6.4E-2	30.7
Average systematic for fitting range		3.4E-2	16.3
	T	Difference	Difference (%)
T value with default parameters	0.209	N/A	N/A
DCA$_z$ = 0.3 cm	0.213	3.7E-3	1.77
DCA$_z$ = 0.1 cm	0.202	6.5E-3	3.10
DCA$_r$ = 6 σ	0.209	5.0E-6	2.3E-3
DCA$_r$ = 8 σ	0.210	6.0E-4	0.290
Minimum track p_t = 0.2 GeV/c	0.172	3.7E-2	17.8
TPC minimum number of clusters = 50	0.213	4.4E-3	2.11
TPC max χ^2 = 6	0.208	1.3E-3	0.646
Average systematic for cuts		5.2E-3	2.488
	T	Difference	Difference (%)
T value with default parameters	0.209	N/A	N/A
PID No PID	0.173	3.6E-2	17.3
PID n_σ = 1	0.194	1.5E-2	7.15
Average systematic for PID		2.6E-2	12.2
Template constraints	0.207	2.3E-3	1.09
MC choice	0.248	3.9E-2	18.5
Efficiency correction method	0.242	3.3E-2	15.8
Phase Space correction	0.211	2.2E-3	1.06
Average systematic for peak shape		2.7E-2	13.0
Total syst		6.4E-2	30.6

Table A.9: Systematic error estimation for the n parameter in the f_0 (980) spectrum Tsallis function (equation 4.4) fitting.

	n	Difference	Difference (%)
n value with default parameters	7.16	N/A	N/A
Fitting range 0.28 - 1.9 GeV/c	7.06	0.100	1.40
Fitting range 0.28 - 2.0 GeV/c	6.97	0.186	2.59
Fitting range 0.40 - 1.8 GeV/c	4.16	2.99	41.9
Fitting range 0.50 - 1.8 GeV/c	4.35	2.81	39.3
Average systematic for fitting range		1.52	21.3
	n	Difference	Difference (%)
n value with default parameters	7.16	N/A	N/A
DCA$_z$ = 0.3 cm	7.66	0.503	7.02
DCA$_z$ = 0.1 cm	6.67	0.485	6.78
DCA$_r$ = 6 σ	7.16	2.2E-4	3.1E-3
DCA$_r$ = 8 σ	7.26	0.107	1.49
Minimum track p_t = 0.2 GeV/c	5.54	1.62	22.6
TPC minimum number of clusters = 50	7.20	4.0E-2	0.553
TPC max χ^2 = 6	7.08	7.6E-2	1.07
Average systematic for cuts		0.219	3.06
	n	Difference	Difference (%)
n value with default parameters	7.16	N/A	N/A
PID No PID	6.64	0.515	7.19
PID n_σ = 1	7.95	0.788	11.0
Average systematic for PID		0.138	1.91
Template constraints	7.22	6.1E-2	0.854
MC choice	8.02	0.860	12.0
Efficiency correction method	7.00	0.151	2.10
Phase Space correction	7.55	0.390	5.45
Average systematic for peak shape		0.127	1.77
Total syst		1.77	24.8

uncertainties applied to the mass and width values of the f_0 peak from the fitting of the p_t integrated π^+ π^- spectrum.

Tables A.12, A.13, A.14 and A.15 show the computation of the estimation for the systematic uncertainties applied to the stated results of the normalised yield of the spectrum value ($\mathrm{d}N/\mathrm{d}y$), mean p_t value ($\langle p_t \rangle$) and the n and T values of the fitted Tsallis function (equation 4.4) respectively for the extracted f_2 (1270). The estimations show the main sources of error in the size and shape of the extracted f_2 spectrum originate from different sources for different measured values. This is due to the low statistics of the f_2 peak as compared to the other extracted peaks as well as the dependence it has on the residual background, which in turn has a large dependence on the size and shape of the template used within the fitting process.

Tables A.16 and A.11 show the computation of the estimation for the systematic uncertainties applied to the mass and width values of the f_2 peak from the fitting of the p_t integrated π^+ π^- spectrum.

Table A.10: Systematic error estimation for the mass measurement for the f_0 (980) peak fitting in the p_t integrated π^+ π^- spectrum.

	Mass	Difference	Difference (%)
Mass value with default parameters	9.69	N/A	N/A
Fitting range 0.28 - 1.9 GeV/c	9.69	1.9E-4	1.9E-3
Fitting range 0.28 - 2.0 GeV/c	9.69	2.0E-4	2.1E-3
Fitting range 0.40 - 1.8 GeV/c	9.70	1.7E-2	0.17
Fitting range 0.50 - 1.8 GeV/c	9.71	1.9E-2	0.20
Average systematic for fitting range		8.7E-3	9.0E-2
	Mass	Difference	Difference (%)
Mass value with default parameters	9.69	N/A	N/A
DCA$_z$ = 0.3 cm	9.69	3.4E-3	3.5E-2
DCA$_z$ = 0.1 cm	9.69	9.4E-4	9.7E-3
DCA$_r$ = 6 σ	9.69	3.0E-5	3.1E-4
DCA$_r$ = 8 σ	9.69	1.9E-3	1.9E-2
Minimum track p_t = 0.2 GeV/c	9.69	3.2E-3	3.3E-2
TPC minimum number of clusters = 50	9.69	1.1E-3	1.2E-2
TPC max χ^2 = 6	9.69	5.6E-4	5.8E-3
Average systematic for cuts		8.9E-4	9.3E-3
	Mass	Difference	Difference (%)
Mass value with default parameters	9.69	N/A	N/A
PID No PID	9.65	4.6E-2	0.47
PID n_σ = 1	9.71	1.3E-2	0.13
Average systematic for PID		1.6E-2	0.17
Template constraints	9.69	4.7E-3	4.9E-2
MC choice	9.69	4.0E-3	4.1E-2
Efficiency correction method	9.69	0	0
Phase Space correction	9.69	1.6E-3	1.69E-2
Average systematic for peak shape		8.2E-4	8.4E-3
Total syst		0.020	0.203

Table A.11: Systematic error estimation for the width measurement for the f_0 (980) peak fitting in the p_t integrated π^+ π^- spectrum.

	Width	Difference	Difference (%)
Width value with default parameters	6.87	N/A	N/A
Fitting range 0.28 - 1.9 GeV/c	6.83	3.9E-2	0.57
Fitting range 0.28 - 2.0 GeV/c	6.83	4.1E-2	0.59
Fitting range 0.40 - 1.8 GeV/c	5.43	1.43	20.87
Fitting range 0.50 - 1.8 GeV/c	5.12	1.74	25.38
Average systematic for fitting range		0.81	11.85
	Width	Difference	Difference (%)
Width value with default parameters	6.87	N/A	N/A
DCA$_z$ = 0.3 cm	6.70	0.16	2.36
DCA$_z$ = 0.1 cm	7.02	0.16	2.26
DCA$_r$ = 6 σ	6.87	4.7E-4	6.8E-3
DCA$_r$ = 8 σ	6.91	4.4E-2	0.64
Minimum track p_t = 0.2 GeV/c	7.20	0.33	4.85
TPC minimum number of clusters = 50	6.67	0.20	2.85
TPC max χ^2 = 6	6.88	1.3E-2	0.19
Average systematic for cuts		2.7E-2	0.39
	Width	Difference	Difference (%)
Width value with default parameters	6.87	N/A	N/A
PID No PID	7.1	0.23	3.4
PID n_σ = 1	7.98	1.10975	16.16
Average systematic for PID		0.67	9.78
Template constraints	6.55	0.32	4.62
MC choice	6.88	1.8E-2	0.26
Efficiency correction method	6.87	1.0E-5	1.5E-4
Phase Space correction	7.44	0.57	8.28
Average systematic for peak shape		0.28	4.14
Total syst		1.14	16.58

Table A.12: Systematic error estimation for the total normalised yield of the f_2 (1270) spectrum.

	dN/dy	Difference	Difference (%)
dN/dy with default parameters	0.150	N/A	N/A
Fitting range 0.28 - 1.9 GeV/c	0.150	1.2E-4	8.0E-2
Fitting range 0.28 - 2.0 GeV/c	0.147	2.4E-3	1.6
Fitting range 0.40 - 1.8 GeV/c	0.148	1.8E-3	1.17
Fitting range 0.50 - 1.8 GeV/c	0.142	7.7E-3	5.15
Average systematic for fitting range		2.9E-3	1.97
	dN/dy	Difference	Difference (%)
dN/dy with default parameters	0.150	N/A	N/A
DCA$_z$ = 0.3 cm	0.152	1.9E-3	1.24
DCA$_z$ = 0.1 cm	0.134	1.57E-2	10.5
DCA$_r$ = 6 σ	0.150	1.5E-4	0.102
DCA$_r$ = 8 σ	0.152	1.8E-3	1.17
Minimum track p_t = 0.2 GeV/c	0.17149	2.2E-2	14.4
TPC minimum number of clusters = 50	0.156	6.3E-3	4.20
TPC max χ^2 = 6	0.152	2.5E-3	1.68
Average systematic for cuts		2.6E-3	1.76
	dN/dy	Difference	Difference (%)
dN/dy with default parameters	0.150	N/A	N/A
PID No PID	0.145	5.3E-3	3.55
PID n_σ = 1	0.176	2.6E-2	17.5
Average systematic for PID		1.0E-2	6.95
Template constraints	0.125	2.5E-2	16.5
MC choice	0.156	5.9E-3	3.97
Efficiency correction method	0.152	1.82E-3	1.22
Phase Space correction	0.150	7.9E-5	5.3E-2
Average systematic for peak shape		2.1E-2	13.7
Total syst		3.5E-2	23.1

Table A.13: Systematic error estimation for the $\langle p_t \rangle$ result of the f_2 (1270) spectrum.

	$\langle p_t \rangle$	Difference	Difference (%)
$\langle p_t \rangle$ with default parameters	1.30	N/A	N/A
Fitting range 0.28 - 1.9 GeV/c	1.29	1.9E-2	1.42
Fitting range 0.28 - 2.0 GeV/c	1.45	0.146	11.2
Fitting range 0.40 - 1.8 GeV/c	1.31	5.4E-3	0.415
Fitting range 0.50 - 1.8 GeV/c	1.30	9.0E-5	6.9E-3
Average systematic for fitting range		3.3E-2	2.5
	$\langle p_t \rangle$	Difference	Difference (%)
$\langle p_t \rangle$ with default parameters	1.30	N/A	N/A
DCA$_z$ = 0.3 cm	1.28	2.8E-2	2.17
DCA$_z$ = 0.1 cm	1.29	1.0E-2	0.775
DCA$_r$ = 6 σ	1.28	2.5E-2	1.88
DCA$_r$ = 8 σ	1.27	3.2E-2	2.43
Minimum track p_t = 0.2 GeV/c	1.25	5.7E-2	4.34
TPC minimum number of clusters = 50	1.23	7.2E-2	5.52
TPC max χ^2 = 6	1.20	9.9E-2	7.62
Average systematic for cuts		4.6E-2	3.53
	$\langle p_t \rangle$	Difference	Difference (%)
$\langle p_t \rangle$ with default parameters	1.30	N/A	N/A
PID No PID	1.25	5.5E-2	4.23
PID n_σ = 1	1.23	7.7E-2	5.90
Average systematic for PID		6.6E-2	5.07
Template constraints	1.24	6.2E-2	4.75
MC choice	1.19	0.111	8.52
Efficiency correction method	1.30	8.5E-4	6.5E-2
Phase Space correction	1.37	7.0E-2	5.41
Average systematic for peak shape		3.0E-2	2.30
Total syst		0.157	12.0

Table A.14: Systematic error estimation for the T parameter in the f_2 (1270) spectrum Tsallis function (equation 4.4) fitting.

	T	Difference	Difference (%)
T value with default parameters	0.490	N/A	N/A
Fitting range 0.28 - 1.9 GeV/c	0.480	9.9E-3	2.01
Fitting range 0.28 - 2.0 GeV/c	0.427	6.4E-2	13.0
Fitting range 0.40 - 1.8 GeV/c	0.441	4.9E-2	10.0
Fitting range 0.50 - 1.8 GeV/c	0.456	3.4E-2	7.01
Average systematic for fitting range		3.9E-2	8.00
	T	Difference	Difference (%)
T value with default parameters	0.490	N/A	N/A
DCA$_z$ = 0.3 cm	0.365	0.125	25.6
DCA$_z$ = 0.1 cm	0.374	0.116	23.7
DCA$_r$ = 6 σ	0.356	0.134	27.4
DCA$_r$ = 8 σ	0.351	0.139	28.4
Minimum track p_t = 0.2 GeV/c	0.343	0.147	30.0
TPC minimum number of clusters = 50	0.317	0.173	35.2
TPC max χ^2 = 6	0.288	0.2022	41.3
Average systematic for cuts		0.148	30.22
	T	Difference	Difference (%)
T value with default parameters	0.490	N/A	N/A
PID No PID	0.404	8.6E-2	17.6
PID n_σ = 1	0.322	0.167	34.1
Average systematic for PID		0.127	25.9
Template constraints	0.461	2.98E-2	5.84
MC choice	0.402	8.9E-2	18.1
Efficiency correction method	0.371	0.119	24.4
Phase Space correction	0.326	0.164	33.5
Average systematic for peak shape		9.8E-2	20.1
Total syst		0.241	49.1

Table A.15: Systematic error estimation for the n parameter in the f_2 (1270) spectrum Tsallis function (equation 4.4) fitting.

	n	Difference	Difference (%)
n value with default parameters	13.0	N/A	N/A
Fitting range 0.28 - 1.9 GeV/c	13.4	0.414	3.19
Fitting range 0.28 - 2.0 GeV/c	21.9	8.89	68.5
Fitting range 0.40 - 1.8 GeV/c	19.8	6.77	52.2
Fitting range 0.50 - 1.8 GeV/c	22.8	9.87	76.1
Average systematic for fitting range		6.49	50.0
	n	Difference	Difference (%)
n value with default parameters	13.0	N/A	N/A
DCA$_z$ = 0.3 cm	15.3	2.35	18.1
DCA$_z$ = 0.1 cm	15.6	2.59	20.0
DCA$_r$ = 6 σ	13.0	1.2E-2	9.4E-2
DCA$_r$ = 8 σ	12.6	0.343	2.64
Minimum track p_t = 0.2 GeV/c	6.46	6.52	50.2
TPC minimum number of clusters = 50	10.1	2.88	22.2
TPC max χ^2 = 6	8.16	4.82	37.1
Average systematic for cuts		1.38	10.6
	n	Difference	Difference (%)
n value with default parameters	13.0	N/A	N/A
PID No PID	16.9	3.97	30.6
PID n_σ = 1	11.1	1.84	14.1
Average systematic for PID		1.07	8.22
Template constraints	10.6	2.41	18.5
MC choice	13.5	0.504	3.88
Efficiency correction method	12.9	8.8E-2	0.679
Phase Space correction	12.1	0.865	6.66
Average systematic for peak shape		6.8E-2	0.524
Total syst		7.15	55.1

Table A.16: Systematic error estimation for the mass measurement for the f_2 (1270) peak fitting in the p_t integrated π^+ π^- spectrum.

	Mass	Difference	Difference (%)
Mass value with default parameters	1.26	N/A	N/A
Fitting range 0.28 - 1.9 GeV/c	1.26	1.43E-3	0.11
Fitting range 0.28 - 2.0 GeV/c	1.26	1.5E-3	0.12
Fitting range 0.40 - 1.8 GeV/c	1.25	8.8E-3	0.70
Fitting range 0.50 - 1.8 GeV/c	1.25	9.2E-3	0.73
Average systematic for fitting range		5.2E-3	0.41
	Mass	Difference	Difference (%)
Mass value with default parameters	1.26	N/A	N/A
DCA$_z$ = 0.3 cm	1.27	6.3E-3	0.50
DCA$_z$ = 0.1 cm	1.26	2.0E-3	0.16
DCA$_r$ = 6 σ	1.26	4.0E-5	3.2E-3
DCA$_r$ = 8 σ	1.26	4.7E-4	3.7E-2
Minimum track p_t = 0.2 GeV/c	1.26	1.9E-3	0.15
TPC minimum number of clusters = 50	1.27	4.9E-3	0.39
TPC max χ^2 = 6	1.26	5.7E-4	4.5E-2
Average systematic for cuts		1.6E-3	0.13
	Mass	Difference	Difference (%)
Mass value with default parameters	1.26	N/A	N/A
PID No PID	1.24	2.3E-2	1.82
PID n_σ = 1	1.24	2.7E-2	2.10
Average systematic for PID		2.5E-2	1.96
Template constraints	1.27	5.8E-3	0.46
MC choice	1.26	1.2E-4	9.5E-3
Efficiency correction method	1.26	0	0
Phase Space correction	1.26	2.2E-3	0.17
Average systematic for peak shape		1.1E-3	8.5E-2
Total syst		2.6E-2	2.06